On the Mach number Effects on Droplet Breakup in Laminar Flow

Irfan Miladi Syahdan

A thesis submitted in partial fulfillment of the

requirements for the degree of

Master of Science in Aeronautics and Astronautics

University of Washington

2015

Reading Committee:

James C. Hermanson

Antonino Ferrante

Program Authorized to Offer Degree:

Department of Aeronautics and Astronautics

University of Washington

Abstract

On the Mach number Effects on Droplet Breakup in Laminar Flow

Irfan Miladi Syahdan

Chair of the Supervisory Committee:

Professor James C. Hermanson

Co-Chair Professor Antonino Ferrante

Department of Aeronautics and Astronautics

A Volume of Fluid (VOF) multiphase numerical study was conducted using the commercial simulation software ANSYS Fluent to understand the effects of compressibility on droplet breakup in the laminar flow regime. A 2D axisymmetric domain which consists of four subdomains was used for the simulations. Validation of the setup and mesh was conducted by comparing to analytical shock tube equation, Engel's, and Boger *et al.'s* work. Two regimes of flows, subsonic and supersonic, were used and were obtained by selection of the operating pressure, velocity, density, dynamic viscosity, and temperature to keep the Reynolds, Weber, and Mach numbers at fixed values between cases. The Reynolds number was held constant at 100. Significant differences within the stripping breakup mode between the supersonic and subsonic cases for similar values of the Weber and Reynolds numbers were observed. The difference was observed in terms of droplet deformation, droplet deformed shape, and droplet lifetime. A Weber number effect is also observed to influence the droplet lifetime. Differences in the pressure distribution were found to drive the different degrees of vertical elongation while the viscous stress mainly acts to bend the droplet downstream. The pressure was found to be the major factor while viscous stress acts as the smaller factor in the physics during most of the deformation process, but viscous stress shows to be the major role at the

beginning of the process. Comparison to the solid sphere case provided confirmation of the pressure distribution difference observed between supersonic and subsonic case was expected. Comparison to solid sphere also shows how droplet deformation itself plays a role in effecting the flow field.

Table of Contents

List of Figures

List of Tables

Acknowledgement

During the process of this thesis, much help and support was given to me and I would like to express my gratitude. First and foremost, I would like express my gratitude to my parents who have always been there for moral support. I thank my advising committee, Professor James C. Hermanson and Professor Antonino Ferrante, whose advice has helped me to write this thesis. I am also grateful for the friendship and the family warmth far from home provided by The Indonesian Kelurahan community at Blakey Seattle. I would like to say thank you to the staff of the William E. Boeing Department of Aeronautics & Astronautics, which has provided a lot of administrative help, especially Mr. Ed Connery. The discussion with friends at the department RA room also is greatly appreciated. Last but not least, I would like to say thank the Fulbright Scholarship program that has funded my studies at the University of Washington.

Chapter 1 Introduction

Droplet disruption, breakup, and vaporization have been active areas of research for several decades.The problem is sparked by the ubiquitous use of liquid droplets in engineering technology, with important applications for combustion, propulsion, materials processing, and others. The details of the droplet disruption process can also have a direct effect on liquid dispersion in many systems. In propulsion, one of the important effects is how liquid fuel dispersion affects the efficiency of the combustion, which is linked to the droplet breakup [1]. In high-speed aerospace applications, droplet disruption and fuel dispersion may be important in the case of liquid-fueled scramjets. The potential operating cost reduction by using liquid fuel instead of cryogenic fuel also motivates research in droplet breakup under supersonic conditions [1]. The understanding of droplet breakup in compressible flows, especially supersonic flow, will be important to better understand the combustion in scramjet. This can lead to a better design and paving a path for economical hypersonic flight.

The studies of droplet breakup have historically involved mostly experiments using shock tubes [2], [3], [4], and/or wind tunnels as the flow generators [5]. In various studies the flow velocity has ranged from subsonic (incompressible) to high supersonic (compressible). Most shock tube experiments used the Mach number of the moving shock wave as the flow parameter, not the Mach number of the flow behind the shock wave, which is the actual flow over the droplet as it undergoes disruption. This often implies that the flow encountering the droplet is high subsonic rather than supersonic. The incoming flow velocity variation in each experimental study tends to be limited due to the high cost of changing the experiment setup, such as changing the shock tube or wind tunnel geometry. Most experiments use either high subsonic or high supersonic freestream flow with only a few experiments having both low subsonic (incompressible) and high supersonic (compressible) flows [5], [6]. The preferred method of changing the droplet disruption parameters is typically to vary the droplet parameters, such as the droplet size or droplet material, rather than changing flow conditions.

This is a numerical study that follows on the experimental studies of Jun & Hermanson [1] and Lin & Hermanson [7] on droplet breakup in accelerating supersonic flows. In those cases the Weber numbers and Mach numbers changed constantly and produced some differences in breakup modes compared to that for the more commonly studied case of constant Weber and Mach numbers [1]. Because the flow was accelerated and the droplet is moving, the relative velocity between flow and droplet continuously changes, which in turn resulted in a change in the non-dimensional parameters that characterize droplet disruption. Different breakup modes compared to the more commonly studied constant-flow case were clearly seen.

A fundamental question is how compressibility plays a role in the deformation and breakup modes of droplets in high-speed flows. This study aims at observing the compressibility impact on droplet breakup by using numerical modelling. The numerical model uses three key parameters which are Mach number (low subsonic and supersonic), Weber number, and Reynolds number. These parameters represent respectively the effects of compressibility, surface tension, and viscosity. Due to the expensive computing resource needed for simulating accelerating flows, this study investigated compressibility effects through the action of constant freestream flows.

1.1 Characteristics Parameters in Droplet Disruption

1.1.1 Weber number

Droplet break up modes are commonly described using the dimensionless parameter of the Weber (We) number:

$$We = \frac{\rho_g {U_\infty}^2 d_o}{\sigma} \quad , \tag{1}$$

where ρ_g is the gas density (for a gas-liquid system), d_o is initial droplet diameter, U_∞ is the freestream velocity of the incoming gas, and σ is the droplet surface tension.

As can be seen by the Eq. (1), We describes the competing effects of the aerodynamic force that drives droplet deformation & disruption and the surface tension that is trying to hold the droplet intact. In

calculating the Weber number, the density and velocity are traditionally taken to be the freestream values of the flow. The Weber number suggests that if the droplet properties are kept constant, then flow properties such as gas density and velocity will essentially determine the breakup modes. But it also means that if something changes these two variables on the droplet mode, such as a bow shock in front of the droplet, the Weber number, and hence the droplet breakup mode, will also change accordingly. How this sudden change in flow properties affects breakup has not been explained properly in the literature to date.

1.1.2 Reynolds number (*Re*)

The Reynolds number is an indication of flow inertia compared to its viscosity, and has important implications for the viscous stresses in the flow, the transition to turbulence, and the wake region downstream of a bluff body. For low *Re*, viscosity is more prominent compared to the momentum in the flow and tends to keep the flow laminar. Experimental results for low Reynolds numbers over a solid sphere are well-known, and for a value of Reynolds number of *Re* = 100 there will be laminar recirculation region behind a smooth, solid sphere. The Reynolds number is defined as

$$Re = \frac{\rho_g U_\infty d_0}{\mu} \quad , \tag{2}$$

where ρ_g is the gas density (for a gas-liquid system), d_o is initial droplet diameter (characteristic length), U_∞ is the freestream velocity of the incoming gas, and μ is the dynamic viscosity of the gas.

1.1.3 Mach number

The Mach number is the main indicator of the degree of compressibility in a flow. The Mach number is a non-dimensional variable that relates an object's velocity to the sound speed of the fluid in which it travels. The Mach number is also an indicator of when a shockwave can be expected to occur, which is important for the overall flow due to the "jumps" of flow properties across a shock wave.

The definition of Mach number is

$$M = \frac{v}{a} = \frac{v}{\sqrt{\Upsilon RT}}, \tag{3}$$

where v is the flow velocity, a is the sound speed, Υ is the specific heat ratio, R is gas constant, and T is the absolute temperature.

1.2 Reynolds numbers in previous studies of droplet disruption

The Reynolds number is often used as an indicator of whether a flow region can be expected to be laminar or turbulent. Over a sphere, $0 < Re < 150$ suggests that the flow is laminar. Below $Re = 100$, the flow will normally follow the curvature of the sphere. A laminar flow can have a standing recirculation region behind the sphere for $100 < Re < 150$. This recirculation region remains in a constant position relative to the droplet and is essentially symmetric about the droplet center line. The recirculation region normally transitions to a shedding vortex for $Re > 150$. In addition, above this Re value, the boundary layer can already be transitioning from laminar to turbulent, depending on the flow conditions and other factors, such as surface roughness.

In terms of Reynolds number, most previous experiments were in the turbulent region due fact that the droplet sizes were in millimeter ranges and the droplets were accompanied by comparatively high freestream flow velocities. In studies of droplet in supersonic flows, a turbulent wake is expected from the high-velocity freestream flow, typically commensurate with Reynolds numbers ranging from thousands to hundreds of thousands. The closest Reynolds number flows to laminar were seen in the study of Theofanous *et al.* [8], [6] and Boiko & Poplavski [9], including one case in Theofanous *et al.* with a Reynolds number of approximately $Re = 210$, while Boiko & Poplavski report $Re > 1000$ for their cases. Boiko & Poplavski [9] presented a discussion about the recirculation on a model droplet while Theofanous *et al.* did not present any further description of that case other than pressure region inside the droplet. To the best of the knowledge of this author there is no previous study that used a constant, laminar Reynolds number especially when studying droplet in both supersonic and subsonic flows.

1. 3 Constant Freestream Velocity Droplet Breakup Modes

The classical reference of Pilch & Erdman [5] categorizes the break up into vibrational, bag, bag & stamen, sheet stripping, wave crest stripping, and catastrophic break up. Over the years, multiple experiments have refined these categories, especially concerning the break up between bag and sheet stripping modes. These different breakup modes will be summarized below.

1.3.1. Deforming Region

The deforming region is where the droplet starts to deform, which can easily be recognized from the changing of shape from spherical to ellipsoidal. The process is called droplet flattening. Hsiang & Faeth [10] also add sub-categories, non-oscillatory and oscillatory, dividing the region to whether surface tension is capable to damp the force imparted by the flow or not.

The deforming droplet disruption region is a precursor to other breakup modes if the Weber number is sufficiently high for breakup or as a mode to itself if breakup does not occur. $We < 12$ describes this deforming area by Pilch & Erdman [11] and Joseph *et al*. [11]. An additional feature of fluid collecting at the droplet edges was captured by Theofanous *et al.* [6] and by Joseph *et al*. [4] which was not observed by the previous experiment of Engel [2]. Figure 1 displays this fluid accumulation phenomenon.

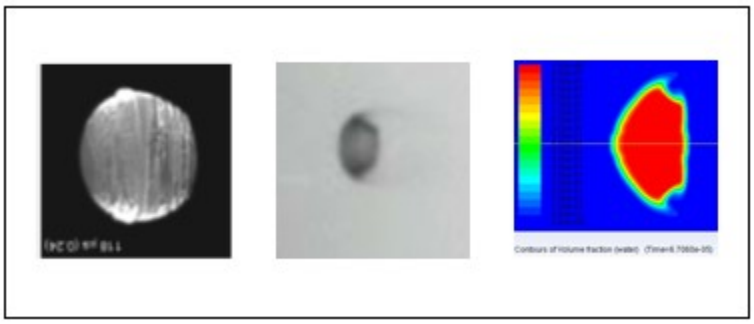

Figure 1. Accumulation of fluids at the droplet edge: Left, Theophanous *et al*. [6]; center Joseph *et al*. [4], and validated by the current simulation [12]. All images have been rotated, so that the flow is moving from left to right.

1.3.2. Vibrational Distortion

Vibrational distortion of the droplet occurs for $We < 12$ if the oscillating disturbance is not dampened. Due to this oscillation and its slow breakup time, droplet breakup is rarely seen even for $We < 12$. As it does not normally lead to droplet breakup the vibrational mode is often neglected by researchers, only considered by Gelfand [13] and Pilch & Erdman [11].

1.3.3. Bag Breakup

In the bag breakup mode a small portion of the droplet center mass forms a thin "bag" structure attached to a toroidal "ring" which contains the bulk of the droplet mass [11]. This process starts with the droplet being flattened and forming a liquid disk [14], similar to that at the end of the vibrational/oscillatory deforming process described above. The bag portion then forms due to flow that goes through the droplet center and blows the droplet center downstream. This process continues until the bag bursts after as the oncoming flow overcomes surface tension, in a process called piercing. The burst bag forms very fine droplet/mist, much smaller than the initial droplet. The toroidal ring which contains most of the droplet mass continues to break apart in a mode that is similar to catastrophic break up and has relation to the Rayleigh-Taylor instability that appears there, as seen in Theofanous *et al.'s* work [8].

The viscosity of the droplet compared to the surface tension is reflected in the Ohnesorge number

$$Oh = \frac{\mu_d}{\sqrt{\rho_d \sigma d}} \quad , \tag{4}$$

where μ_d is the droplet dynamic viscosity, ρ_d is droplet density, and σ is the surface tension

It should be noted that increasing the Ohnesorge number, i.e. with TBP, increases the chance of observing bag breakup. Some experiments that use water, a relatively low *Oh* droplet material, do not show bag breakup. Experiments using droplet with higher *Oh* almost always shows bag breakup. Gelfand in his work also states that bag breakup is seen on droplet with "enhanced viscosity". It is unclear form the literature precisely which values of Weber number characterize the bag-breakup mode with different values of *Oh*. All bag breakup modes mentioned here have $Oh < 0.1$ (non visco-elastic).

1.3.4. Bag stamen/Multimode Breakup

Many classical papers identify bag-stamen as the breakup mode with a higher Weber number than for the case of pure bag breakup. Between the bag and sheet-stripping modes, typically $50 < We < 90$, there are a few modes that resemble bag breakup with additional physical features, such as a long strand of liquid tail in the center of the bag, a short coherent center structure inside the bag structure, and a multiple bag-like structure. This has also been recognized as the transition region and as a multibag/multimode breakup in some studies [6], [13], [15]. This mode normally appears for Weber numbers higher than those seen for bag breakup**.** Factors that contribute to additional bag appearance are number of interfacial waves at the windward surface of the droplet and drag on the droplet as it changes shape. Joseph *et al.* suggest a rule of thumb was stated that every 2 increments in wave number resulted in 1 additional bag [4].

1.2.5. Sheet Stripping Break Up/ Shear Induced Breakup

For higher velocities and still higher values of the Weber number, a stripping-type of behavior occurs. The **s**tripping breakup does not form the bag seen in bag and multimode breakup, although the breakup does start with the flattening of the droplet. After the flattening process, fluid accumulates at the

equator of the droplet, as seen in Fig.1. It should also be noted that the flattening process normally results in the formation of a lenticular shape (hemispherical in the windward interface but comparatively straight at the leeward interface [4]). These flattening shapes were seen in the works of Engels [13], Joseph *et al.* [2], Dai & Faeth [15], and also in author's simulation [12].

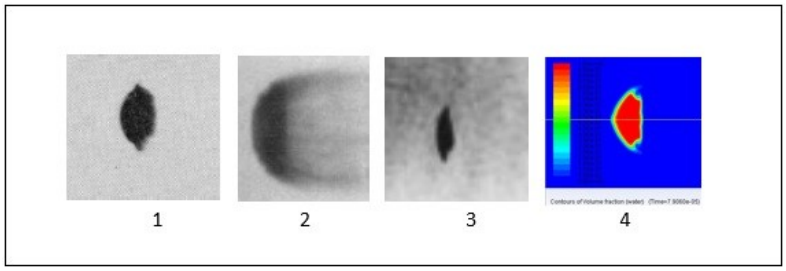

Figure 2. Flattened droplet undergoing sheet-stripping breakup 1. [4] 2. [4] 3. [15] 4. Past test case of this research [12], in the Annual Poster Event of William E. Boeing Department of Aeronautics and Astronautics, Dec 2014. All images have been rotated such as the flow is moving from left to right.

For higher values of Weber number still, the mechanism on how the droplet loses fluids depends on which subcategory of stripping breakup that occurs. Previous experiments show that for stripping breakup the Weber number can have a broad range of values from $We = 10^2 – 10^6$. Thus, stripping breakup can be considered the final mode of droplet breakup short of the total, catastrophic breakup discussed below. Joseph *et al.* also state this in their experiment [4], as their results show sheet stripping still occurring for $We > 45000$. The results which show that $We < 350$ results in sheet stripping is for low *Oh* number ($Oh < 0.1$).

Stripping breakup is evidently divided into two regimes, namely, sheet stripping and wave crest stripping. Engels [2], Joseph *et al.* [4], and Dai & Faeth [15] did not observe this wave cress stripping mode. It appears that wave cress stripping breakup is similar to sheet stripping breakup but with numerous smaller interfacial waves. Both the droplet fluid and the interfacial waves are transported to the edge/equator by shear, and thus accumulate there [4]. The peripheral fluid accumulation occurs at the location where the fluids are being stripped into thick mist. However, Engels noted that mist also emanates from the windward surface [2]. This obscures the true shape of the droplet core where it is mostly still liquid.

1.3.6. Catastrophic Breakup

Catastrophic breakup occurs when the unstable waves grows faster than the stripping process that can remove material from the droplet then causes the droplet to fragment [11]. The experiments that support this breakup mechanism relate it to the interfacial waves and Rayleigh-Taylor (R-T) instabilities. A recent experimental work conducted by Theofanous *et al.* [6], report that they did not observe any such waves using a new imaging technique and the waves seen in previous experiments were caused by the limited capability of shadowgraph at the time, where the image can be obscured by the generated droplet mist. However, their experiment did show fragmentation of the liquid ring after bag bursts in the bag breakup mechanism. This fragmentation is most likely due to the same R-T instability growth that caused catastrophic breakup. The existence of catastrophic breakup was acknowledged by a few studies but the precise values of Weber number that characterize this breakup mode remain inconclusive as this mode is frequently associated with stripping breakup.

1.3.7 Recirculation Region behind Deformed Droplet in Stripping Breakup

There are only a few studies that elaborate the recirculation region on the droplet leeward side and its effect on droplet breakup [9], [16]. Pressure and drag are often the variables reported to be connected to the droplet deformation. Consideration of the recirculation region might bring additional insight into the deformation process because the tendency of the recirculation region to result in a low pressure region that may further impact the droplet deformation and disruption.

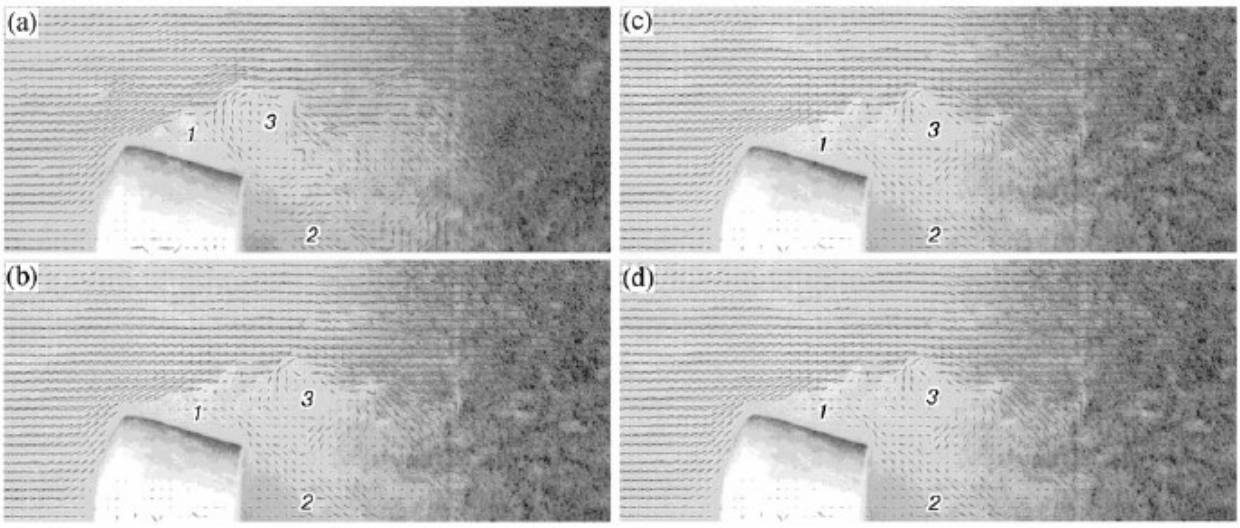

Figure 3. Boiko & Poplavski's recirculation region on a droplet model using a solid deformed object: 1) Flow separation region; 2) Reverse base flow; 3) Isolated toroidal vortex. $1.1<Ms<1.4$, We = 400-2100, d = 2.2 mm, $Re>$ 1000 [9].

Boiko & Poplavski's study [9] used a solid model that simulates a deformed droplet to observe how flow behaves in the leeward region of the droplet. The droplet model shape was developed after observing droplet shapes after being deformed in a process similar to stripping breakup. The model shows there is a recirculation region near top edge of the droplet and an isolated toroidal vortex near center of the droplet. Boiko & Poplavski stated that the top recirculation region interacts with the top surface and has influence in the growing section of fluid at the mid sector, most likely related to the fluid accumulation at the equator seen in other studies. They also stated that this separate toroidal vortex has effect on to the droplet flattening due to their position. Their model is shown in Fig. 3.

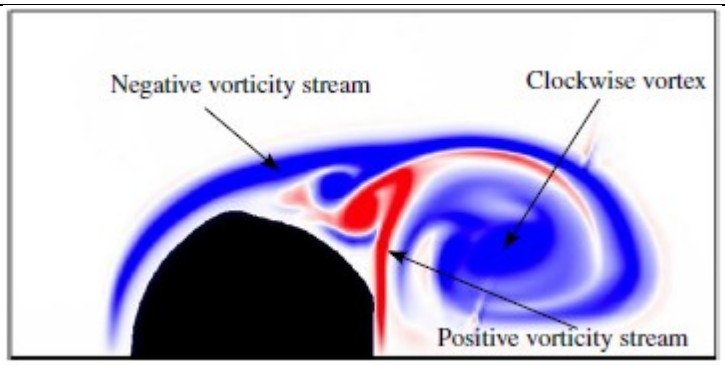

Figure 4. Meng & Colonius vorticity field at early breakup stage. The positive (red) and negative (blue) vorticity streams interact to form the recirculation region. M_s = 1.4, Re = 237.000 [16].

A numerical study by Meng & Colonius considered the recirculation region. Although their flow conditions were different from those of Boiko & Poplavski, they report a similar recirculation region near the top of the droplet. This recirculation region is stated to be a result of two different values of vorticity interacting in the early stages of the breakup [16]. However, the isolated toroidal vortex was not mentioned.

1. 4. Accelerating Freestream Velocity Breakup Modes

Unlike droplet breakup in using a constant freestream velocity (U_∞), which was the case for most of the studies cited above, droplet breakup with a constantly changing U_∞ has not been studied extensively, especially in the high velocity (highly compressible flow) range. In real life scramjets, the flow will be most likely an accelerating flow, hence studies in this type flow will bring additional information on droplet breakup in a scramjet [1].

The method to achieve this acceleration is to drop liquid into a nozzle, allowing the droplet to accelerate with the accelerating flow. A concern that the droplet will breakup completely before reaching high velocity was overcome by Kim & Hermanson using a wind tunnel nozzle with a smooth acceleration/loading profile [1]. Their experiment is among a few that studied droplet disruption in the presence of an accelerating, supersonic flow.

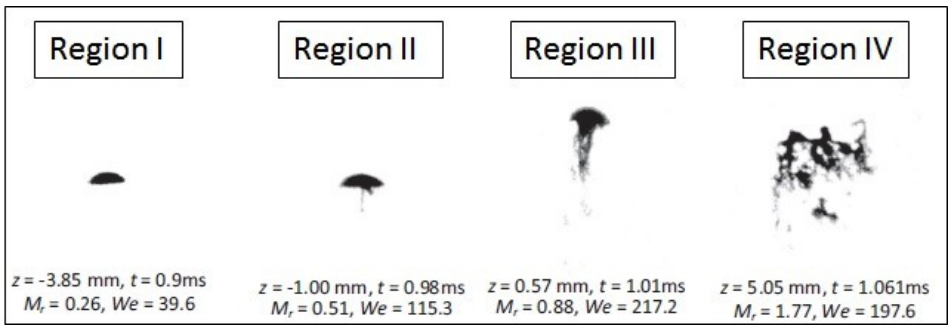

Figure 5. Droplet breakup stages for the case of an accelerating freestream [1]

The breakup process in this case was reported to have four main regions [1], as seen in Figure 3. The first region is the deformation region which is similar to the deforming region previously mentioned. The droplet undergoes the flattening process to an ellipsoidal shape, at We = 10.5 & M_r = 0.12 (region I). As the Weber number increases to 39.6 the droplet assumes a lenticular shape. Further downstream (region II), as We = 115.3 a thin tail is formed in the leeward side. *Re*gion III is where the primary break up occurs [1], at the We = 217.2 and M_r = 0.88. At this stage, leeward interface experiences chaotic breakup and windward interface keeps to deform. This region continues even as We = 278 and M_r = 1.45. To be noted that the droplet core is still present at this region. This region, in a few cases, has some similarities with Theofanous *et al.'s* experiment with We = 150, configuration C-D3.B, a Mach 3 case. The last region, region IV, droplet fragments into much smaller pieces or into mist. The mode is similar to catastrophic breakup and/or the droplet state of ring fragmentation in multimode breakup [6].

The breakup modes seen under accelerating-flow conditions are a mix of various breakup modes seen on constant freestream studies, with additional modes such as trailing tail on lenticular shape seen on region II. The continuous and substantial changes in flow condition change the Weber number which may explain the changing modes, as well as their occurrence for different values of Weber number than reported in the classical literature. As is known well for constant-freestream-velocity cases, large differences in Weber number will lead to different breakup modes. But the fact that there are some differences in breakup modes from the equivalent Weber number in the constant-freestream cases suggest that there might be some

important compressibility effects. Establishing these effects of compressibility on droplet deformation and disruption was the principal focus of the current study.

1. 5. Research Objectives

The research aims at studying the impact of compressibility on droplet breakup modes in low subsonic ($M = 0.2$) and moderate supersonic flows ($M = 1.5$ - 2). Previous research has considered droplet breakup at various Weber numbers and droplet viscosities. Previous works tended to focus in incompressible and high subsonic flows with only a few that are true supersonic, even only few newer ones are truly supersonic. Older studies tend to use incompressible low subsonic flows and then high subsonic flows, while true supersonic flows are mostly done in a few newer studies. But these works do not mention clearly the effect of different Mach numbers for a similar Weber number, implying that droplet breakup will be the same if the Weber number is the same. Previous studies also rarely employed a constant Reynolds number when varying Mach number which is practically difficult to achieve in an experiment. The effect of Mach number has also not been clearly separated from the effect of Reynold number. This causes some uncertainties whether the differences in droplet disruption observed, if any, are caused by the variation in Mach number, Reynolds number, or a combination of both.

The main goal of this study was to observe whether there is any difference in droplet breakup between incompressible (low subsonic) freestream and compressible (supersonic) freestream for the case of fixed Weber and Reynolds numbers. By having a few fixed values of Weber numbers, the effects from Weber number variation for the same Mach and Reynolds number can also be observed. The focus is on the general trends, using the differences in breakup observed to develop an understanding on the underlying flow physics. This work does not address the finer details of daughter droplet size, evaporation, or fragmentation. A better understanding of the impact of compressibility on droplet disruption can ultimately lead to better high speed aerospace propulsion design.

This research attempts to answer the following specific questions:

1. What is the impact of compressibility on droplet breakup?

2. Is there a difference in breakup mode for a constant upstream Weber and Reynolds number with low subsonic and supersonic Mach numbers?

3. What are the underlying physic causes for the resulting differences in droplet deformation?

Chapter 2 Numerical Study Method and Setup

2. 1 Numerical Software Package and General Steps

This numerical study has been conducted using ANSYS Fluent CFD software along with ANSYS Design Modeler and ANSYS Meshing for geometry and mesh generators.

Every numerical modeling starts with determining which physical phenomena that are important to the study. In this study, the important phenomena are droplet breakup modes, deformation, and the flow field around it. These require a sufficient number of mesh elements across the droplet diameter to resolve the curvature. Consideration has to be made of whether the physical phenomena can be represented using planar, axisymmetric or 3D case. The latter is the most accurate and ideal for almost all types of physics but it is the most computationally expensive. Another main consideration is the computational resources available. These considerations are translated into the decision of size and division of the domain. Along with geometry generation, this step is conducted in ANSYS Design Modeler. The domain is then transferred to ANSYS Meshing for mesh generation. Each division of the domain will have a certain determined mesh element size and has a mapped surface control. This control produces a well-structured grid because the domain essentially does not have any curves. The Inter-mesh division is connected with interfaces performed internally to Fluent.

2.2 Volume of Fluid (VOF)

A distinct interface between the phases is a main attribute of a volume-of-fluid (VOF) method, as this method is categorized as a front capturing method [17]. VOF was first developed to solve free boundary problems [18]. This method uses a stationary computational domain where interactions and the physics of phases occur within the domain boundaries. The opposite method is a moving mesh which follows the physical phenomenon around, i.e., follows the droplet. In VOF, the presence of a distinct phase is calculated in the cell and is indicated by the volume fraction, C. C has a value between 0 and 1, and when an

intermediate value occurs in a computational cell then the interface between the phases is present in that cell. Locating the interface inside a cell and its normal direction is done with the mixed Young-centered method [19].

2.2.1 VOF Implementation in FLUENT and Governing Equations of VOF

The implementation of VOF in Fluent is described in a summary from Fluent Theory Guide [20], in its chapter on VOF. Volume Of fluid (VOF) is implemented in Fluent by calculating the volume fraction of phases inside a cell. The percentage of each phase volume fraction in a cell will determine how the other flow variables are represented, either as described as one shared values between the phases in the mixture level or represent the values of each one phase. This practice is aligned with other VOF studies. There will be three possible phase volume fraction types in a cell, where Fluent uses α_q to denote the volume fraction values. These possibilities are illustrated below [20]

- The phase is non-existent in the cell, $\alpha_q = 0$
- The phase is fully occupying the cell, $\alpha_q = 1$
- The phase shares the cell with other phases, and an interface among them is present in the cell, $0 < \alpha_q < 1$.

In non-evaporation case, where the evaporation module in Fluent is not turn on, ideally the phase considered are only liquid and gas. There will be no physical diffusion between the two phases, however numerical diffusion might still occurs. This depends on the volume fraction treatment used on in the simulation. Treatment that inhibits diffusion commonly needs lower stable time step value compared to the ones that allows numerical diffusion.

Tracking the interface between phases is an important part of VOF. Fluent does this by calculating continuity equation of each phase, the number of continuity equations are determined by the values of α_q

in a cell. Equation (5), taken from Fluent Theory guide, represents a continuity equation for a single phase (q)

$$\frac{\partial}{\partial t}\left(\alpha_q \rho_q\right) + \nabla.\left(\alpha_q \rho_q \bar{v}_q\right) = 0 \quad (5)$$

Where α_q is the volume fraction percentage, ρ_q is density of phase q. The r.h.s. of Eq. (5) is zero because this study focuses on non-evaporating droplets. Equation (5) is integrated in time using an implicit time discretization scheme.

2.3 ANSYS Fluent Setup

This study is a multiphase transient simulation on an axisymmetric mesh using the VOF module in ANSYS Fluent. The current version of Fluent allows only for pressure-based solver when solving a multiphase flow. Traditionally, density-based is the solver type of choice for high Mach number flows, but the evolution of Fluent over the years has made the density based and pressure based solver to have little difference, if any, in terms of general accuracy and stability.

The primary phase material used modified air, which has all the properties of air except a modified dynamic viscosity to allow for independent control of the Reynolds number. Through the power law, a base dynamic viscosity reference value is set to obtain the desired viscosity at the chosen temperature. This artificial air is set to the ideal gas law for compressible cases and incompressible ideal gas for incompressible cases. The secondary phase material, typically set for the droplet liquid, is isopropanol (2-propanol) which value is inputted by a .scm file. Isopropanol was chosen for its lower vapor pressure to avoid consideration of evaporation, and for comparison with experiment [7]. The isopropanol surface tension value of 0.0213 N/m^3, obtained from ref [1], is then inputted using the "phase interaction" option under "surface tension" tab. The "patch" function inserts the isopropanol value to the calculation domain. This function introduces user's input variables to a specified region in the domain. In this case, the variable is volume fraction of isopropanol. The droplet is patched near the "axis" boundary condition of the

axisymmetric line which is the center line. This create a half-circle containing isopropanol values. The mesh is shown in Figure 6.

A "velocity-inlet" boundary condition is selected for the inlet boundary condition. This boundary condition allows the user to specify the velocity magnitude and temperature of the inlet flow. The Mach number of the inlet flow, also the freestream value, can be easily predicted using these two input variables. The capability to specify the air velocity helps in controlling the Reynolds and Weber numbers. The density and pressure of the inlet flow were then determined by Fluent using the ideal gas law and the specified operating pressure. For the outlet, a "pressure outlet" boundary condition is used with default setting where it is set to have the same pressure as the operating pressure by specifying the "gauge pressure" as zero.

The upper most boundary condition uses a "symmetric" boundary condition that prevents the shock wave from reflecting back inside the domain. All boundary condition located at the centerline axisymmetric line use the "axis" boundary condition. To connect each sub domain, their boundary condition use the "interface" boundary with names specified at geometry generation.

The main factor to ensure numerical stability is to have the flow only to pass a small number of mesh elements in one time step. A "rule of thumb" for a stable time step is shown in equation (6)

$$dt = \frac{dx}{v}, \tag{6}$$

Where *dt* is the time step, *dx* is the smallest mesh element length, and *v* is the flow velocity passing the smallest mesh element.

This principle of setting an appropriate the time step value is always a good practice when the boundary or deformable fluid-fluid interface does not move in time. But this study patches the volume fraction value of the droplet and its interface will move/deform as flow passes over the droplet. Small deformation of the interface does not affect the stability to noticeable level, only causing the residual to decrease more slowly. But a breaking/stripping interface will cause appreciable instabilities in the

calculation especially at the time of initial liquid breaking/stripping, which requires adjustment of the time step value. Using a "body force weighted" pressure discretization relieves this instability and enable time step to be around the value calculated with Eq. (6). Another major factor that contributes to stabilities is using the implicit scheme rather than the explicit scheme.

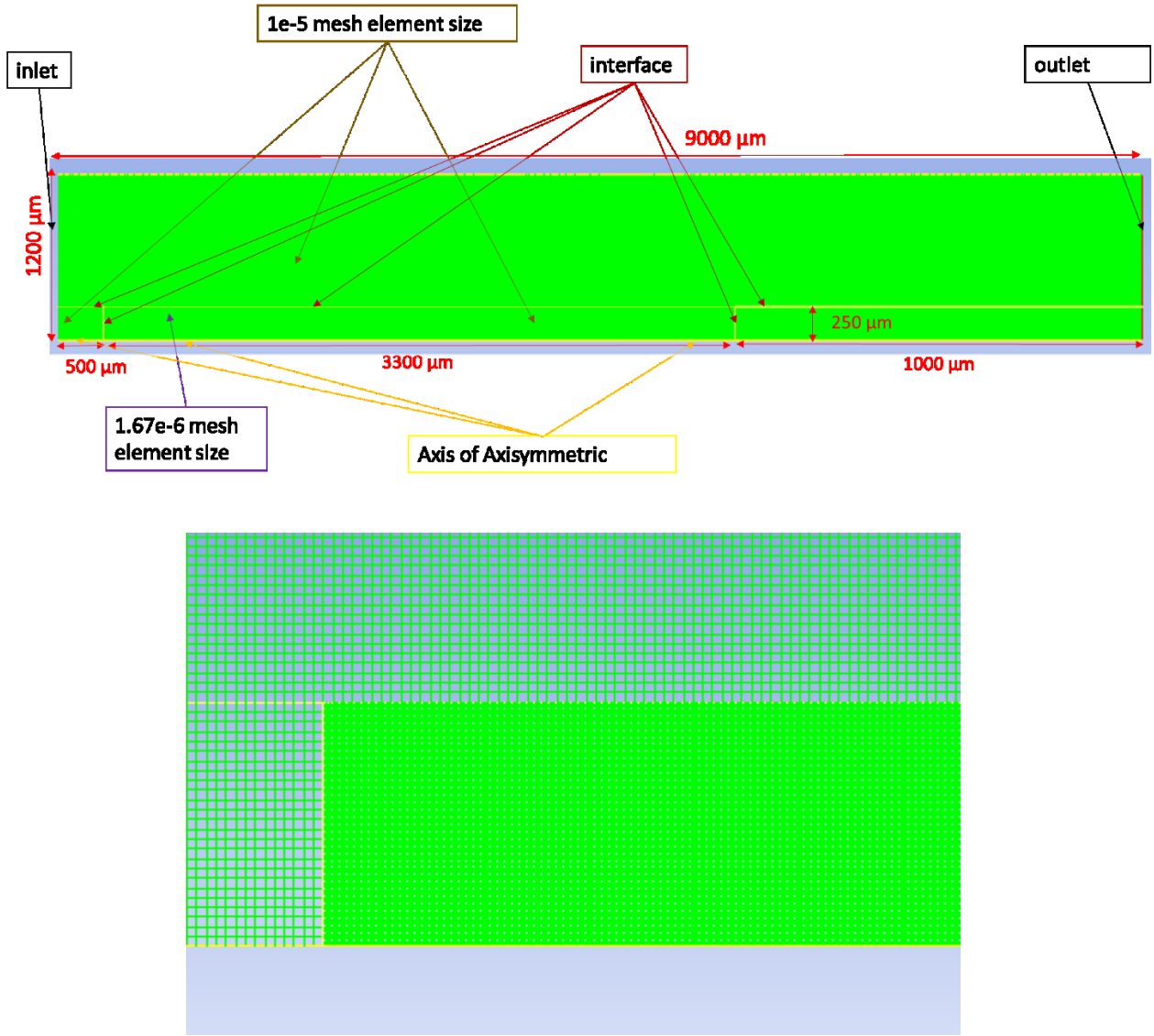

Figure 6.Computational mesh: Whole domain (upper) and close up of mesh density changes (lower). The droplet is represented by **60** mesh elements across the diameter

Figure 6 displays the mesh employed in this study. This mesh is divided into four regions which falls into two types of mesh-density regions: high density region (mesh element size of 1.67 μm) for where the droplet deformation occurs and lower mesh density region (mesh element size of 10 μm). The high mesh density region has a length sufficient for the droplet to breakup while the other region lengths are designed to give the flow sufficient time before encountering the droplet and room for the shock wave to develop. Another important advantage of this mesh is the capability of providing a sufficiently large domain compared to the droplet while keeping total number of mesh points to a minimum.

Dividing the region while carefully determining the mesh density of each region helps to minimize the total size of the mesh. Smaller total mesh size brings faster calculation compared to one uniform mesh element size in the whole domain. A uniform, one-size mesh-element method throughout the whole domain will require a much larger total mesh size in order to provide the same number of mesh elements across the droplet diameter. A consequence of dividing the region in this study is the inlet has two locations of the boundary condition with identical setting, an upper and lower part. The resulting flow from both inlet locations shows no difference. Another consequence is that the region needs to be connected using mesh "interfaces" that can be specified inside Fluent. The total mesh size is 308,423 mesh elements, with 60 mesh elements representing the droplet.

The high-density region provides 60 mesh element across droplet diameter. Each individual flow case uses a d = 100 μm droplet with its center located at 450 μm from the beginning of the high density region or 950 μm from the inlet. This is to ensure disruption to the flow, if any, caused by flow moving from a lower to a higher mesh density region will dissipate before reaching the droplet. The high mesh density region has height of 2.5 times the droplet diameter. This height means the outer edge of the bow shock will be in the low-density region, but this outer edge flow is sufficiently far from the droplet that it does not have an effect to the droplet. The effect of this to droplet deformation is estimated to be small

because the flow passing this thicker shock wave does not interact directly with the droplet. A detailed configuration setup of Fluent is presented in Appendix A.

2.4 Input Variables

Three primary non-dimensional parameters of this study are the Reynolds, Weber, and Mach numbers. Reynolds number will be held constant at $Re = 100$ for Weber numbers 50, 100, and 200. A Weber number of 100 will be the main focus of the study. Each of these *We* values was run for the three Mach number cases: $M = 2$ & $M = 1.5$ representing supersonic flow, and $M = 0.2$ representing low subsonic flow. The study is conducted at laminar $Re = 100$ in order for the simulation to use only the exact equations applicable to the case of laminar flow.

Laminar flow is thus chosen to avoid the need for modelling the turbulence using RANS (Reynolds-Averaged Navier-Stokes) or other turbulent modeling approaches. The case considered here is an internal, multiphase with a deformable droplet interface (fluid-fluid interface) at low Reynolds numbers, while various low Reynolds number RANS modelling in Fluent was developed for external flow with solid objects. Thus RANS modeling does not necessarily apply and might cause uncertainty in the main focus of this current work. But for validation purpose in higher Reynolds number cases, the k-epsilon with enhanced wall treatment RANS model, performed sufficiently well as can be seen in subchapter 3.1.1. Operating in the laminar region means level of confidence is high since laminar simulation uses exact equations. The study uses $Re = 100$, which theoretically in solid sphere will give a symmetrical standing vortex. This case is then suitable for 2D axisymmetric simulations.

In order to keep Weber number to be constant when varying the Mach number in each case ρ, v, μ, and T are adjusted to achieve the particular Mach number. Because the simulation only uses one droplet material for all cases, the droplet surface tension is kept constant. Given the very short durations of both the experiments and simulations considered in this work, the effects of viscous heating on the droplet temperature are not considered [4]. Thus the surface tension of the droplet fluid is taken to be a constant.

In most of the similar Mach number cases, the freestream velocity v is held the same to the extent possible and the freestream density ρ will vary. Using the "velocity inlet" boundary condition in Fluent, with a constant area domain, means that the operating pressure input has to be adjusted. A similar concept is used to keep the Reynolds number constant, but with dynamic viscosity of the flow altered, hence the use of artificial air in subchapter 2.3.

The first consequence from employing fixed values of the Reynolds and Weber numbers while having Mach number varies from supersonic to low subsonic is having two operating region in terms of operating pressure, viscosity and density. The supersonic cases consist of low density, low operating pressure, and low viscosity flows, while the subsonic case consists of high density, high operating pressure, and high viscosity flows.

Table 1. Properties Value Combination for Constant Re = 100 cases. Units: Density (kg/m3), Velocity (m/s), Dynamic Viscosity (kg/m-s), Temperature (K), and Operating Pressure (atm).

Intended Values:		Re	100	We	200			
Density	Velocity	Re	We	M	D Viscosity	D Viscosity ref	T (K)	Op Pressure (atm)
0.0776	738	98.72922	198.42	1.997	5.801E-05	5.000E-05	340	0.022
0.1391	556	95.23608	201.88	1.504	8.121E-05	7.000E-05	340	0.420
7.6282	74	97.31537	196.11	0.2	5.801E-04	5.000E-04	340	7.340

Intended Values:		Re	100	We	100			
Density	Velocity	Re	We	M	D Viscosity	D Viscosity ref	T (K)	Op Pressure (atm)
0.0389	722	99.95	95.20	2.00	2.810E-05	2.500E-05	325	0.011
0.0663	553	98.76	95.19	1.50	3.712E-05	3.200E-05	340	0.021
4.1876	72	99.35	101.92	0.20	3.035E-04	2.700E-04	325	3.800

Intended Values:		Re	100	We	50			
Density	Velocity	Re	We	M	D Viscosity	D Viscosity ref	T (K)	Op Pressure (atm)
0.0212	741	95.02478	54.65	2.005	1.653E-05	1.425E-05	340	0.007
0.0343	556	95.29661	49.781	1.504	2.001E-05	1.725E-05	340	0.011
2.1224	74	95.00397	54.565	0.2	1.653E-04	1.425E-04	340	2.060

The second consequence was the need to use a pseudo air for the inlet flow medium. This pseudo air has all the same properties of air except the dynamic viscosity, which is adjusted to obtain the desired constant Reynolds number. The correct combinations of density, velocity, temperature, and dynamic viscosity are found using a self-written Matlab code to brute force the combination. Table 1 presents input values and the desired flow properties in each case.

To assess the validity of continuum assumptions on the simulation conditions, the Knudsen number is calculated using equation (7)

$$K_n = \frac{\lambda}{d} = \frac{M}{Re}\sqrt{(\frac{\gamma\pi}{2})}\,, \tag{7}$$

Where λ is mean free path of gas, L is characteristic length of droplet diameter (100 μm), M is Mach number, Re is Reynolds number.

The research is meant not to be in the visco-elastic region. In order to ensure this, the non-dimensional Ohnesorge number Oh is checked using Eq. (4) with the following values of μ_d = 0.002311 kg/m-s, ρ_d = 785.16 kg/m^3, σ = 0.0213 N/m.

For Re = 100, the Knudsen number is below 0.032, while the Ohnesorge number (Oh) for 2-propanol is 0.0565, i.e., both much smaller than unity. Hence, continuum and non visco-elastic assumption are valid.

2.6 Code Validation For Fluent

In order to build confidence in Fluent's capability for this study, validation is conducted by running a few types of cases. These cases are chosen to test fluent capability in handling certain aspect of the flow i.e. different gases, compressibility, droplet deformation, and shock wave interaction.

2.5.1 Shock tube

The shock tube is a convenient and fundamentally important way to validate a numerical code due to the variation of physical events that happens inside a shock tube. A few such events to mention are regions with very different values of pressure, density, velocity, and temperature; a region with compression of the gas, a region with expansion of the gas, and even different type of gas in the expansion and compression region. All these different physical events will show how the code can handle multiple types of physics.

The initial conditions and expected results from the shock tube are calculated using shock tube equation [21]. Figures 7-10 shows the comparison between Fluent and analytical result from shock tube equations. As can be seen, the result match well. The small depression that appears in Figure 5 and 9 corresponds to the contact surface, which separate the helium and air. This is predicted in numerical calculation but not in the analytical equations. The analytical equation assumes that the contact surface is infinitely thin in width, so the dip will not be seen by the analytical equations. The behavior is also seen in other study [22]. Part of the validation result are shown in the next chapter.

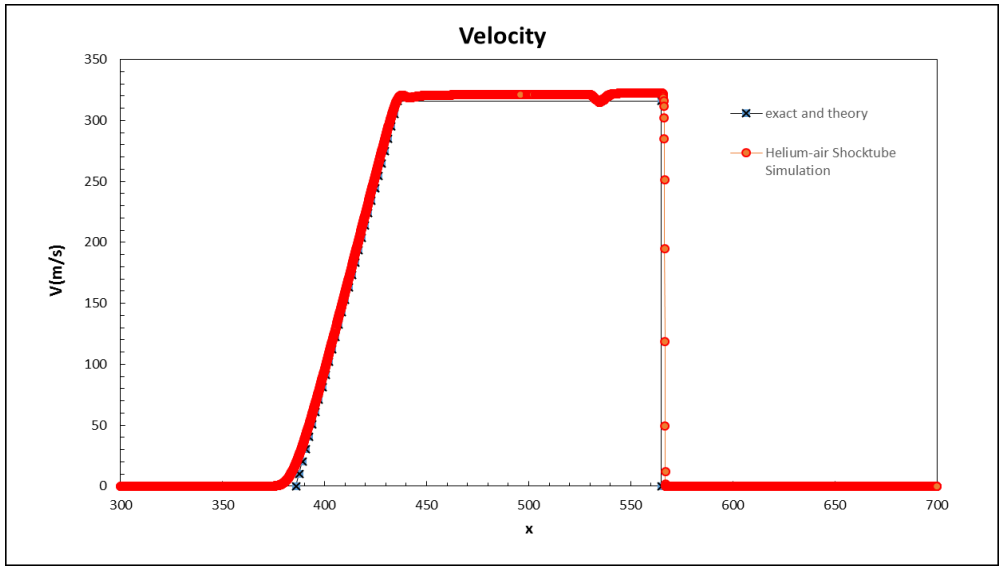

Figure 7. Fluent vs Analytical result of velocity evolution in a helium-air shock tube

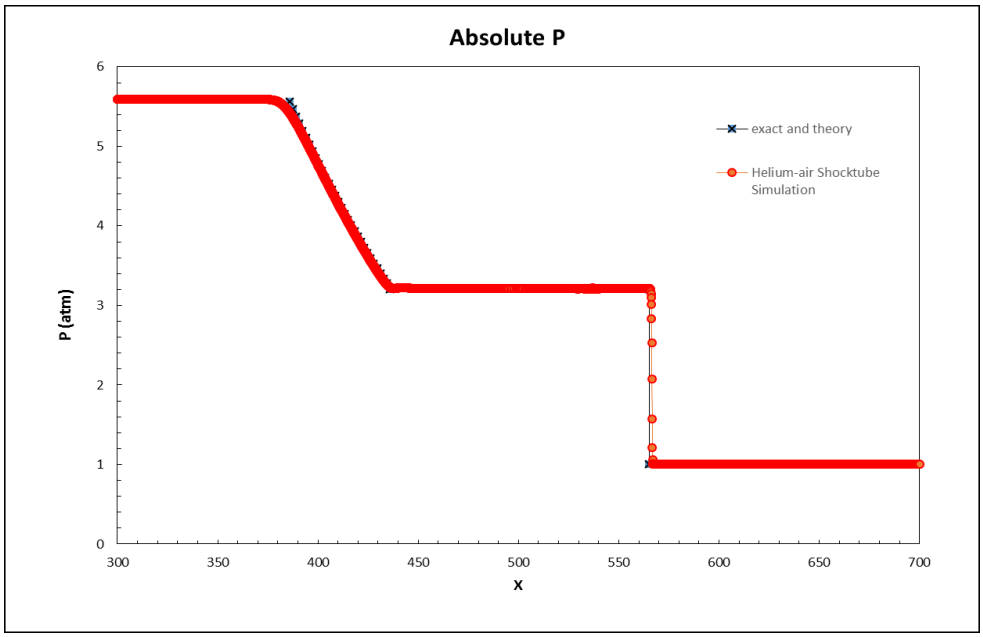

Figure 8.Fluent vs Analytical result of pressure evolution in a helium-air shock tube

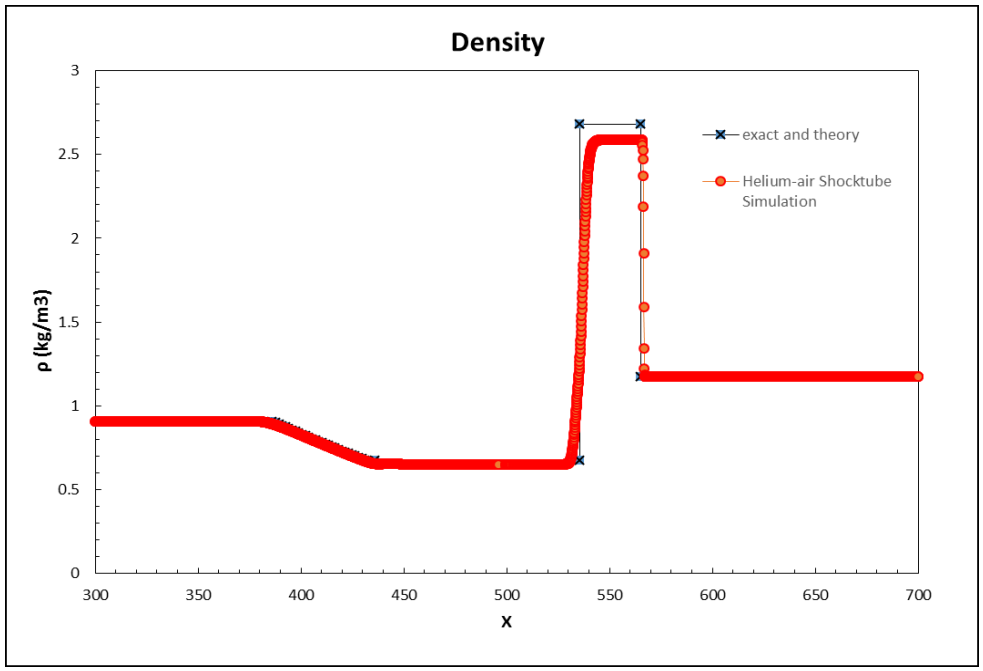

Figure 9.Fluent vs Analytical result of density evolution in a helium-air shock tube

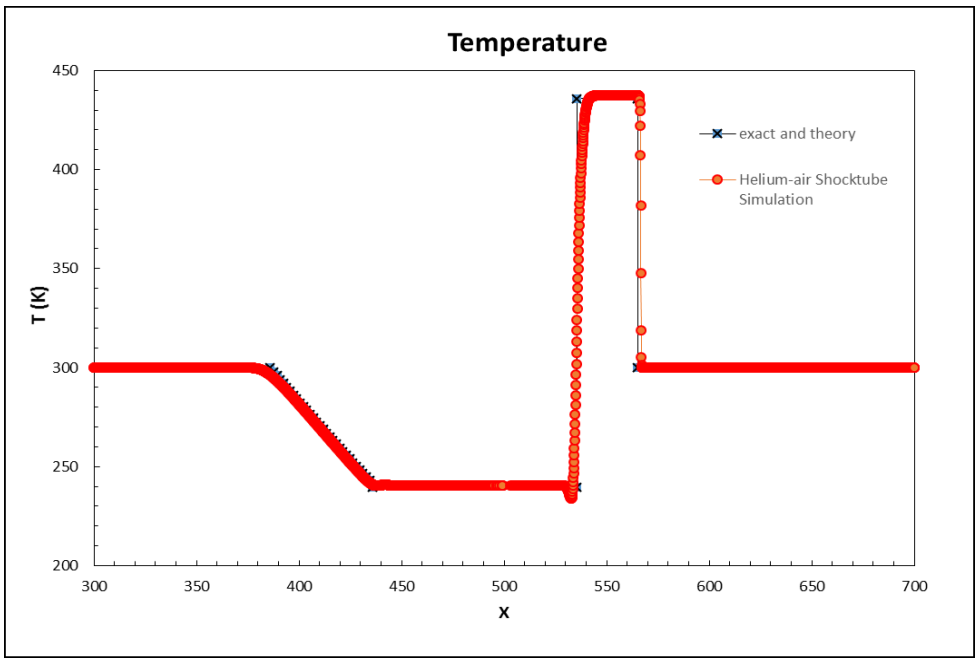

Figure 10. Fluent vs Analytical result of temperature evolution in a helium-air shock tube

Chapter 3 Results and Discussion

3.1 Validation with Comparison Cases

3.1.1 Engel's Experiment Comparison

Investigation of Fluent's capability to replicate droplet deformation was done by conducting a simulation using conditions of Engel's experiment [2]. The experiment was a water droplet deformed using an air shock tube with a helium driver gas. The 2D axisymmetric Fluent mesh was divided into four main regions: an expansion and a contact surface region, a compression region, a droplet-free test region, and a droplet deforming region. This mesh is capable of representing a 2.7 mm diameter water droplet with 50 mesh elements across its diameter, while minimizing total mesh size.

This simulation used a method where the properties of the shock tube flow has been started which are patched into the calculation domain, instead of letting the shock tube flow develop from the beginning. The values of a running shock tube were calculated using the shock tube equation to calculate density, velocity, static pressure ratio, temperature, u_2 (velocity of flow after the shock wave), M_s (Mach number of the shock wave), M_2 (Mach number of flow after the shock wave), and M_3 (Mach number of flow after the contact surface). These values were then patched-in as initial condition with Fluent's "patched" option. There are four regions of patches with the length of each region calculated to provide the droplet enough flow time for the droplet to break up completely. This guarantees that the flow encountering the droplet has the same properties as in the Engel's experiment, which the simulation reproduces. A shock speed of M_s =1.7 (M_2 = 0.767 or u_2 = 315.8 m/s) was chosen with a 2.7 mm-diameter water droplet. The downside is the expansion fan is not initially captured between region 4 (helium expansion region) and 3 (after the contact surface region), but the expansion fan is of no interest for this simulation and it does not affect the properties in the vicinity of the droplet. This method reduces the computational time significantly, from a predicted two and a half weeks to only a week.

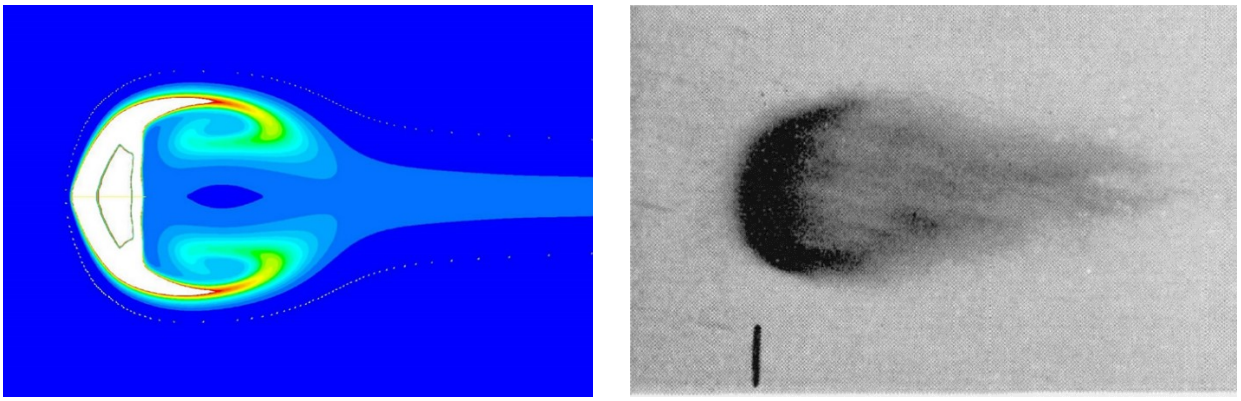

Figure 11. Comparison between the current simulation result (left) and Engel's experiment (right). Water droplet with d = 2.7 mm. We= 9000. Re = 103000. M_{air} = 0.77.

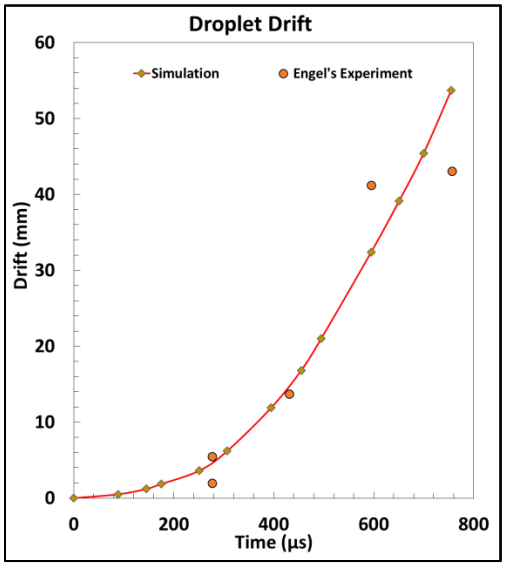

Figure 12. Droplet Displacement

The similarity between the simulation result and Engel's photograph is depicted in Figs. 11 and 12. The numerical calculation produced a qualitatively similar image as Engel's [2]. A lenticular shape occurs when the windward interface takes on a hemispherical shape and the backward interface is relatively straight, which Fig. 11 displays. The simulation result has a small, sharper nose at the windward associated with the axisymmetric nature of the simulation. While the main droplet is hemispherical in shape, the flanks area has been extended in Fig. 11 to highlight stripping. But overall shape is similar to a lenticular shape. Both images show that water is mainly being stripped from the flanks of the droplets. The finer mist of

water that seemingly comes from the center of the droplet is actually coming from the flanks. To display this phenomenon, a planar image would need to be taken, which was not applicable to the experiment. Because the value of the Reynolds number, RANS modelling was used in this case. But the similar shape in this comparison suggests the RANS model was adequate in this case.

3.1.2 Boger *et al.*'s Experiment Comparison

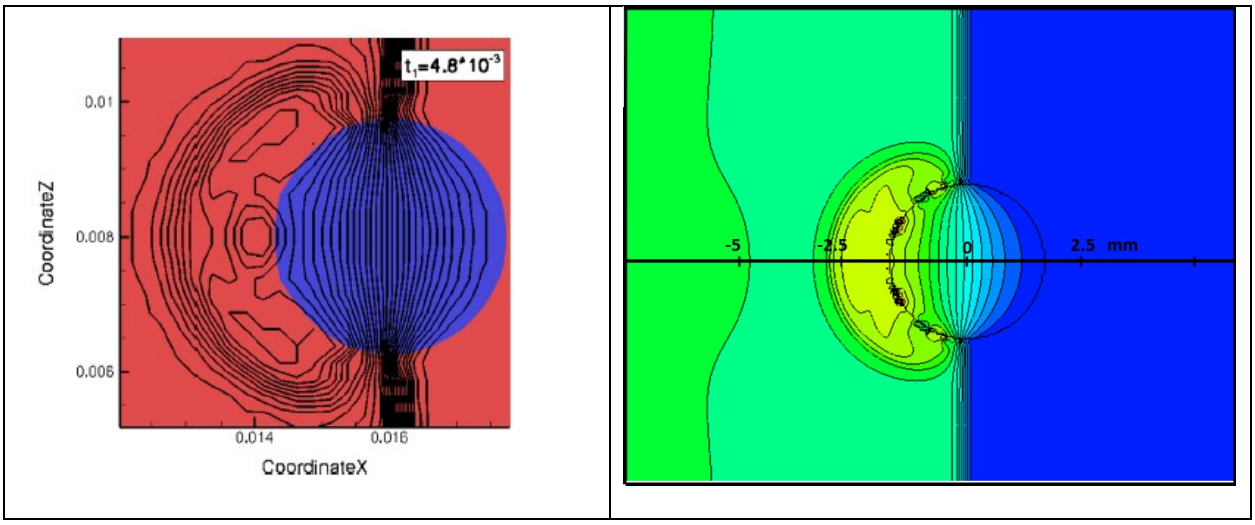

Figure 13. Pressure Contour Lines of Shock Wave Passing Droplet: Boger *et al.'s* (Left) [22] and Current Simulation (Right). r = 1.75 mm. Re = 23000.

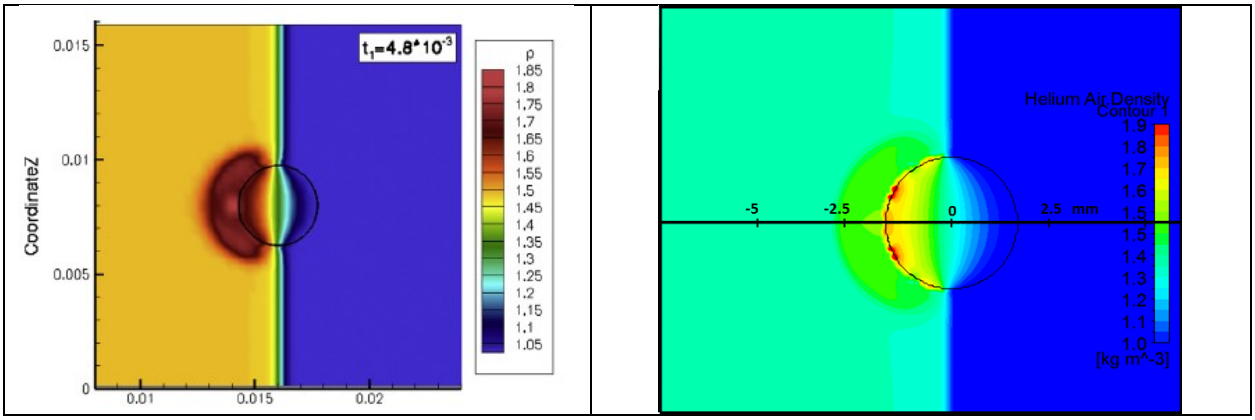

Figure 14. Density Distribution of Shock Wave Passing Droplet: Boger *et al.'s* (Left) [22] and current Simulation (Right). r = 1.75 mm Re = 23000.

Boger *et al.* performed a DNS simulation to observe shock interaction with a droplet to validate their code improvement in compressible flows [22]. This style of validation suggested checking Fluent's

capability to model shock reflection, where Fluent here again used a RANS model. The high values of Reynolds number suggested that RANS was needed. However because the run was only to the point where the shock wave was still in the middle of the droplet, RANS did not in fact play any major role in this case. This simulation required a "custom field" to extract the pressure gradient and a UDF (user defined function) for the density gradient. The purpose of the UDF was to specify that Fluent store density gradient values for each time step, which Fluent does not do natively. The condition of the shock tube was calculated and set to produce the same flow properties as shown by Boger *et al.'s* simulation. The results are seen in Figure 13- 15.

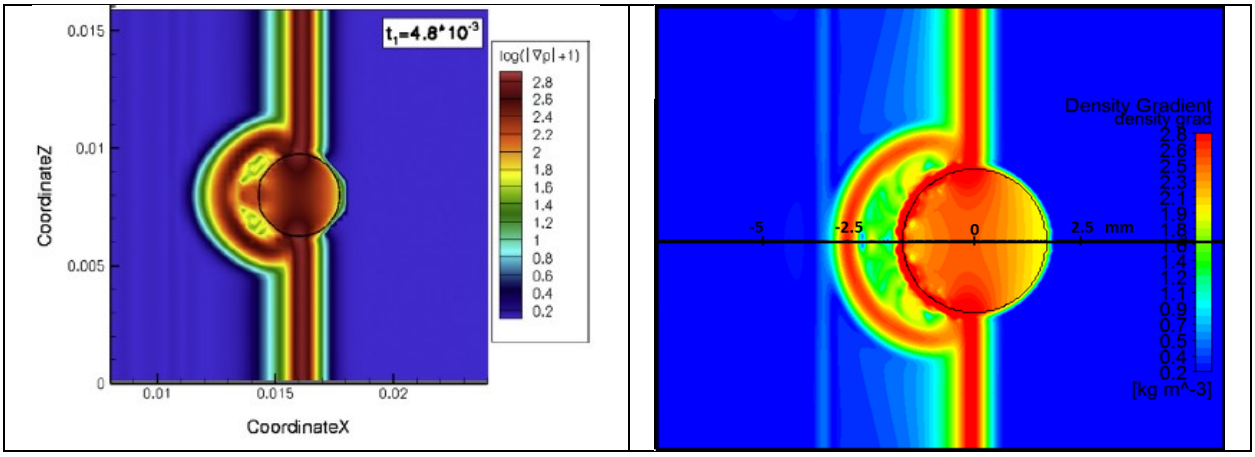

Figure 15. Density Gradient (log(|∇ρ|)+1) Distribution of Shock wave Passing Droplet: Boger's (left) [22], current simulation (right). r = 1.75 mm Re = 23000.

Based on these images Fluent appears to be capable of reproducing the major parts of Boger *et al.'s* results, with some differences in the small scale physics [22]. Because Boger *et al.* only gave result in these images without stating their values, the comparison is qualitative between the color code of this study and their study. For example, the value range of density gradient is similar between the two simulations, and it can be visually observed that the current results also present a high density gradient at the top and bottom of the droplet and also at the reflected shock wave. For the density field shown in Fig. 14 the color code style might be different, which causes the main flow density to have different color representations. But careful observation of the values that each color code represents clarifies that they refer to the same value.

A lower initial density value, due the difficulties on setting the initial values as exact as theirs, also contributes to the slightly lower value. However, trends in terms of density gradient and pressure are reasonably similar. Fluent does exhibit the oscillating pressure lines, seen as dark spots in Fig. 13 at the interface which Boger *et al.*'s novel code manage to avoid. There appear to be some small details that this simulation does not have the resolution to display, such as the fine details behind the reflected shock. It should also be pointed out that the DNS nature of Boger *et al.* code reveals more fine details than are available from the Fluent simulation. But for the most part, Fluent is capable to re-produce the results, in terms of early value distribution especially density gradient, and pressure. Neither simulation here was conducted over a sufficiently long time to have any implications for the droplet deformation.

3.2 Droplet Breakup: Supersonic vs. Subsonic Cases

In this section the effect of varying Mach number on droplet deformation and liquid shedding is considered for droplets with fixed values of Weber and Reynolds numbers. As described in Chapter 2, the flow originates from a velocity inlet, which makes the simulation similar to a wind tunnel experiment. The Reynolds number is kept at 100, which puts it in laminar regime hence RANS is not used. The flow variables are described in detail at chapter 2.

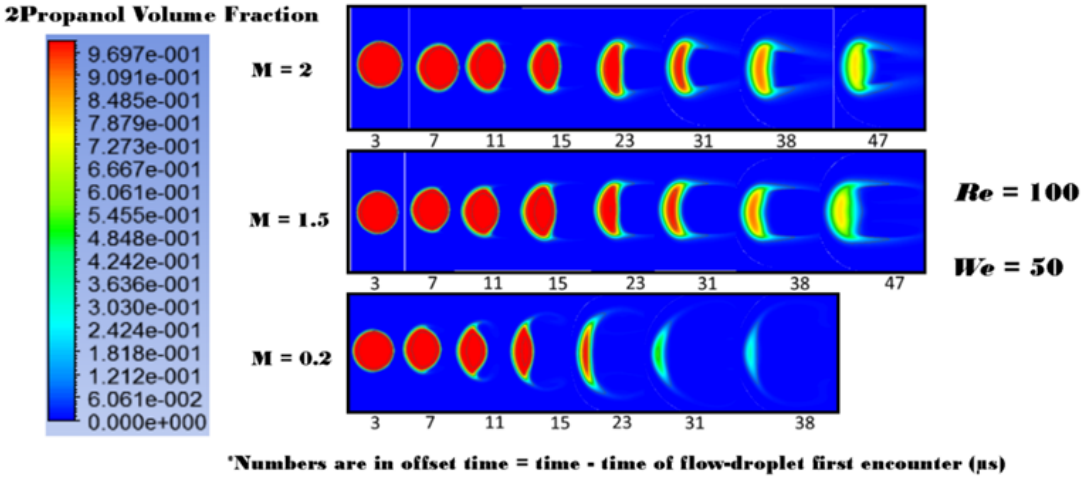

Figure 16. Droplet Breakup for different Mach numbers for *Re* = 100, *We* = 50. Flow moving from left to right. A volume fraction of unity is 100% isopropanol.

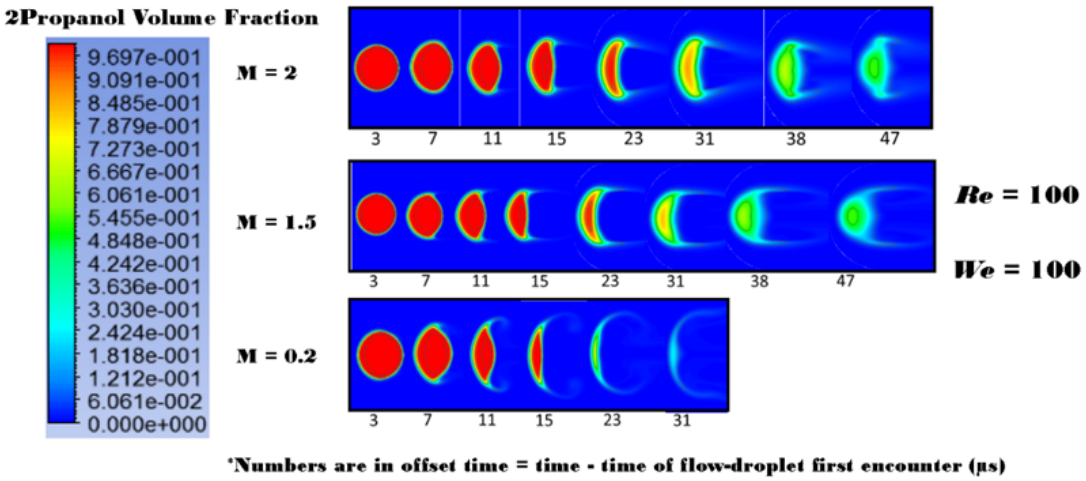

Figure 17. Droplet Breakup for different Mach numbers. For *Re* = 100, *We* = 100. Flow moving from left to right. A volume fraction of unity is 100% isopropanol.

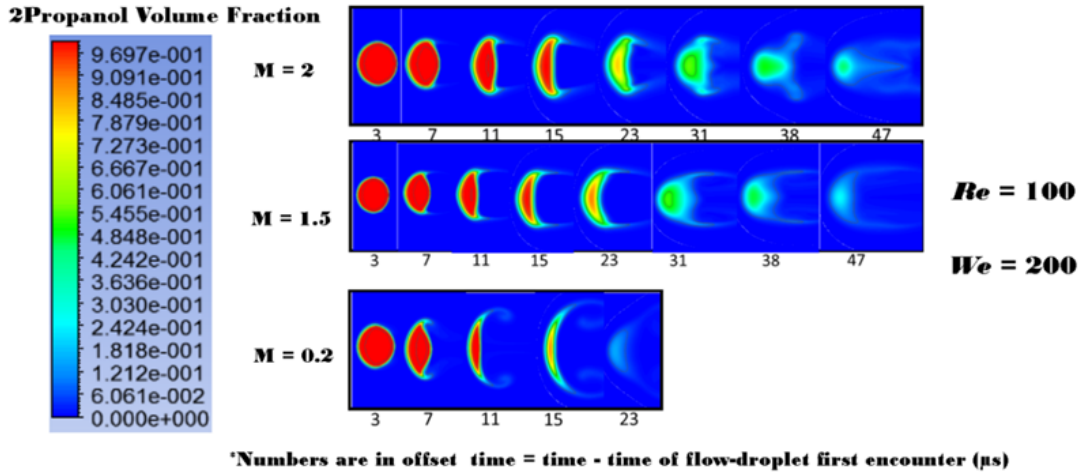

Figure 18. Droplet Breakup for different Mach numbers. For *Re* = 100, *We* = 200. Flow moving from left to right. A volume fraction of unity is 100% isopropanol.

All cases shows stripping breakup as the breakup mode but the supersonic and subsonic cases present different details within the stripping breakup, as seen in Figs. 16-18. These images suggest there are consistent differences in the droplet breakup details between supersonic and subsonic flow for all Weber number cases. The first difference is droplet breakup in supersonic flow appears to have lower deformation than the ones in subsonic flow for a similar offset time and fixed value of Weber number. The second difference is that the lifetime of the droplet in the supersonic case is generally longer than in the subsonic

case, which suggests that compressible flow, for the same value of Weber number, in fact delays complete breakup. The droplet lifetime, in terms of the highest droplet volume fraction at selected offset times, decreases faster in the subsonic case than in the supersonic case, as seen in Figs. 16-18. This can also clearly be seen by the droplet volume fraction distribution in these two Mach number cases.

The choice of the two iso-lines in Figs 19 and 20 guarantees that the deformation is evaluated in areas where the fluid is nearly pure isopropanol or reasonably close near unity. Depending on the choice of reference iso-line, the volume fraction values will dissapear faster than when using a lower droplet volume fraction iso-line value. Figs. 19 and 20 show quantitatively the degree of droplet deformation, calculated by following iso-line 98% and 90% droplet volume fraction which follows Theofanous *et al.*'s definition where deformation is defined by the droplet's vertical length (L_y) over its horizontal length (L_x).

The supersonic flow cases, both M = 1.5 and M = 2, consistently show lower deformation for a given offset time. Noting Figs. 19 and 20, lines representing subsonic cases are consistenly to the left side of the lines representing supersonic cases, which means that the subsonic case has faster deformation than the supersonic case. To the best of our knowledge, this is the first time that this behavior has been revealed. The current simulation is the opposite of the result reported by Thefanous *et al*, where their supersonic cases have faster deformation rates than are seen under subsonic conditons, as shown in Fig. 21 [6]. However, their cases were not for constant Reynolds number as is the case in this study. Their estimated Reynold number range for supersonic flow is 300-3300, for subsonic flow it was 231. It is difficult to establish the exact cause for the differences since they do not describe flow field for their isolated drop cases in detail as presented here. One possible cause from this current study is the fact the supersonic flow was run at a much lower ambient pressure which may cause the deformation to be slower in this supersonic case.

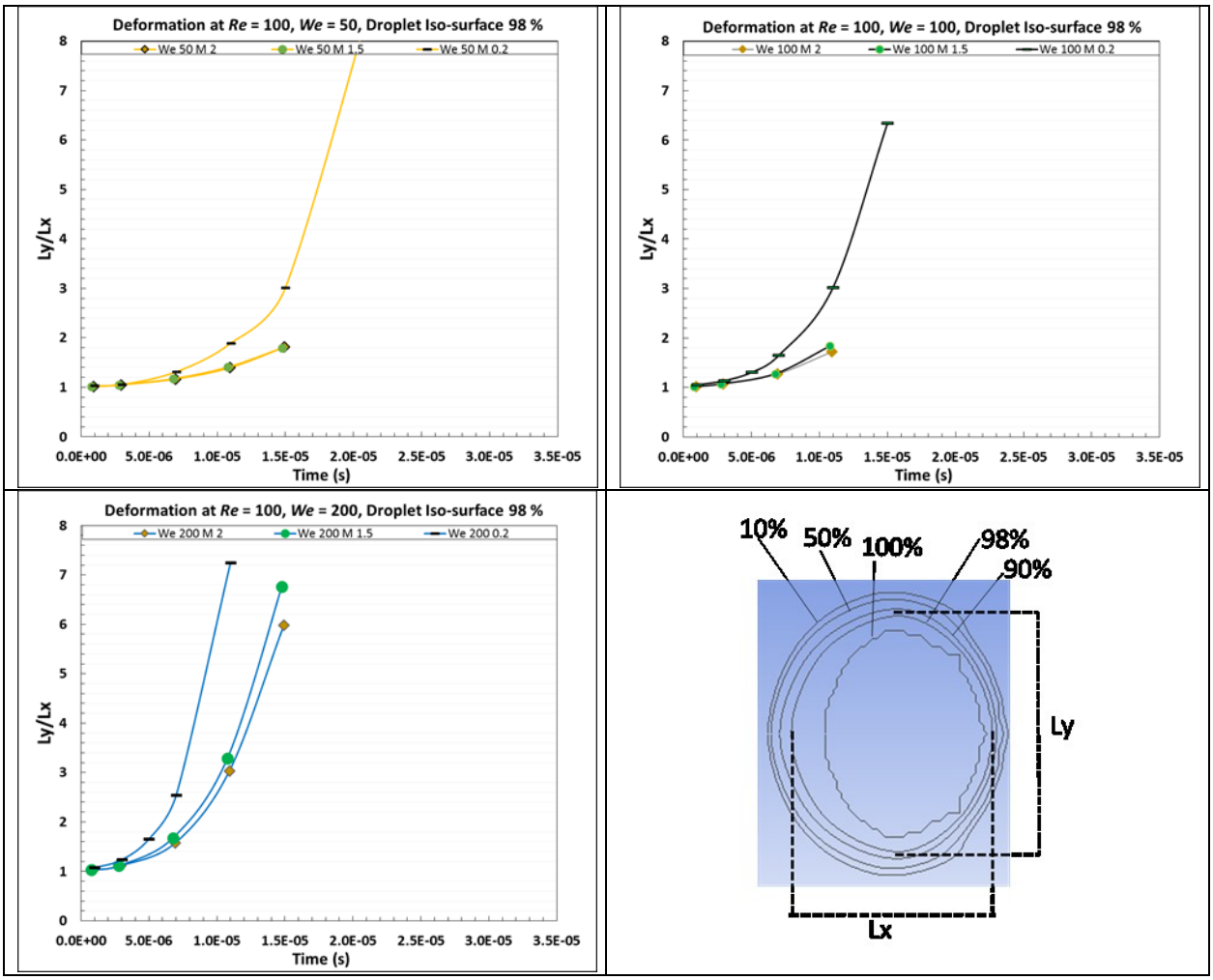

Figure 19. Droplet deformation (*Ly/Lx*), based on the iso-line of 98% droplet volume fraction (bottom right figure).

For *Re* =100.

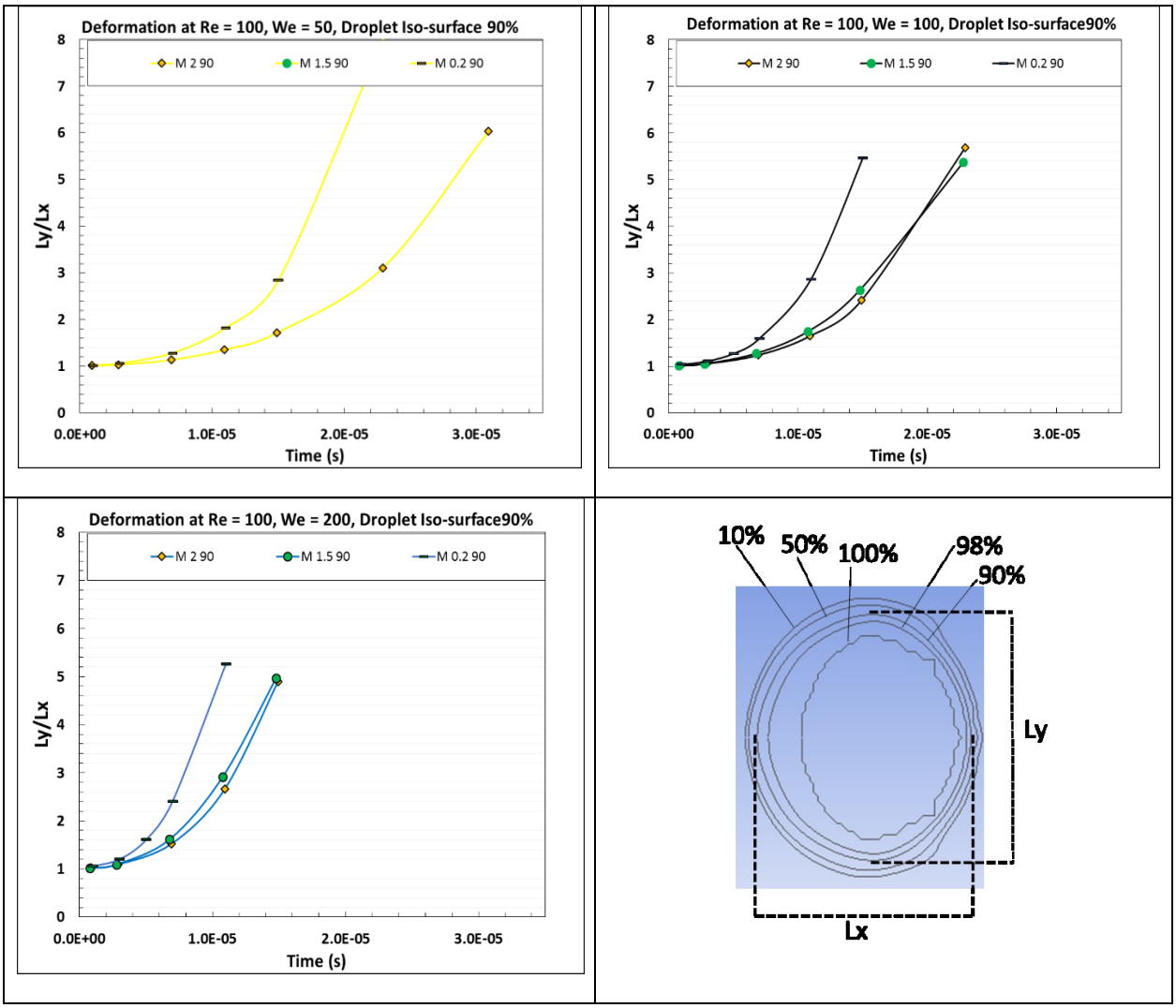

Figure 20. Droplet deformation (Ly/Lx), based on the iso-line of 90% droplet volume fraction (bottom right figure). For *Re* =100.

The effect of Weber number is also apparent in deformation and lifetime, as seen in Figs. 16-18. As Weber number increases the deformation rate and decreases the droplet liftime. This is consistent with the more rapid disruption expected for higher Webers number, and that this study has a constant Reynolds number suggests that this is not a viscous effect. This effect is more prevalent in subsonic than supersonic cases which supports the trend that droplet deformation and breakup is delayed in compressible flow for a fixed value of Weber number. A similar impact on droplet lifetime is seen in Fig. 22, where the time evolution of the maximum droplet volume fraction is shown. With these results, it can be said that the effect

of increasing compressibility overall, for fixed Weber number, is to inhibit deformation and delay the complete breakup, as seen at Fig 22.

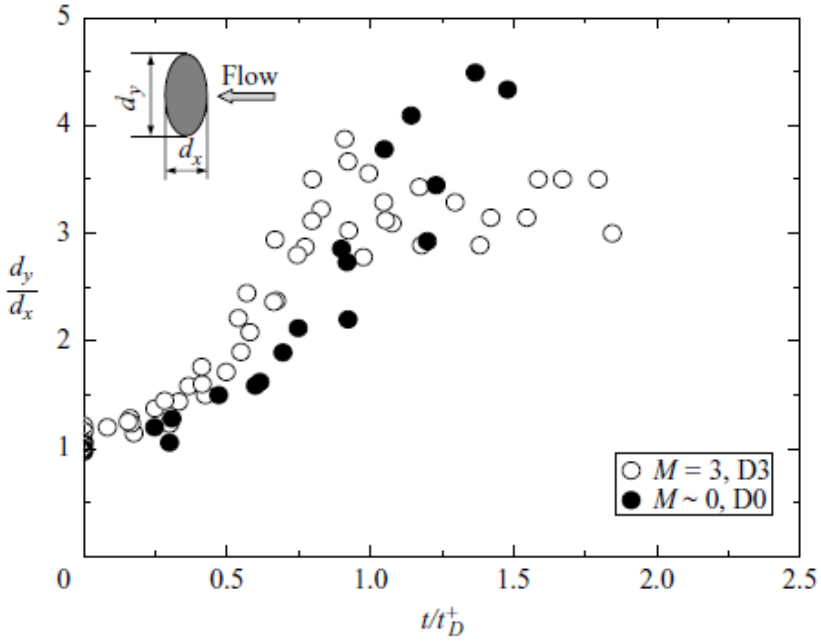

Figure 21. Droplet deformation in supersonic and subsonic flow by Theofanous *et al*. [4] *dy* and *dx* are similar to the length scales *Lx* and *Ly*, respectively.

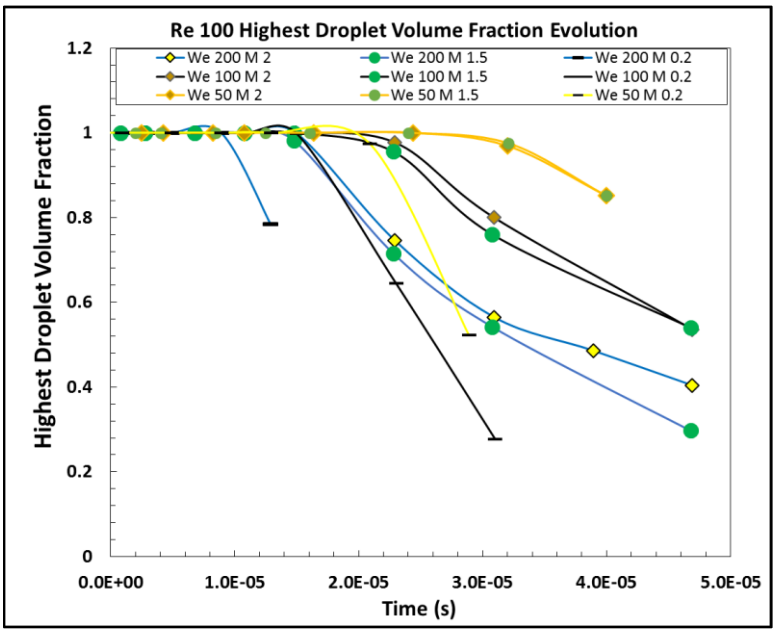

Figure 22. Maximum droplet volume fraction evolution with time for *Re* = 100

Another point to notice is the actual breakup mode does not seem to change drastically between the supersonic and subsonic case, in the sense that the expected stripping breakup for these values of Weber number is observed. A droplet with a Weber number of 50 does not undergo bag breakup here, but it is known that bag breakup is difficult to produce especially for low values of the Ohnesorge number *Oh* even in experiments.

The actual Weber number seen by the droplet may be different than the value defined based on the upstream flow for the case of supersonic flow, where a bow shock wave is present. The bow shock allows for calculating a Weber number on the flow center line. The common practice is to take the Weber number based on variables values at freestream. But a shock wave changes the value that the droplet sees from the freestream condition, which might lead to an alternate way of defining the Weber number. Figure 23 shows the jump inWeber number upstream and downstream of the bow shock wave, based on the changes in density and centerline velocity, which can be considered significant especially in the $M = 2$ cases. The downstream Weber number drops to a lower value, to about a half of the freestream value. If these post-shock wave Weber number values are compared to those for droplets based on the freestream Weber number, on a droplet with sufficient *Oh* that is still below 0.1, it will suggest a bag or bag-stamen breakup. But the fact that the breakup mode does not changes into a lower *We* type of breakup mode, such as bag stamen breakup, may be a consequence of the low *Oh* and the fact that the off-centerline velocity in compressible flow downstream of a detached bow shock wave can be significantly higher than the on-centerline value, resulting in higher aerodynamic forces on the droplet than would be suggested by the Weber number alone.

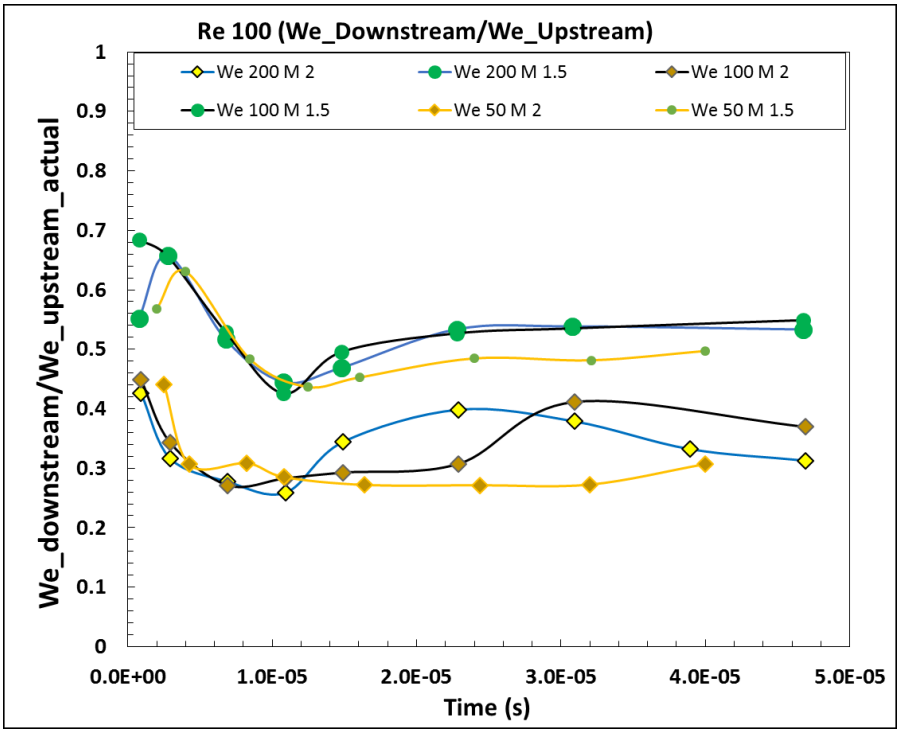

Figure 23. *We_downstream/We_upstream* for *Re* = 100

Because Fluent needs to avoid instabilities in compressible flows with low density, the program creates a precursor flow which has values that are a somewhat lower than the intended values. However, this precursor flow is short in duration, around 1-2 μs depending the intended Weber number and the precursor flow does not happen in incompressible cases ($M = 0.2$). Despite this, the initial Reynolds number upstream stays near the intended value, with a deviation averaging ± 8 counts. As the droplet accelerates and moves, the Reynolds number decreases because the droplet-air relative velocity decreases. This Reynolds-number invariance is expected for a constant freestream flow and this is how most contant-flow experiments are performed. This is also true for Weber number, where the upstream Weber number overtime is still close to its intended value, *We* = 100. Hence, these cases are still considered constant *We* = 100 cases. The same is also applicable in other intended Weber case. The simulation has the evaporation model turned off in Fluent, so the interface smearing seen in Figs 16-18 are mostly numerical. Ideally, the interface between two fluid phase in VOF is clear and thin, as explained by Dodd & Ferrante [19]. In this ideal state, the droplet volume fraction (C) should have values of $0<C<1$ only at one cell. This is only

achieved in Fluent if the more advanced type of volume fraction is used, such as the "geometric-reconstruct" of explicit scheme or the "compressive" of implicit scheme. Experiences shows, that these sharp method are highly unstable, prone to sudden unstable courand number jumps, and require very low time step compared to first order upwind method, which can be 10x lower. Another point is these sharp method do not always gave better stripping visualization, such as in Engel's case fine mist-like stripping.

The current study used the first order upwind volume fraction treatment scheme. This scheme is the most stable method and provided better stripping visualization on the Engel's case [2], seen in Fig 11. This approach loses volume fraction by "smearing" rather than throught daughter droplets. This explains why the result in Figs. 16-18 shows the stripping to appear as a mist-like visualization. This "smearing" causes regions where the droplet volume faction to have values of $0<C<1$ in more than one cell (mesh element).

The current study focuses on the primary flow physics that drive differences in deformation trends between the supersonic and subsonic cases. The details such as the actual stripping mechanism, droplet fragmentation, size of doughter droplet, and droplet windward-interface instabilities were not the main concern of this current study. Hence, the first order upwind volume fraction treatment is sufficient to give information about the different general trends of the droplet in subsonic and supersonic flow with also the primary flow physics that underlie those differences, at short early offset time of the deformation. In Figs 16-18, the red color codes area indicates with $C > 0.9$ where droplet can be considered not to have lost fluid massively yet, so there is confidence in discussing the physics up to offset time 15 μs. The details mentioned before can be addressed in future studies using the more advanced volume fraction treatment when the computing resource required becomes available.

3.3 Flow Fields and Breakup mechanisms

3.3.1 Pressure Distribution and Viscous Stress

One distinction between supersonic and subsonic cases is the pressure inside the droplet, as can be seen in Fig. 24. The difference in pressure gives a first hint to the source of the different deformation behavior observed. The pressure inside the droplet is connected to the pressure distribution around the droplet. For example, the stagnation point pressure influences the pressure inside near the windward surface as also seen in the Boger *et al's* study for their code validation on shock-droplet interaction [22]. The pressure distribution within the droplet is similar to that shown by Theofanous *et al.*, indicating this difference in pressure is expected in both supersonic and subsonic flow, albeit their Reynolds number is different than that of the current study [6]. The different pressure distribution will be described using solid sphere comparison because the pressure distribution inside is connected to the pressure distribution outside and the pressure distribution between solid sphere and droplet is very similar, at least for the very early stages of droplet deformation. This discussion will be extended later on in the solid sphere comparison discussion, subchapter 3.3.2.

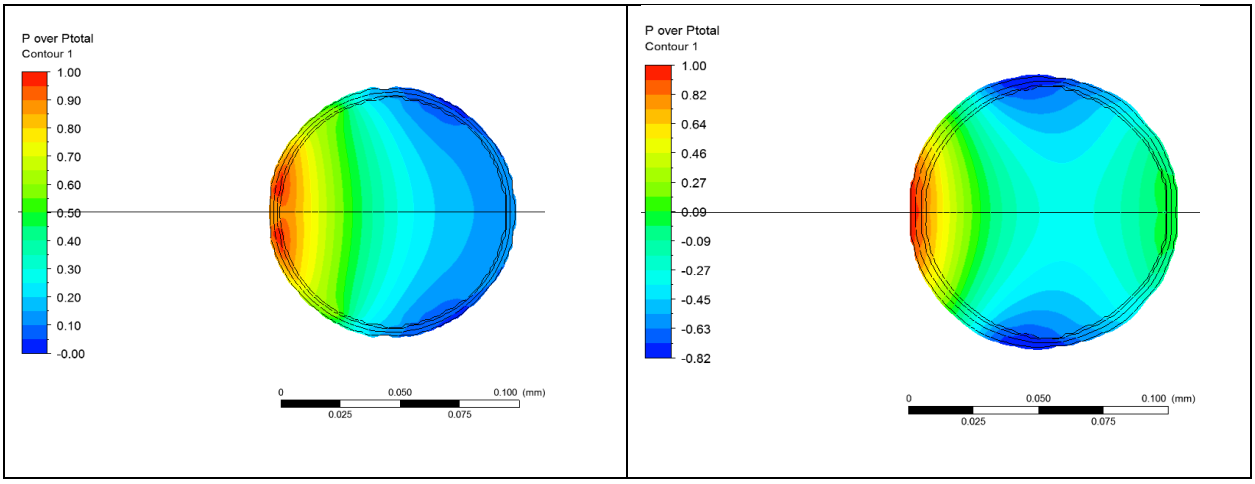

Figure 24. Current study droplet pressure distribution in the early stages $M = 2$ (left), and subsonic $M = 0.2$ (right). 2propanol droplet. Droplet size $d = 100$ microns. $Re = 100$. $We = 100$. Offset time: 1 µs

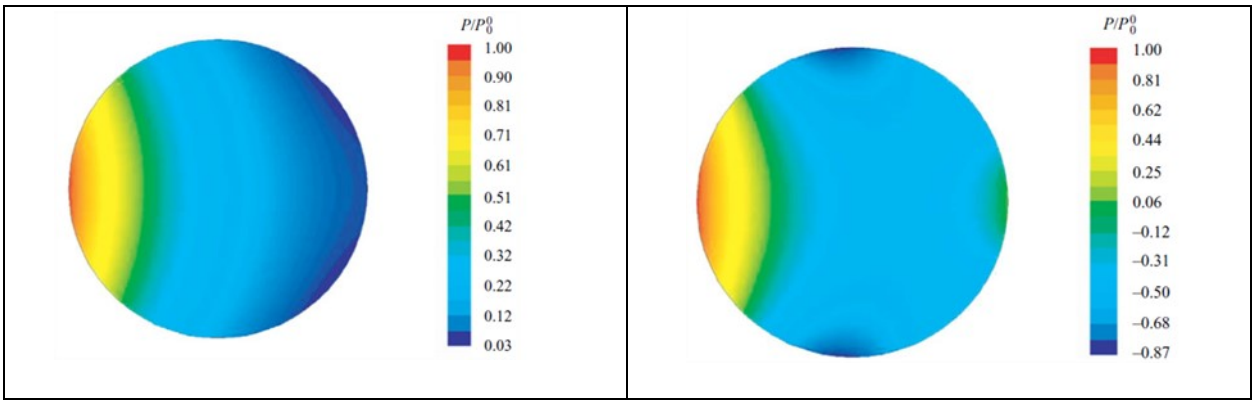

Figure 25. Theofanous *et al's* droplet pressure distribution in the early stages [4]. $M = 3$ (left), $45 < We < 495$, $210 < Re < 4166$ and subsonic $M = 0.11$ (right), $7 < We < 100$, $210 < Re < 4166$. $Re = 100$.

In the early stages of droplet disruption in the subsonic case, offset time = 1 μs, , the lowest-pressure region occurs at the top-bottom edge of the droplet in this 2D axisymmetric simulation, while the high pressure regions reside at the windward sides of the droplet, as seen in Fig, 24. The resulting pressure gradient within the liquid causes the droplet to deform or flatten. The top and bottom edges are stretched vertically, normal to the freestream flow direction, with the windward and leeward interface being pushed simultaneously towards the center of the droplet. "Humps" subsequently appear at the top and bottom of the droplet as a result of the limited area of the low pressure, as seen in Fig, 26. The motion of stretching vertically and decreasing in horizontal center line results in the high deformation values (*Ly/Lx*) as seen in Fig. 19.

The supersonic cases have some different details in the pressure distribution compared to the subsonic cases, as seen in Figs 26 and 27. First and most important is that at the early stages the lowest-pressure region in supersonic flow occurs further back in the leeward interface, compared to the near top and bottom of the subsonic cases. The "humps" appear, but develop not vertically but rather horizontally as the droplet undergoes deformation. Contrary to the subsonic cases, initially, the lowest-pressure region in the supersonic case is located towards the droplet leeward side low pressure regions and stays at the leeward interface.

Observing the pressure distribution in each flow regime in Fig. 26, droplets in the supersonic case have two areas where there are considerable pressure differences. The supersonic cases have distinct divisions which separate the pressure difference at the windward side from the pressure difference of the leeward side of the droplet. The locations of these two areas remain generally the same as time progresses, as seen in Fig. 26 and 27. In subsonic flow, the two areas are at the windward droplet surface due to the stagnation point (high pressure) and the top-bottom region (low pressure) due to flow acceleration. However, unlike the supersonic case, the lowest-pressure region move in the subsonic case, especially the ones that are initially located at the top-bottom of the droplet surface.

For Figs. 26 and 27, some definition of pressure is needed:

$P_{static\_gauge} = P_{absolute\_total} - P_{dynamic} - P_{operating}$

$P_{absolute}$ = Pressure relative to vacuum. This pressure is the one used in gas law calculations.

$P_{operating} = P_{absolute} - P_{statuc\_gauge}$

To give a better understanding of the operating pressure ($P_{operating}$), an example is given here. If an experiment is conducted in an open space, the operating pressure is atmospheric pressure. If an experiment is conducted in a pressure vessel, the ambient pressure inside the vessel is the operating pressure.

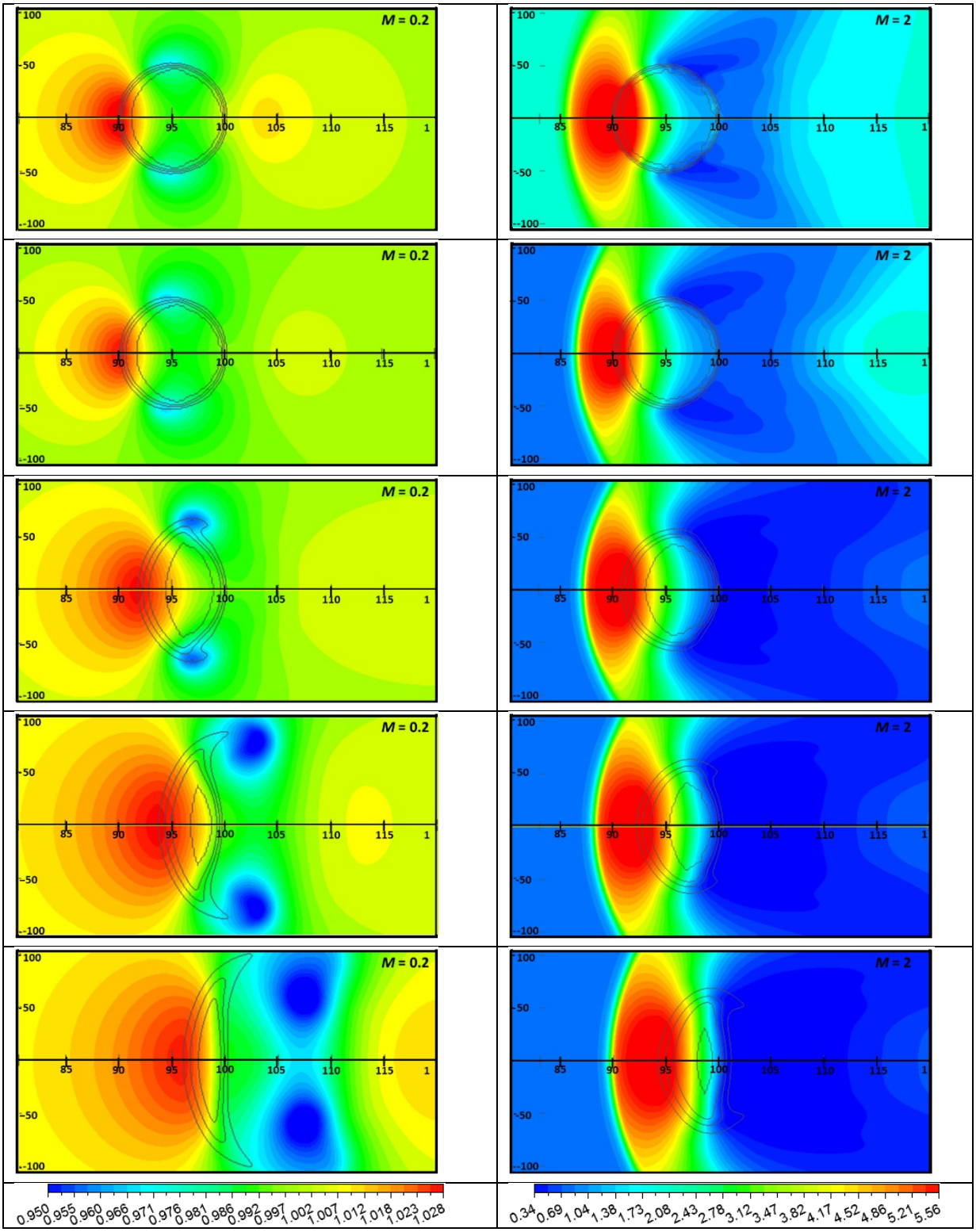

Figure 26. Normalized pressure *(Pabsolute/P(absolute_infinity)):* Subsonic (left) and Supersonic (right). *Re* = 100, *We* = 100. Offset time from top: 1 µs, 3 µs, 7 µs, 11 µs, and 15 µs. The droplets are represented by iso- lines (black solid lines) of volume fraction values: 0.98 (innermost), 0.9, 0.5, and 0.1 (outermost).

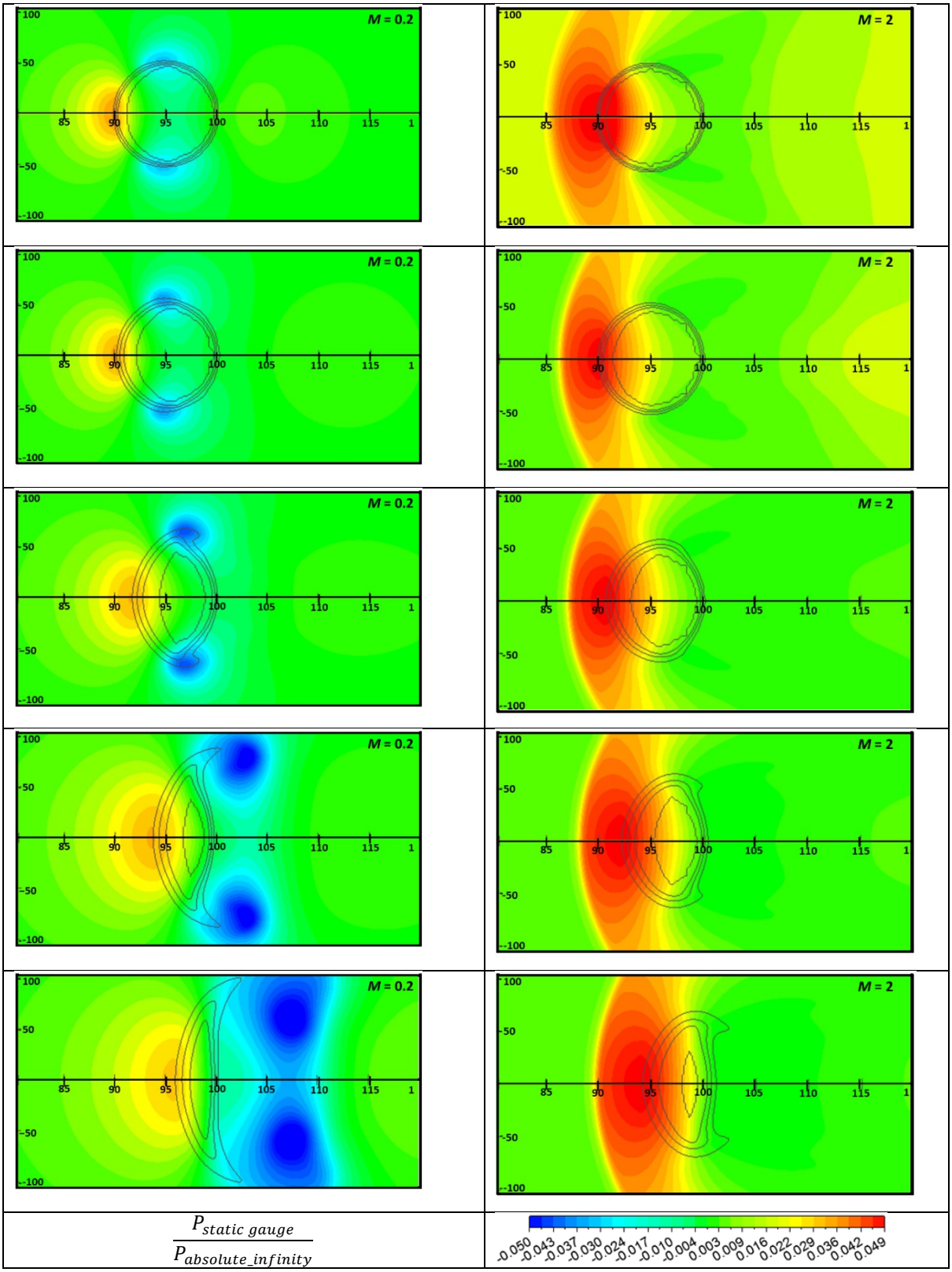

Figure 27. Comparison of normalized pressure: Subsonic (left) and Supersonic (right), displayed with the same color code. *Re* = 100, *We* = 100. Offset time from top: 1 µs, 3 µs, 7 µs, 11 µs, and 15 µs.

3.3.1.1 Deformation Driven by Pressure Gradient and Viscous Stress

In order to understand the complete stress field and the possible implications for droplet deformation, the pressure gradient and divergence of viscous stress were studied. The ANSYS CFD-post post processing software (a sister software of Fluent for post processing) only has a built-in gradient calculator without a variable divergence calculator, except for velocity. However, this CFD-post software does offer tools to construct the components of viscous stress. To test the accuracy of the method, a comparison between the $\nabla.\tau$, $\nabla.\sigma$, and ∇P was conducted. Theoretically, the resultant of $\nabla.\tau$ and ∇P should be equivalent with $\nabla.\sigma$. Figure 28 displays the agreement between that calculation and theory. Another check was to calculate τ_{xx}, τ_{yy}, τ_{xy} by a simple hand calculation, at selected points on the droplet surface, using the velocity gradient data. The result was also similar, indicating that the viscous stresses have been properly extracted from the calculated velocity field.

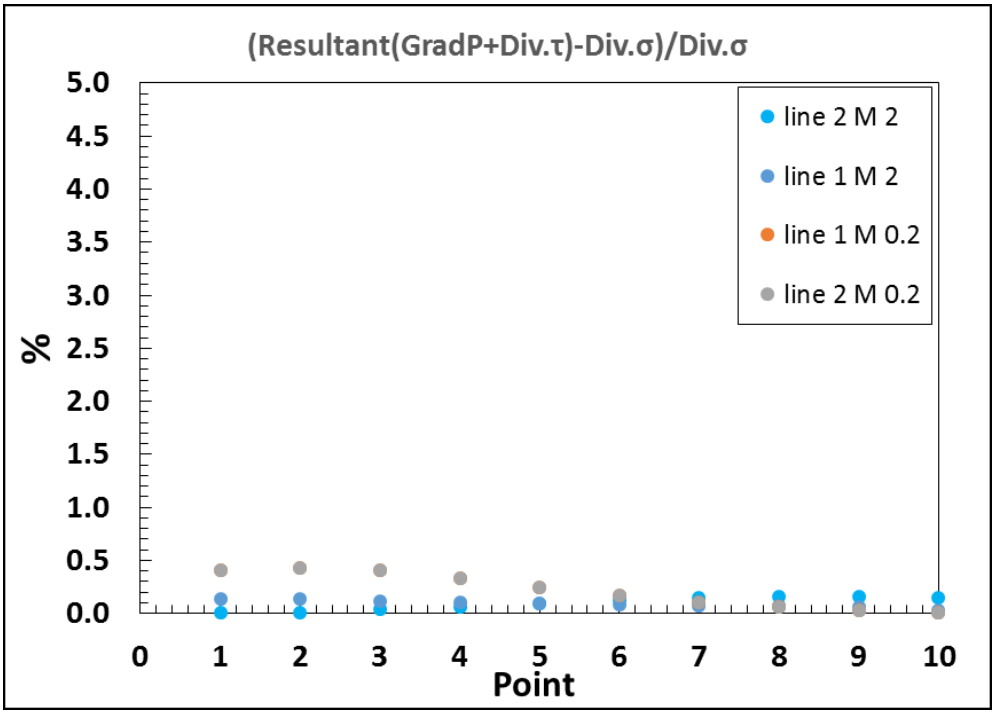

Figure 28. Checked result of the CFD-post $\nabla \cdot \tau$ built as verification of Post-Processed $\nabla \cdot \tau$

The pressure distribution (hereafter the term will refer to normalized pressure shown in Fig. 26) shows variations around the periphery of the droplet. If we compare the magnitude of pressure to the viscous

stress, the viscous stress seems to be negligible due to its magnitude averaging only about 0.1% of the absolute static pressure. However, from the equation of motion it is the gradients of pressure and the divergence of the viscous stress that drive the fluid motion, hence to determine the dominant physics acting on the droplet, gradients of pressure and divergence of viscous stress must be determined. The result is both pressure gradient (∇P) and divergence of viscous stress $\nabla \cdot \tau$ are in fact comparable in magnitude, which means both pressure and viscous stress contribute to the droplet deformation, but with pressure having the bigger role in most cases. Theofanous *et al.* also mention that shear stress will have a significant role by examining their equation which they derived [8].

Table 2. Highest value of $\nabla \cdot \tau$ /highest value of ∇P

Offset time (μs)	Subsonic	Supersonic
1	0.84	0.11
3	0.49	0.38
7	0.31	0.36
11	0.27	0.30

Table 3. $\frac{\nabla \cdot \tau}{\nabla P}$ at location of Highest $\nabla \cdot \tau$

Offset time (μs)	Subsonic	Supersonic
1	3.69	1.13
3	0.67	0.71
7	0.39	0.62
11	0.61	0.67

The initial ratio of highest-value of $\nabla \cdot \tau$ to the highest-value ∇P for subsonic flow is 0.85 while for supersonic flow it is around 0.1. These values do not necessarily exist in the same location. In the subsonic case, the highest-pressure gradient is typically near $\Theta = 80°$ for flow outside the droplet and for $\nabla \cdot \tau$ is near it. For supersonic flow, the Θ values for the peak pressure gradient and shear stress gradient are near 80° and 90°, respectively. If both $\nabla \cdot \tau$ and ∇P viscous stress are evaluated at the location of highest magnitude of $\nabla \cdot \tau$, $\frac{\nabla \cdot \tau}{\nabla P}$ is 3.7 for subsonic flow and 1.13 for the supersonic case. All these values are at early stages, with an offset time of 1 μs. It should be pointed out that there are specific locations where $\nabla \cdot \tau$ is higher

than ∇P as shown in Figs. 31, 32, 33 and 34. It should also be reminded that these locations change as time progresses. The stress-gradient ratio in the subsonic case then decrease over time. Table 2 and 3 represent values for what is considered outside the droplet. In the supersonic case, the highest-magnitude ratio of the stress gradients decreases, but the ratio at the highest $\nabla \cdot \tau$ location increases before decreasing. Viscous stress appears to play a smaller role in supersonic flow compared to subsonic flow, seen in the values of Table 2 and 3. Two trends deserve further mention here. First, the location of highest value $\nabla \cdot \tau$and ∇P may not be identical. Second, there are other locations near the droplet that has $\nabla \cdot \tau$ magnitude higher than ∇P magnitude even though it does not have the highest magnitude of $\nabla \cdot \tau$.

A mentioned above, the location where the highest values are located changes with time. In subsonic flow, the location of the peak values of $\nabla \cdot \tau$ and ∇P near the droplet surface varies. For subsonic flow, Θ then decreases to 75° for a short while. But the location of peak viscous stress then moves up again to Θ = 89° before the droplet highest point bends further back passing the leeward side. In supersonic flow, the location of highest $\nabla \cdot \tau$ magnitude shifts considerably. For short offset times in the supersonic case, the peak location of the viscous stress is located at the windward side near Θ = 90°, however there is several other locations on the windward droplet surface that exhibit peak stress values very close to the peak magnitudes of $\nabla \cdot \tau$. The peak viscous stress shifts to the windward near Θ = 45° and stay around this region as vertical elongation develops.

Figure 29 and 30 present the $\frac{\nabla \cdot \tau}{\nabla P}$ ratio at iso-line 10% droplet volume fraction. As can be seen, initially, offset time 1 μs, the shear stress play a big role on the droplet deformation. But as time progress, the divergence of tau become less dominant and the gradient of pressure become the dominant factor, in both supersonic and subsonic case. This more obvious in the supersonic case, where the ratio values are consistently below unity after offset time 1 μs. In general, both pressure and viscous stress play significant role at the beginning of the process, but then pressure becomes the dominant force as time progress.

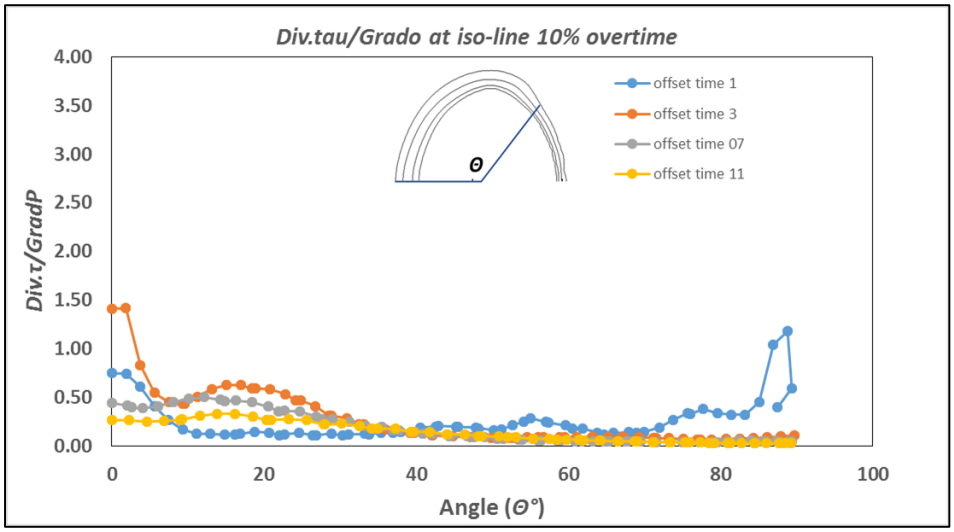

Figure 29. $\frac{\nabla \cdot \tau}{\nabla P}$ values at iso-line 10% droplet volume fraction in supersonic case for *Re* = 100 and *We* = 100

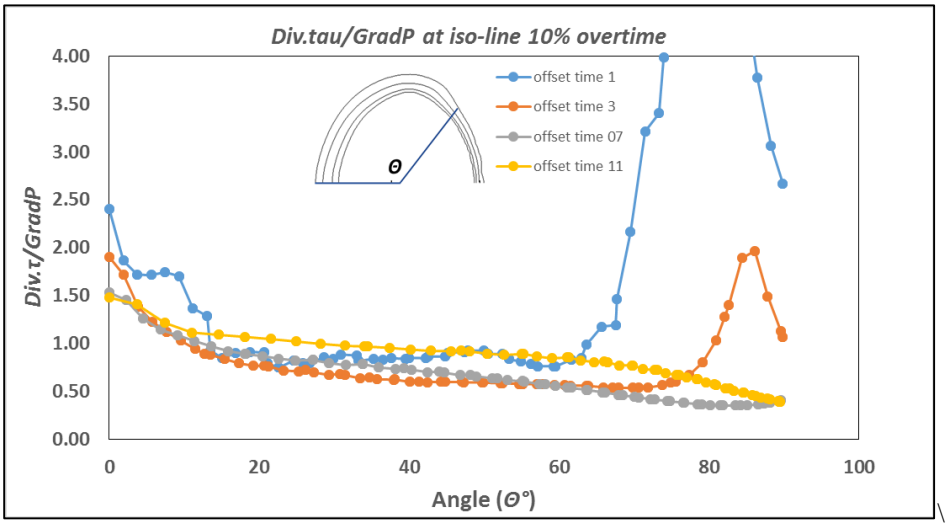

Figure 30. $\frac{\nabla \cdot \tau}{\nabla P}$ values at iso-line 10% droplet volume fraction in subsonic case for *Re* = 100 and *We* = 100

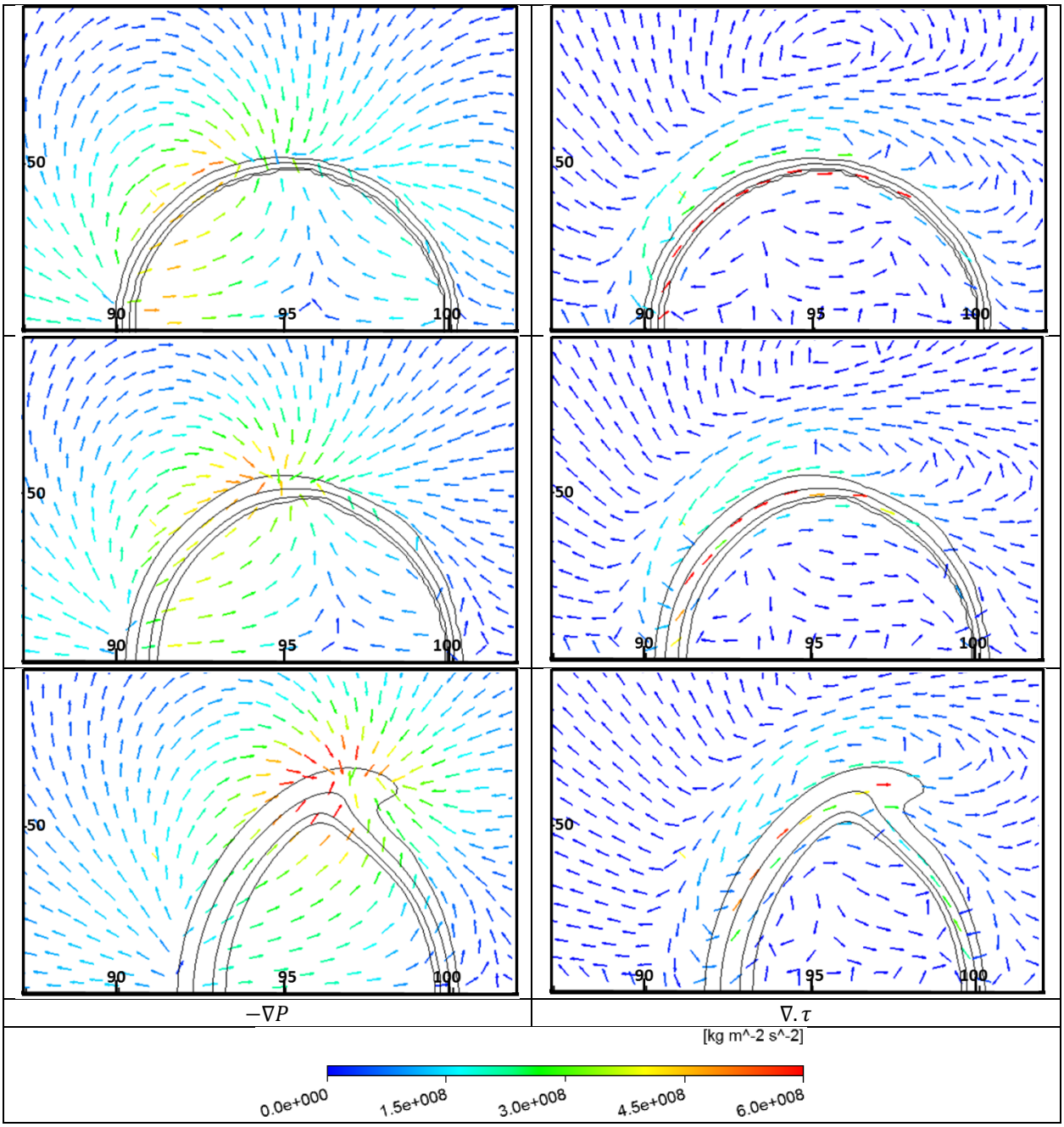

Figure 31. Vectors of $-\nabla p$ (left) and $\nabla \cdot \tau$ (right) in subsonic flow. *Re* = 100, *We* = 100. Offset time from top: 1 µs, 3 µs, and 7 µs. The droplets are represented by iso-lines (black solid lines) of volume fraction values: 0.98 (innermost), 0.9, 0.5, and 0.1 (outermost). Vector spacing: 5.5 mesh elements outside and 6.3 mesh elements inside droplet.

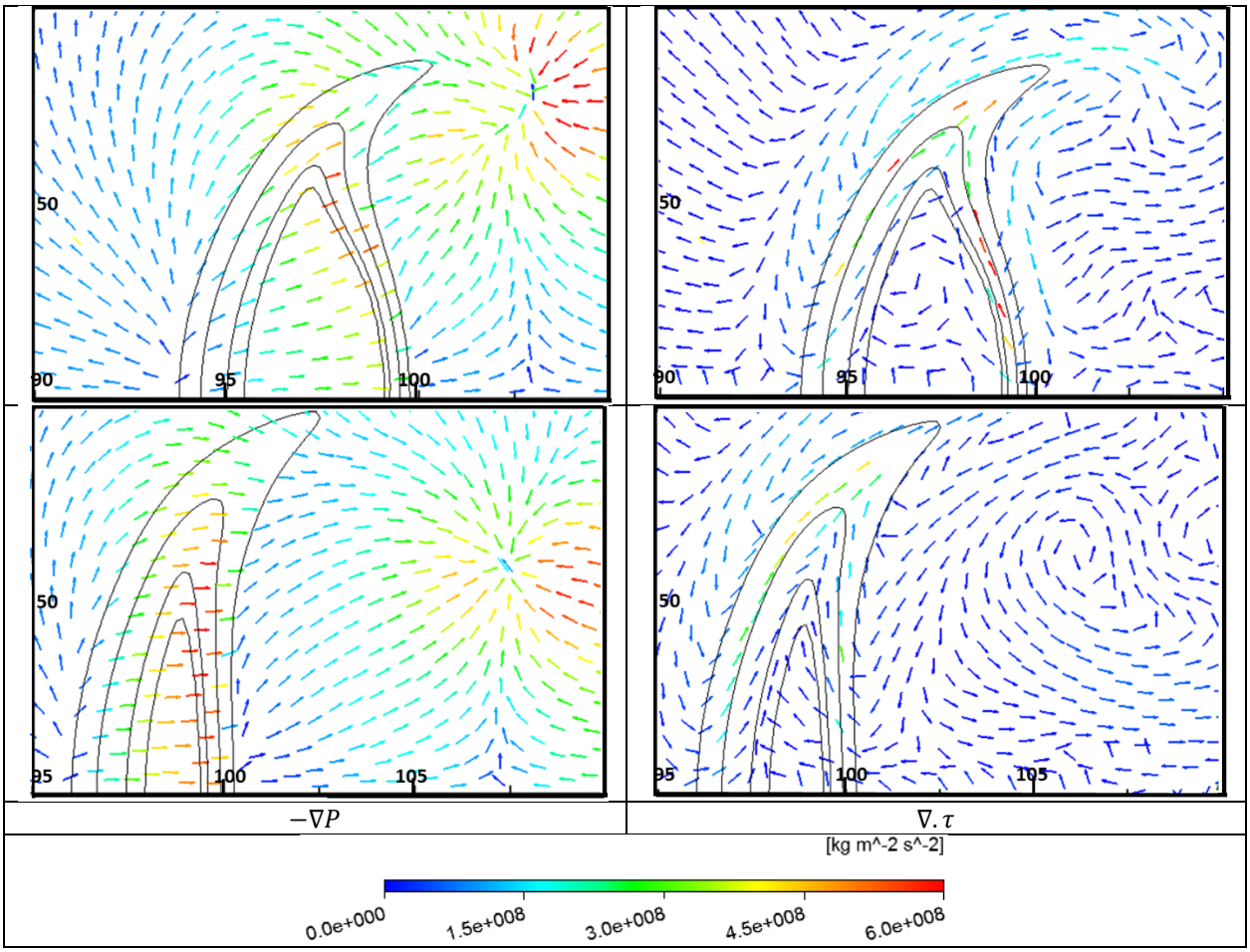

Figure 32.Vectors of -∇P(left) and $\nabla . \tau$ (right) in subsonic flow (continued). *Re* = 100, *We* = 100. Offset time from top: 11 μs, and 15 μs. The droplets surface is represented by iso-lines (black solid lines) of volume fraction values: 0.98 (innermost), 0.9, 0.5, and 0.1 (outermost). Vector spacing: 5.5 mesh elements outside and 6.3 mesh elements inside droplet.

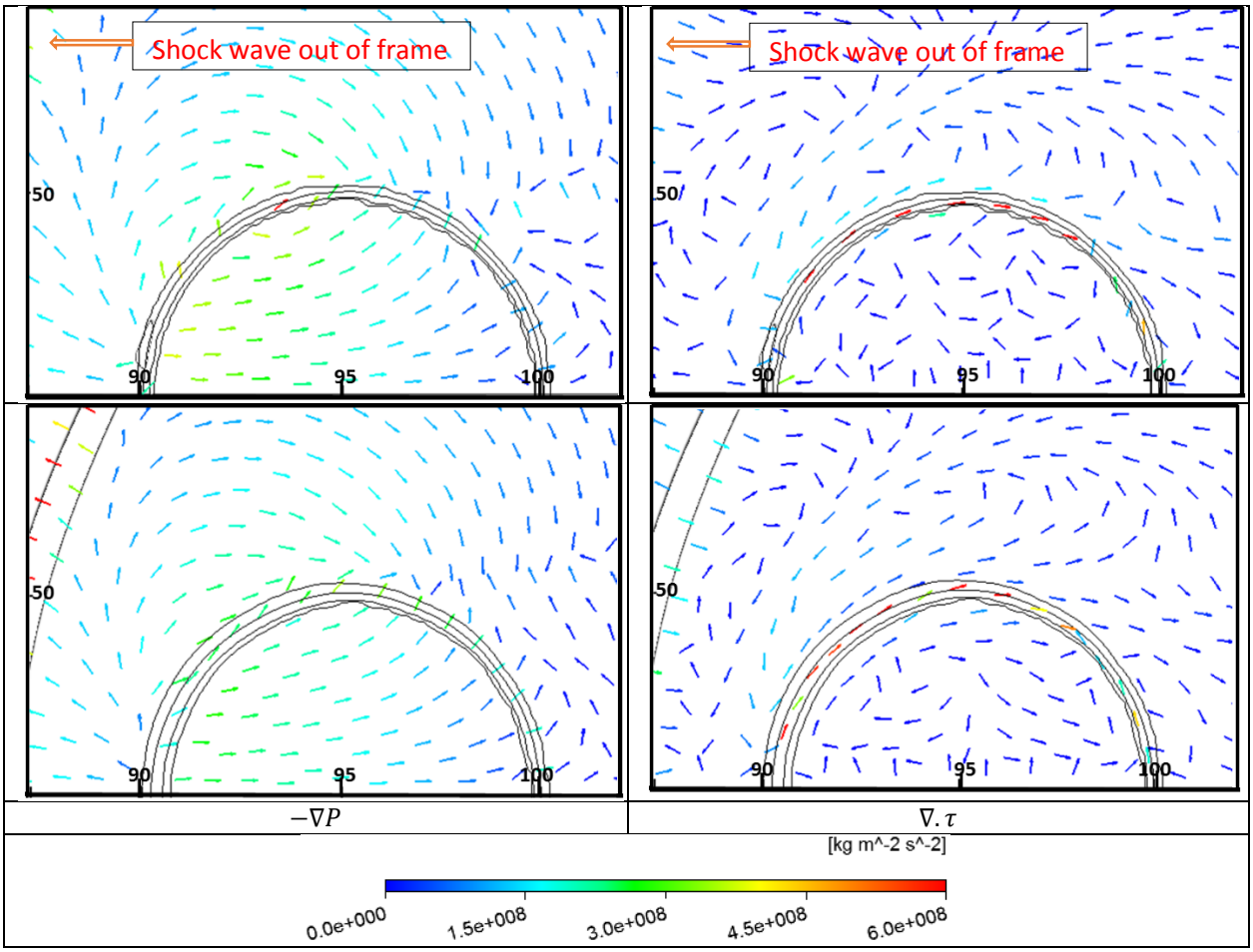

Figure 33. Vectors of -∇P (left) and $\nabla . \tau$ (right) in supersonic flow. *Re* = 100, *We* = 100. Offset time from top: 1 μs, and 3 μs. The droplets are represented by iso-lines (black solid lines) of volume fraction values: 0.98 (innermost), 0.9, 0.5, and 0.1 (outermost). Vector spacing: 5.5 mesh elements outside and 6.3 mesh elements inside droplet.

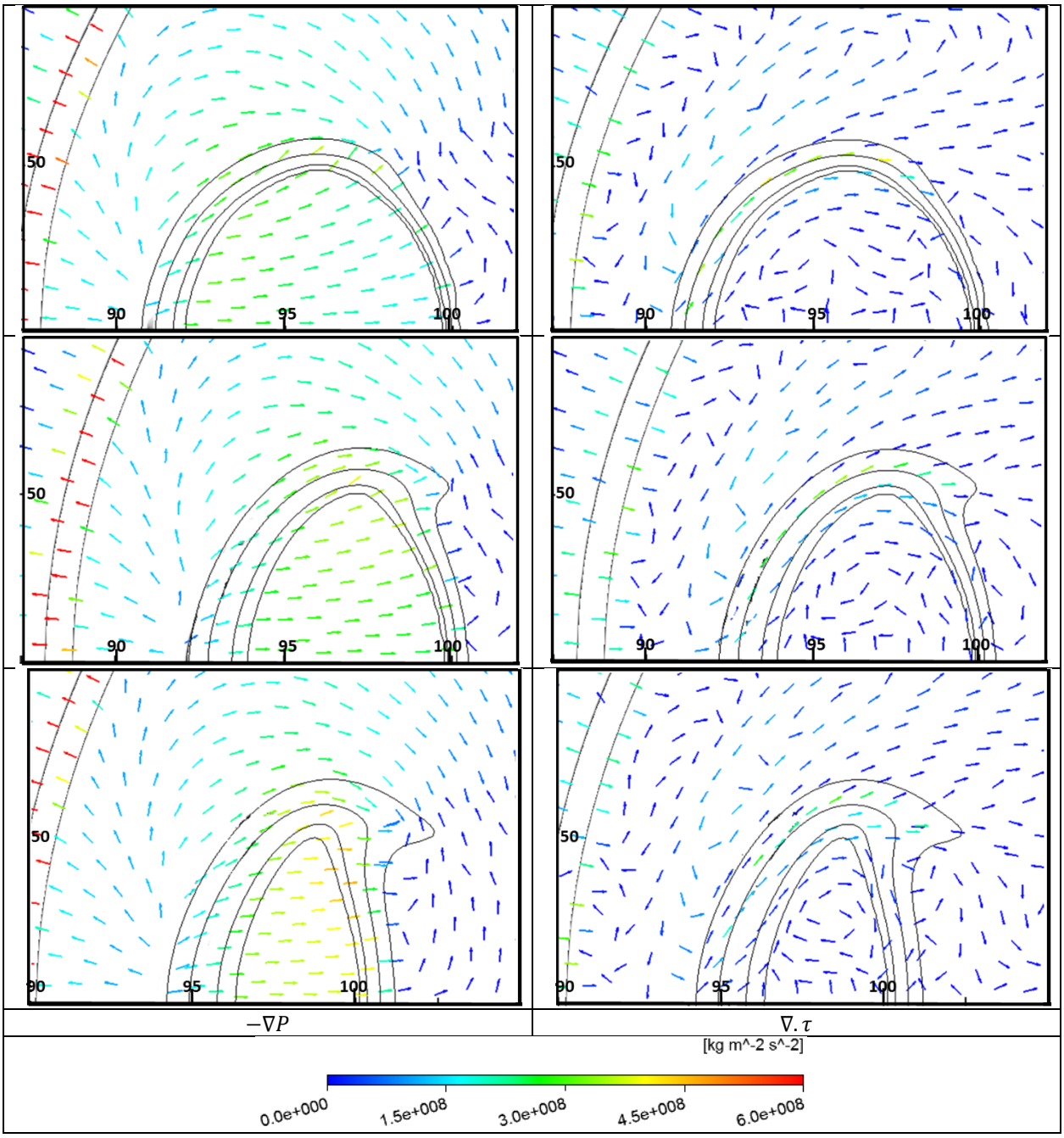

Figure 34.Vectors of -∇P (left) and $\nabla . \tau$ (right) in supersonic flow (continued). *Re* = 100, *We* = 100. Offset time from top: 11 μs, and 15 μs. Droplet are represented by iso-lines (black solid lines) of volume fraction values: 0.98 (innermost), 0.9, 0.5, and 0.1 (outermost). Vector spacing: 5.5 mesh elements outside and 6.3 mesh elements inside droplet.

The deformation process of droplets under subsonic conditions is thus driven by both pressure and viscous stress as seen in Figs 31 and 32, left image sets. The process in the perspective of these two stress variables is described as below:

1) The pressure distribution around the droplet has lowest-pressure regions at the flanks of the droplet, left image set of Figs. 26 and 27. These regions create pressure gradients both inside and outside the droplet. The pressure gradient inside pulls droplet liquid vertically towards the low pressure region. This is the main driving force behind the observed vertical stretching of the droplet.

2) Simultaneously to the above, viscous stresses also work on the droplet surface. The shear stress pushes the windward interface downstream resulting in a horizontal deformation. However due to the direction of viscous stress vector, viscous stress also has a vertical direction. This vertical component also contributes to the vertical stretching of the droplet.

3) As the viscous flow pushes the liquid interface downstream, the viscous stress assists the pressure gradient to change the droplet shape, and changes the flow field. The change in droplet shape changes the location of the lowest-pressure region. The change in lowest-pressure location region in turn changes the direction of pressure gradient. For the most part, the pressure gradients are still stretching the droplet fluid vertically. The viscous stress vector also changes direction to become more vertical, eventually leading to a droplet vertical protrusion with a backward bend.

4) The process of pressure field changes deformation, and the deformation changes the flow field continues throughout the process. At later on, offset time 11 μs, the leeward side of the droplet also sees viscous stress from the growing recirculation region. The action of both droplet side viscous stress helps shape the droplet to a thin lenticular shape. At this point the lowest-pressure region has already been located off the droplet and the pressure gradient inside the droplet has become aligned with the flow direction, which is directed

more horizontal than vertical at the edges of the deforming droplet. The droplet then proceeds throughout rest of the breakup process in this shape seen in last image of Fig 32.

5) To bring the point once more, the forces working on the deformation is stated again. The forces that dominates the deformation changes as time progress. In the initial stage, offset 1 μs, both the pressure gradient and divergence of viscous stress is significant in driving the deformation, with viscous stress divergence is more dominant. But as time progress the, pressure gradient is the dominant factor.

In supersonic cases, the droplet deforms in a thicker and shorter lenticular shape compared to the thin and long lenticular shape seen in the subsonic cases. This deformation evidently occurs because there is no strong vertical pulling in supersonic cases, Fig. 33. The process is described as below and can be compared to the deformation process under subsonic conditions, Thus for the case of supersonic flow:

1) The right images set of Figs. 26 and 27 indicate that there is apparently no distinct, lowest pressure region at the flanks of the droplet. Hence, the pressure gradient inside of the droplet pulls droplet fluid downstream with only slanted slightly in vertical direction. The pressure gradient also causes the windward interface to be pulled back, altering its curvature.

2) Given the small pressure gradient effect, the initial magnitude of divergence of viscous stress acts as the main factor pushing the windward interface backward and changing its curvature. Due to its direction, it also pushes the windward interface outwards from the flow centerline, stretching the droplet vertically. But after 1 μs, pressure gradient is the dominant factor of the deformation.

3) The change in curvature does not bring about drastic changes in the air flow direction, hence the lowest-pressure region remains mostly at the leeward side of the supersonic cases. There is no the lowest-pressure region at the flanks of the droplet seen in subsonic flow. The droplet deforms and this deformation does however change the flow field which shifts the lowest-pressure region just within the droplet leeward side. As the lowest-pressure region moves down it also expand in area while the associated value of the pressures.

This affects the pressure gradient inside the droplet to become more horizontal. This further contributes to the lack of vertical force that can elongate the droplet vertically.

4) As time progresses, the magnitude of the viscous stress divergence decreases and the pressure gradient becomes the main factors that drives the droplet deformation. At this time, starting around offset time of approximately 7 μs, the pressure direction is stronger in the horizontal direction than in vertical direction. The pressure gradient works almost horizontal at the droplet peak, as seen in Fig. 34, which in time creates the horizontal protrusion at the droplet peaks.

5) Due to the horizontal pressure gradient at the droplet peak, the horizontal pressure gradient inside the droplet, and the lack of force to stretch the droplet vertically, the droplet assumes this thicker and shorter lenticular shape throughout the rest of its lifetime than is seen in incompressible flow.

There is a general process that is apparent in both the supersonic subsonic cases, that the pressure field first affects the pressure gradient and divergence of viscous stress, albeit the magnitudes are different. The pressure gradient and divergence of viscous stress, even if divergence of viscous stress plays a somewhat smaller role in some cases, drives the deformation. The deformation then changes in the flow field. A comparison with the flow over solid sphere shows that no significant changes in the flow filed occur if there is no deformation, as can be expected and will be discussed later on. Figure 35 shows a simple schematic that describes this process

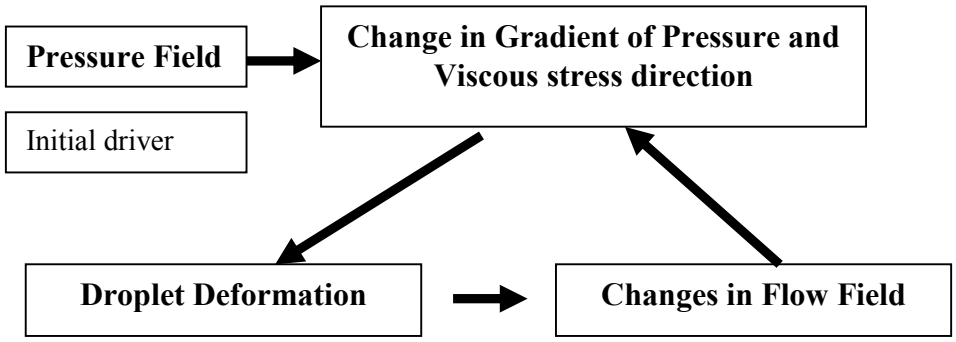

Figure 35. Schematic of the deformation process

The simulations were all conducted at low Reynolds number which was much lower than Reynolds number in most experiments. The flow towards the windward side of the droplet can be reasonably expected to be similar to that for higher Reynolds number flows, at least in terms of the flow and pressure fields. As shown previously, the initial pressure distribution inside the droplet is similar to that reported by Theofanous *et al.* [6], albeit they have higher Reynolds and Weber numbers. This builds confidence that this distribution is expected. However, since higher *Re* will lead to important flow differences in the wake region, the behavior of the lowest-pressure region in supersonic flow can be different.

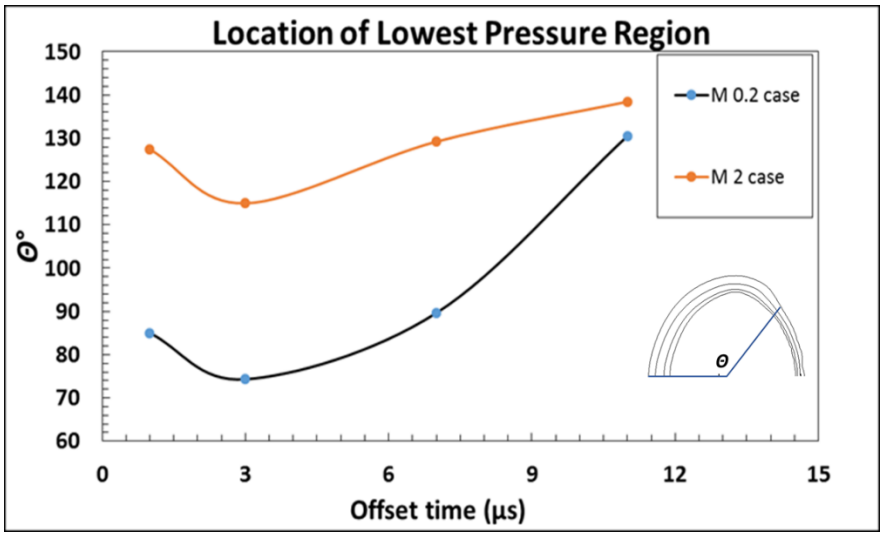

Figure 36. Lowest-pressure region location for *Re* = 100 and *We* = 100

In both the supersonic and subsonic flow cases, the highest pressure region is located at the droplet windward stagnation point. Because of this, the different lowest-pressure region location is the main factor determining the direction of the pressure gradient inside the droplet at early stages, such as at an offset time of 1 μs. As presented in Fig 36, the lowest-pressure region location in the initial stages is different, in the supersonic cased the low pressure occurs at the droplet leeward side, in the subsonic case, the low pressure region is near the droplet peaks.

The subsonic case's lowest-pressure region remains relatively constant in location on top of the droplet and then migrates away and downstream from the droplet, as discussed above. The location of

minimum surface pressure is located near Θ = 90° from the droplet forward stagnation point early on, relatively stays there when the droplet is still spherical in shape, and migrates to Θ > 132° after droplet develops the vertical protrusion, seen in Fig. 26 fourth image of the left set and in Fig 36. This matches the pressure gradient direction that is mainly towards the droplet peak for offset times of 1-7 μs. The supersonic cases have the lowest-pressure region on the leeward surface of the droplet, beginning at Θ = 127° and shifting to Θ = 115° for a short time and then returning to the initial value. This apparent upward movement is attributed to the droplet vertical elongation. The center of lowest-pressure then slowly moves towards the droplet center line as lenticular shape becomes visually obvious, seen in Figs 26 fourth and fifth image of the left set and Fig 36. The Θ angles were calculated from the middle point of droplet horizontal center line to the center of the lowest-pressure region area, as determined by the mid-point of iso-line 10% droplet volume fraction along the horizontal flow centerline.

3.3.2 Droplet Deformation Mechanisms from a Recirculation Point of View

Supersonic and subsonic flow present differences in the air flow recirculation behavior in the leeward region of the droplet. A solid sphere in a *Re* = 100 flow theoretically experiences laminar stationary recirculation at its leeward side, which both supersonic and subsonic cases exhibit this characteristic to a certain extent, consistent with the Reynold number of 100 employed in this study. In the early stages (offset time 1-7 μs) of the simulations both air flows have recirculation regions that remain in an almost constant horizontal position relative from the droplet in the early stages, hence the recirculation can be considered stationary. The recirculation region in subsonic flow will be accompanied by viscous stresses that may be sufficiently large to contribute to the leeward side deformation after an offset time of roughly 11 μs. As the droplet deformation process proceeds, these recirculation zones behave noticeably different. Figures 37 and 38 visualize these differences, presented in a style similar to that employed by Meng & Colonius [16].

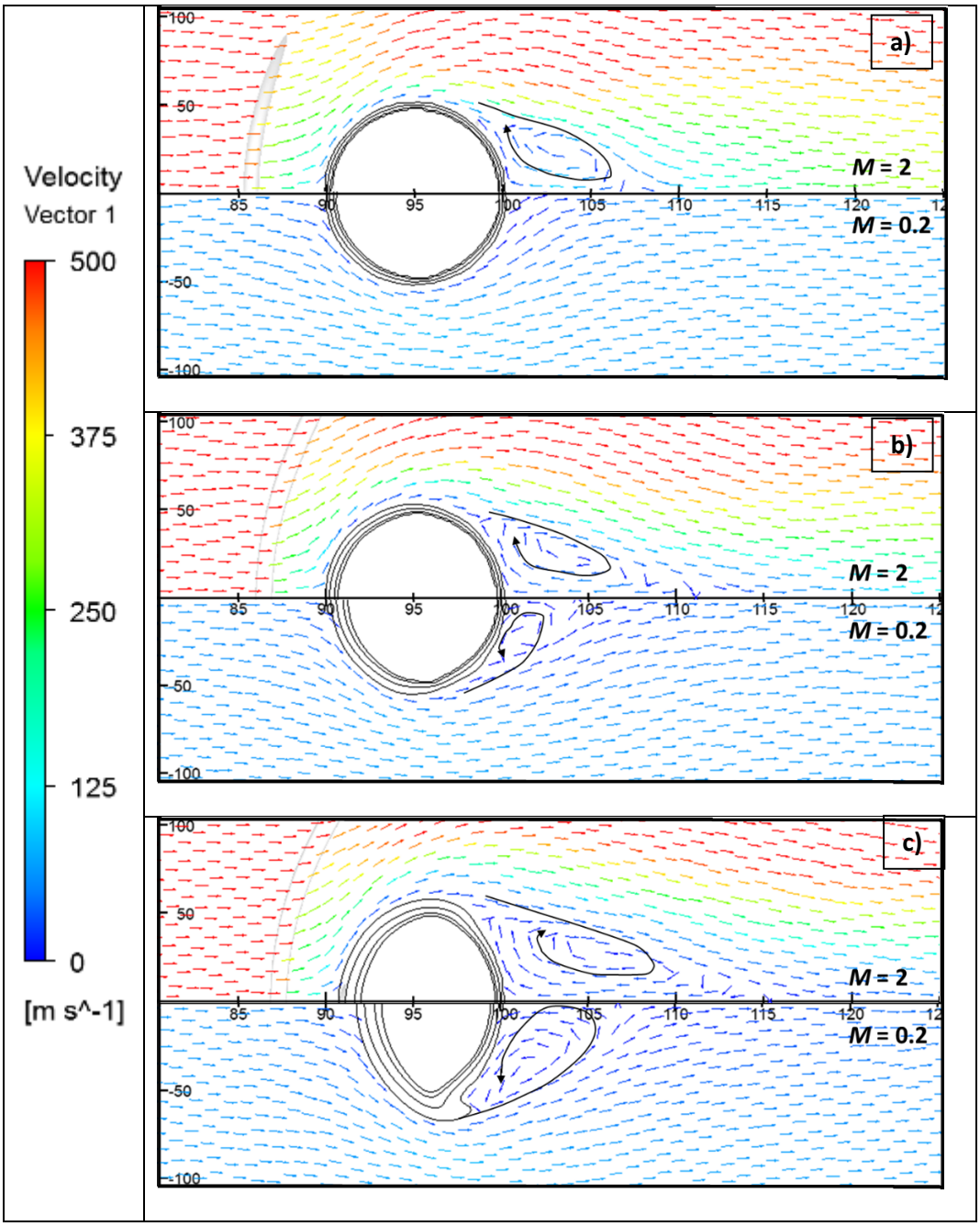

Figure 37. Supersonic (upper) flow and Subsonic (lower) flow velocity vectors evolution. *Re* = 100, *We* = 100. Offset time: a) 1 µs, b) 3 µs, c) 7 µs. The droplets is represented by iso-lines volume fraction values: 0.98 (innermost), 0.9, 0.5, and 0.1 (outermost). The general movement of the recirculation regions are shown to aid recirculation center visualization

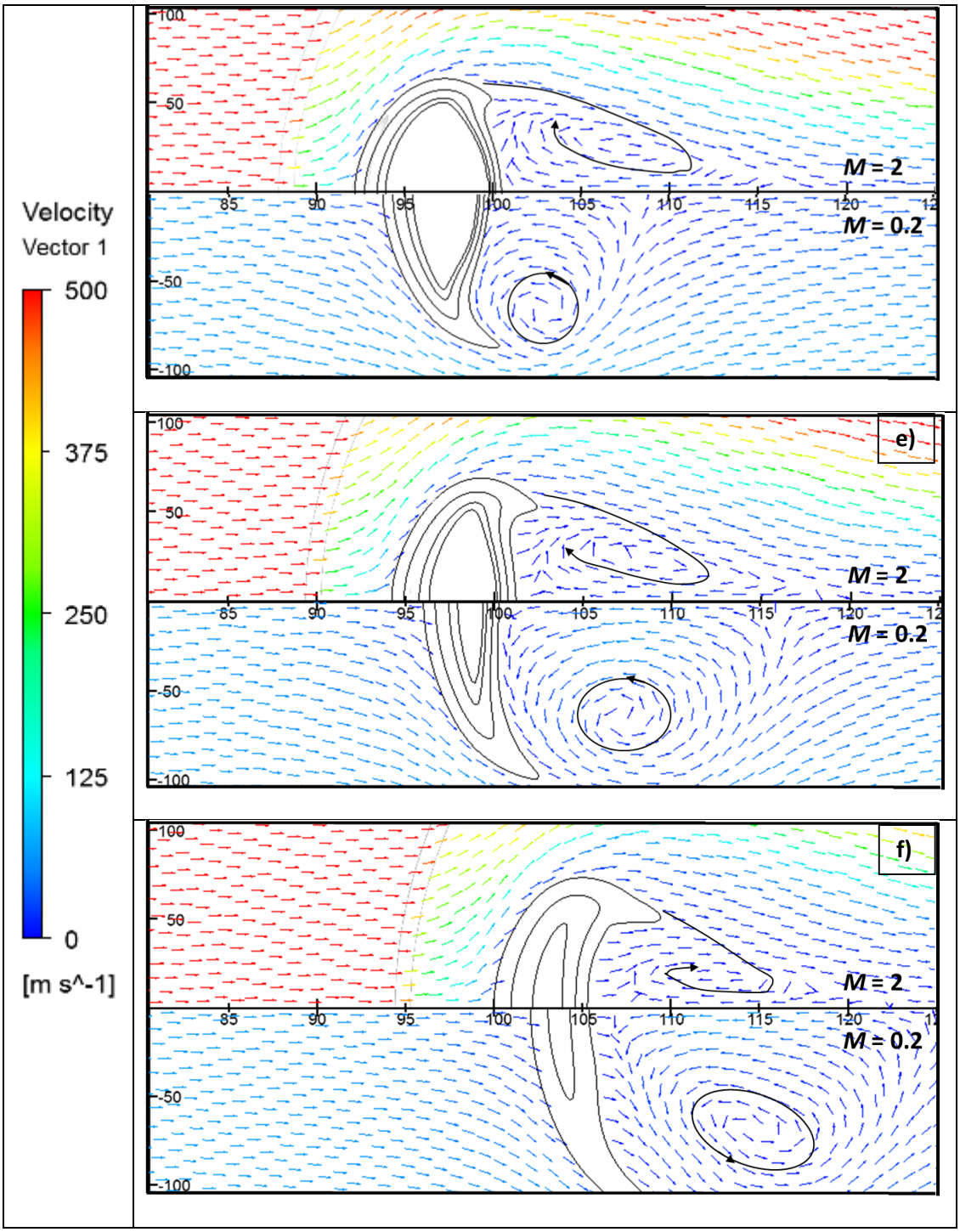

Figure 38.Supersonic (upper) flow and Subsonic (lower) flow velocity vectors evolution. *Re* = 100, *We* =100. Offset time: d) 11 µs, e) 15 µs, and f) 23 µs. The droplet surface is represented by black iso-lines volume fraction values: 0.98 (innermost), 0.9, 0.5, and 0.1 (outermost). The general movement of the recirculation regions are shown to aid recirculation center visualization

The experiments by Boiko & Poplavski on a deformed droplet model presented recirculation regions, both at the leeward side but one region is near the top of droplet model surface while another isolated vortex assumes a position closer to the droplet horizontal centerline [9]. In the current study, the subsonic region eventually assumes a position near the droplet outer edge with a rounder recirculation shape. In supersonic flow, the recirculation region assumes a position more similar to an isolated toroidal vortex than is the case in subsonic flow for short offset times, on the order of 1 micro second, as can be seen on Fig 37.

The main difference in recirculation between the two cases may be the shape of the recirculation zones. In supersonic flow, the high velocity allows flow to travels much further back before portions of the flow recirculates to the droplet. This causes the flow to have a somewhat ellipsoidal trajectory with a small upward portion and have a center that is nearer to the droplet center line compared to the subsonic case. The recirculation zone stays in a relatively constant position to the droplet as time increases in the supersonic case. While in subsonic flow, the recirculation starts at a later time than for the supersonic case. The vortex grows from a small recirculation at the leeward side and located near the droplet center line. From this point, the recirculation region grows larger with a slight vertical elongation. At a time, around 11 μs, the vortex will start to move vertically and become more circular which happens around the time the droplet became visually ellipsoidal. The simulation is axisymmetric, and at Re = 100, the flow is expected to have an axisymmetric recirculation, which then assumes a position higher than the location of supersonic. Instead of dying out, subsonic recirculation moves away.

It should be pointed out that flow across a real liquid surface inevitably leads to an accompanying shear stress. This is because there will be velocity gradients, regardless of the magnitude, due to the no-slip condition at the liquid surface. The velocity gradient is the source of the viscous stress.

Both the pressure and the viscous stress deforms the windward droplet surface, both pushing the surface back and vertically elongating it, while air flow starts to follow the droplet contour. This pushing

of the windward interface changes its curvature which alters, in turn, the flow field. Eventually this deformation causes recirculation to appear. As mentioned in the discussion about divergence of the shear stress tensor, the viscous stress in the leeward side is generally lower than that on the windward side. This is because the velocity at the leeward side is much smaller than on the windward side of the droplet. The unbalanced stress field contributes to the backward deformation of the droplet peaks.

3.3.2.1 Solid Sphere Comparison

In order to better understand the impact of compressibility on the flow field and the implications for droplet deformation, simulations were also performed for the flow over rigid spheres. Two simulations of axisymmetric solid-wall spheres were conducted. The flow conditions were similar to Re = 100, We = 100, M = 2 and M = 0.2 to emulate both supersonic and subsonic conditions.

The result of the two solid sphere cases, in terms of pressure distribution, shows that there are significant differences between the two cases. The solid-sphere pressure distributions are shown in Fig. 40 and the corresponding location of the lowest-pressure region in Fig. 39. The most notable part is the lowest-pressure region, which for the subsonic case it is located near and slightly downstream of the droplet peak. For the case of supersonic flow, the location of the minimum pressure is shifter towards is at the leeward side of the sphere. The lowest-pressure region for the subsonic case stays relatively fixed but the pressure value increases with time. This is also the true for supersonic flow, but only after the lowest-pressure regions reach a fixed position. The supersonic solid-sphere case reaches this constant fixed position at around offset time 7 μs.

A comparison between Figs. 26 and 40 shows that both the deforming droplet and the solid sphere have similar distributions of static pressure for both the subsonic and supersonic cases, respectively, for sufficient short offset times of 1-3 μs. After an offset time greater than approximately 7 μs, the pressure field between the droplet and solid sphere cases differs in two ways. First, the lowest-pressure region moves as the deformation in the droplet increases, while the pressure distribution for the solid sphere remains

relatively invariant, as expected. Second, the evolution of the lowest-pressure magnitude between the droplet and the solid sphere cases is different, with a decrease seen in droplet cases and an increase in the solid sphere case. The deforming droplet case has the magnitude of the pressure in the lowest-pressure region that is decreasing, as indicated by the deeper blue color code in Fig. 26. By comparison, the solid-sphere case exhibits an increase in the pressure value in the lowest-pressure region as time progress, as indicated by the lighter blue color code moving to green color code in Fig 40.

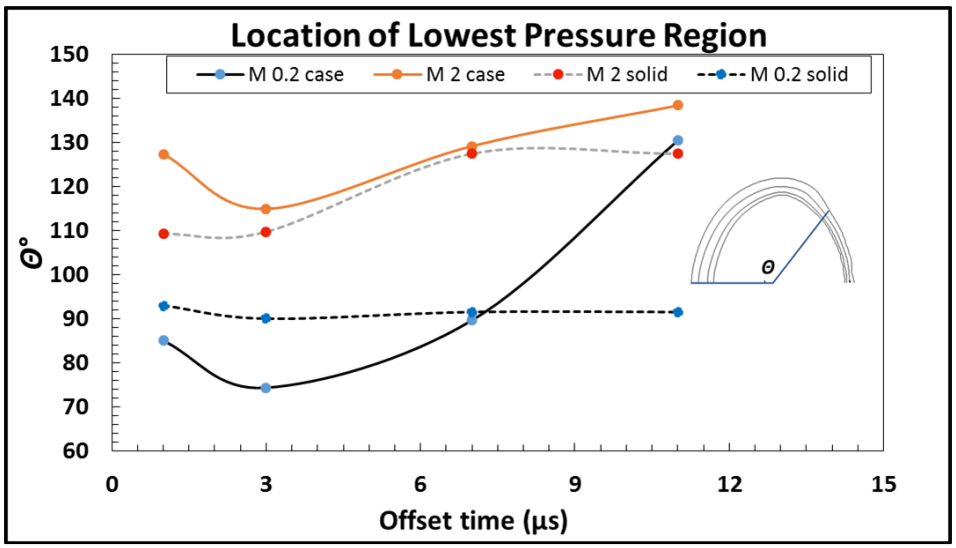

Figure 39. Comparison of lowest-pressure region location between droplet and solid sphere for *Re* = 100 and *We* = 100

These two differences in pressure distributions for the droplet and solid sphere subsonic case is also present in the respective supersonic case. But it is clear that the change in lowest-pressure region magnitude is less apparent in the supersonic cases. This fact suggests that deformation does affect the flow fields. In the subsonic droplet case, the deformation is higher hence the difference in flow field changes is more obvious.

The above discussion has established that the early stages of solid sphere and droplet are similar, especially in pressure distribution. Thus the reason of the initial pressure distribution difference between supersonic and subsonic flow can be taken from the solid sphere perspective at offset time 1 μs.

Determining the cause of the different pressure distribution is important. As mentioned before, pressure gradient direction is determined by the location of high and low pressure region. Because the high pressure region is located at the stagnation point for both subsonic and supersonic case, then the importance of lowest-pressure region location is clear.

Locations of the lowest-pressure region in subsonic flow that are shown by Fig. 29 are confirmed by looking the studies by Rimon & Cheng [23] and Constantinescu & Squires [24]. Each of these studies is in subsonic flow and they are are different Reynold numbers but all of them have the lowest-pressure region occurring near the sphere peak.

For supersonic flow, the same lowest-pressure region at the leeward side is also seen by Theofanous *et al.*, both in their cylinder and spherical droplet [6]. Classical studies on a sphere such as Lam & Pollock shows that in compressible flow, the Mach number has the effect of shifting the peak pressure location (lowest-pressure region location.) [25]. Their experiment shows that as the Mach number is increased, the lowest-pressure region shifts downstream. The experiment was conducted on the range of $0.4 < M < 1$, but the effect is expected to continue. The exact location of the lowest pressure region will depend on the Reynolds number due to flow separation effects. Even though their Reynolds numbers were for much higher values than those of the current study, Theofanous *et al's* result mentioned above, which has Re = 300-3300 and $M = 3$, brings confidence that the result of this study is aligned with this trend of the shift in the location of minimum pressure to locations further downstream as the Mach number is increased. This fact also strengthens the observed trend that compressibility has a role in the difference of vertical elongation between the supersonic and subsonic case, which is by shifting the lowest-pressure region location.

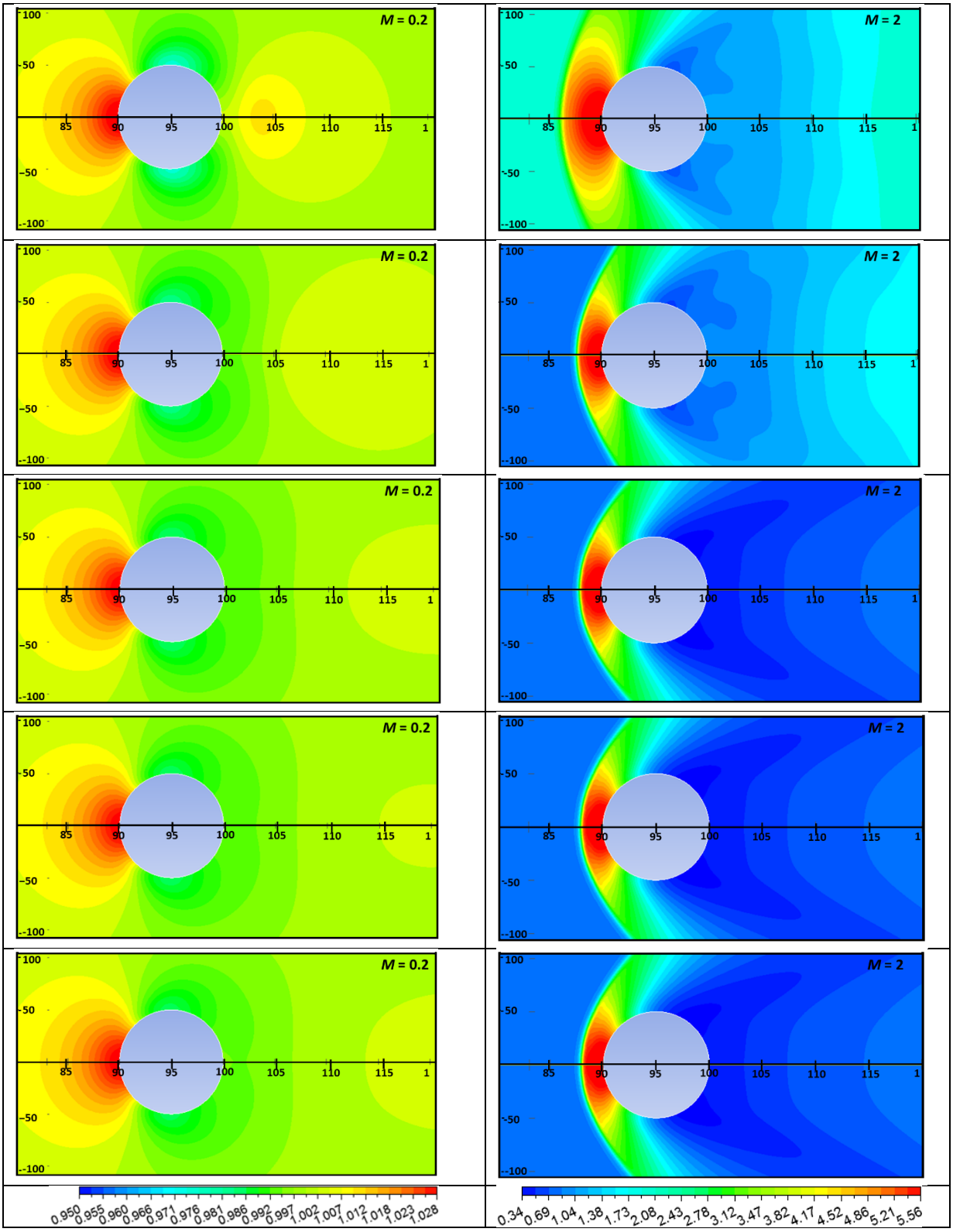

Figure 40. Solid Sphere normalized pressure *(P(static gauge)/P(absolute_infinity)):* Subsonic (left) case and Supersonic (right) case. *Re* = 100, *We* = 100. Offset time form top: 1 µs, 3 µs, 7 µs, 11 µs, and 15 µs.

In terms of viscous stress and its divergence, the value between solid sphere and droplet is expected to be different. This is due to the different boundary object conditions between the two cases. A solid sphere has a boundary condition of solid non-deformable wall: the droplet has a fluid-fluid boundary condition that is deformable. The deformable boundary condition can have movement/velocity that results in lower viscous stressed compared to the case of a solid wall.

In the recirculation point of view, the end condition of the recirculation region between the solid sphere subsonic and supersonic cases seems to be similar, by visually observing the last two image of Fig. 42, but the process of reaching these end states is noticeably different. The supersonic case starts with the recirculation region already horizontally elongated. The horizontal length of the recirculation changes as time progress, first increasing then decreasing. Over time, this recirculation region then move slightly towards the droplet center and obtain a short horizontal length.

The flow recirculation for subsonic case on the other hand starts by following the solid droplet contour, then a small recirculation region emerges near the droplet horizontal centerline. This recirculation region grows to a near circular shape with some vertical elongation. The recirculation region also moves slightly towards the droplet top edge. At the end, even though supersonic and subsonic recirculation regions look similar, a closer inspection reveals that supersonic recirculation is more horizontally elongated while subsonic recirculation region is more circular with some vertical elongation. These are similar to the recirculation patterns seen for the case of deforming droplets.

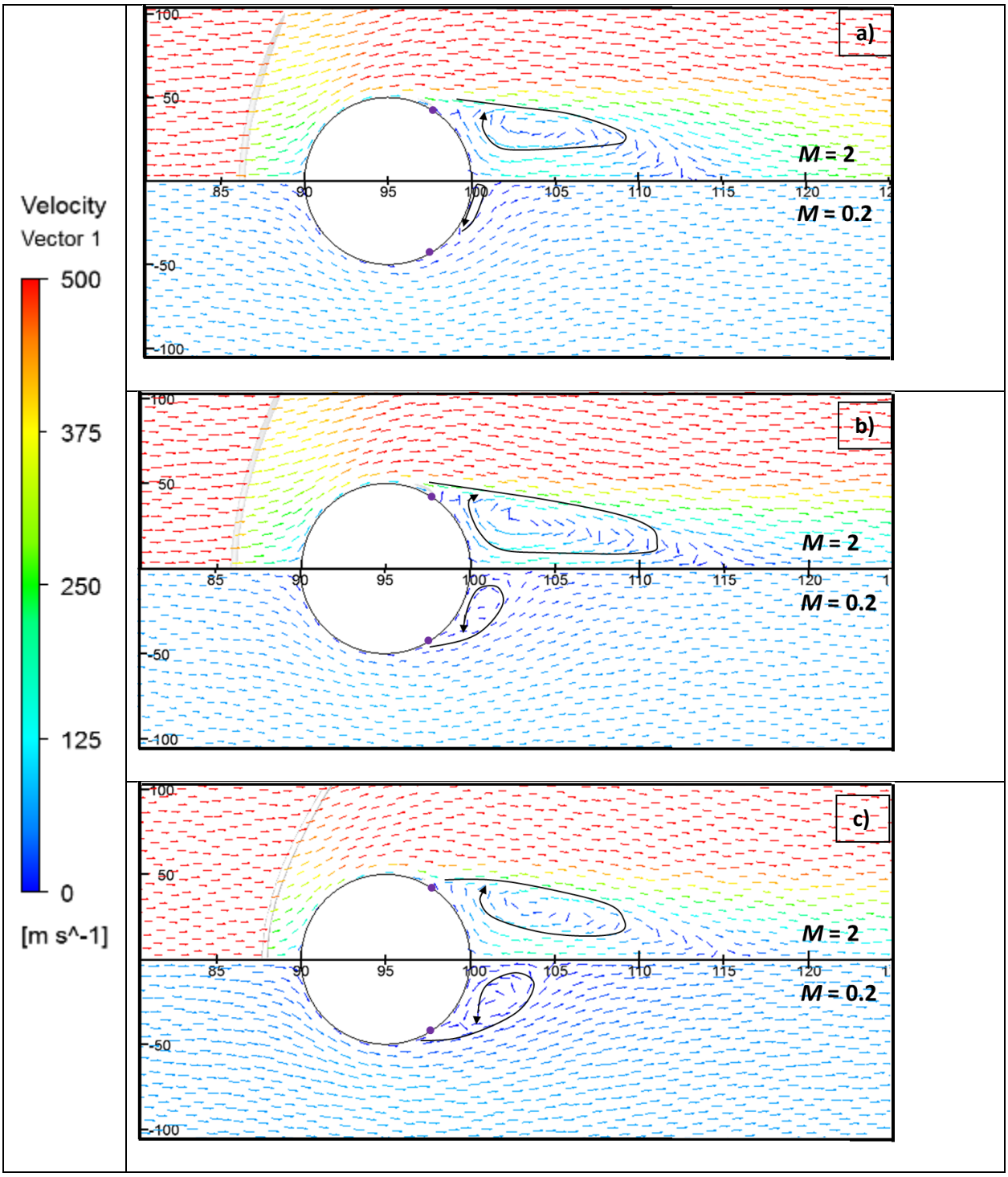

Figure 41. Solid droplet sphere (axisymmetric) supersonic (upper) flow and subsonic (lower) flow velocity vectors evolution. *Re* = 100, *We* =100. Offset time: a) 1 µs, b) 2 µs, c) 3 µs. The general movement of the recirculation regions are shown to aid recirculation center visualization

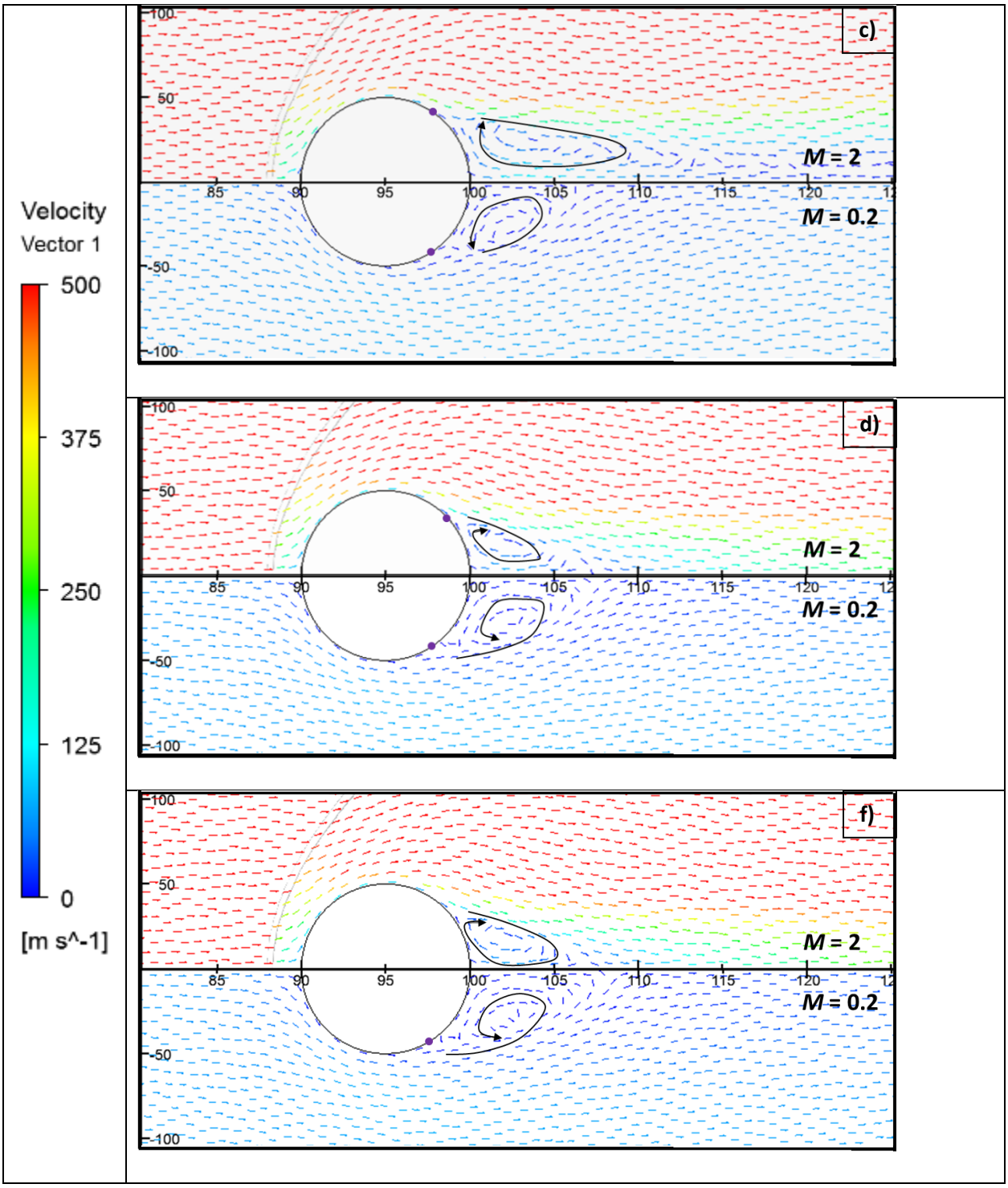

Figure 42. Solid sphere (axisymmetric) supersonic (upper) flow and subsonic (lower) flow velocity vectors evolution. *Re* = 100, *We* = 100. Offset time: c) 5 µs, d) 7 µs, f) 11 µs. The general movement of the recirculation regions are shown to aid recirculation center visualization

The early stages of these solid-sphere recirculation patterns have similar trends to the early stages of the deforming droplet case. Both in the solid and deformable droplet, supersonic-flow recirculation is horizontally elongated and the subsonic case is more circular. These similar trends in the early stages help build confidence that the recirculation behavior we see at the deforming droplet is expected at this $Re = 100$.

A more detailed comparison with the subsonic case reveals a recirculation region for the case of the solid sphere that grows rounder and moves vertically before stopping at a certain distance from the centerline while in deformable droplet the recirculation moves to a notably higher position. In the supersonic cases, both solid and deformable droplet recirculation region stays in a relatively fixed position relative to the droplet, near the centerline and a bit further downstream. This also suggests that there is a connection between the droplet interfacial deformation and the position of the recirculation region, such was discovered when studying the pressure distribution. The most possible connection is the large vertical deformation of the droplet interface in subsonic case, results in a shift in the location of the recirculation zone, while the low interfacial vertical deformation in supersonic flow keeps the recirculation relatively more stationary to the droplet. It results in the two flow regions having different pressure distributions, especially in the location of the low-pressure regions. This in turn affects the deformation. Thus the connection effect between variables is reinforced.

3.4 The Impact of the Two Operating Condition Types and Reynolds Number on the Results.

As mentioned in chapter 2, Table 1, in order to keep a constant Reynolds and Weber number for both the subsonic and supersonic cases, two distinctly different operating conditions had to be applied, one for supersonic case and the other is for subsonic case. The supersonic case is characterized by low density, low viscosity, and a low operating pressure condition while the subsonic case is has correspondingly higher values of density, viscosity, and operating pressure. The main drivers of the deformation are pressure distribution (hence its gradients) and viscous forces. The impact these two variables will be briefly discussed within the context of the very different operating conditions.

Previous subchapters established that the difference in pressure distribution, therefore pressure gradient behavior, is the main cause of subsonic high vertical elongation. Confidence in the different pressure distributions was firstly built by knowing that Theofanous *et al.* also reported a similar trend in pressure distribution inside the droplet for their subsonic and supersonic cases [6]. This is important because the pressure distribution drives the droplet fluid mostly vertically, for the cases where there is such motion. Also observing the pressure value distributions after being normalized by their respective upstream pressures, allows for plotting the pressures in both subsonic and supersonic flow on similar scales. Specifically, while the gauge-pressure values themselves are very different for the two flow cases, the normalized pressure can be put on a reasonable scale, as seen in Fig. 27. In this case it can be noted that the normalized freestream pressure is almost the same between the two cases.

The second deformation driver is the viscous flow, though as discussed previously, these forces are, in many cases, smaller than those resulting from the gradients in pressure. Here the concern lies in the strain rate, which is the result of velocity gradient which leads to the shear stress. The supersonic-flow case will tend to have higher velocities than the subsonic case, even after the shock wave. This can in turn lead to create a higher strain rate. But due to the intention of keeping the Reynolds and Weber numbers the same, the dynamic viscosity was also altered at freestream, with supersonic using lower value of the dynamic viscosity, as seen in Table 1. This leads to the subsonic case having a lower maximum magnitude of $\nabla \cdot \tau$. However, the effect on the strain rate is less clear compared to the effect on pressure.

As a reminder, the current study simulations' are at low Reynolds number, Re = 100, while Reynolds number in experiments are typically at much higher values. As is well-known, the wake region will clearly be very different for the different Reynolds number regimes. The shear stresses and boundary layer behavior would also be Reynolds number dependent. But the physics on the windward face of the droplet are less sensitive to the Reynolds number, so that the pressure field responsible for the initial droplet deformation is predicted not to be very dependent on the Reynolds number. However, the effects of

increasing the Reynolds number and the emergence of turbulent flow in the droplet wake are interesting and important topics to be investigated in future works.

Chapter 4 Summary

1. A mesh with 4 four interfaced subdomain that provides high-density mesh for representing the droplet and enough space for the bow shock length was successfully developed and run using the commercial software package Fluent for deformable droplets and solid spheres in subsonic and supersonic flow. The method was able to optimize total mesh size.
2. Validation of Fluent and first order upwind calculation was conducted by comparison to a helium-air shock tube to check agreement with the exact, 1D shock tube relations for inviscid flow. The simulations were also seen to reproduce the droplet shape and displacement reported experimentally by Engel and the features of droplet-shock interaction presented by Boger *et al*.
3. Fixed values of Reynolds number (Re=100) and Weber number (We = 50, 100, and 200) were achieved by having combinations of flow properties for the two types of operating conditions (subsonic and supersonic) and an air flow with a modified dynamic viscosity.
4. The supersonic freestream flow does not change the main droplet breakup mode for the values of Weber number considered here, which remains a stripping-type breakup. Supersonic flow does affect the droplet deformation and lifetime within the main (stripping) breakup mode at laminar Reynolds numbers, compared to subsonic flow.
5. Supersonic flow effects on droplet deformation and disruption include a thickening of deformed droplet shape, reduced droplet deformation (L_y/L_x), and occurs over a longer time scale leading to a longer droplet lifetime than in subsonic flow. On the other hand, a subsonic incompressible freestream flow leads to vertically elongated droplets that are relatively thinner and disappear faster than in compressible flow.
6. Increasing the Weber number increases the rate of droplet deformation and reduces droplet lifetime in incompressible flow. The Weber number effect is stronger in incompressible compared to compressible flow

7. The viscous stress and pressure both appear to contribute to the droplet deformation in both supersonic and subsonic cases as indicated by the comparable magnitude of pressure gradient and divergence of viscous stress. In most cases the pressure appears to have the larger role in driving the deformation, especially with increasing time.
8. The combined effects of pressure distribution, shear stress, and gas recirculation in the leeward region of the droplet can be related to the observed droplet deformation and breakup. The resulting process combines all of these effects on droplet deformation.

Chapter 5 Recommended Future Work

Improved computing resources and computational time will be crucial factors in enabling future research on this complicated problem. A few recommendations that may be used as directions for future works or further research are listed below:

1) Sharper volume fraction treatment. This method is directly related to available computing power and time. Sharper volume fraction treatment will enable additional physics to be studied. This method will be done by employing a more advanced volume fraction discretization, such as the compressive discretization scheme. The Fluent guides state that this scheme is among the sharpest interface treatment in the Fluent's implicit scheme. The implicit scheme is preferable because it is much more stable in breakup compared to an explicit scheme. However, the method will need higher computing power to conduct in a reasonable time because the compressive scheme needs a lower time step to be stable, especially when droplet stripping begins. Test cases must be conducted to determine if this method is aligned with real life result. Additional physics that are possible to study with this improvement may include the formation of daughter droplets, instabilities at the droplet's windward surface, and droplet fragmentation, to mention a few.

2) Increasing the constant Reynolds number within the laminar regime. A different value of Reynolds number, still in laminar range, will enable studies of the effect of Reynolds and the effect of different types of laminar wake regions on the droplet deformation rate of supersonic and subsonic cases.

3) Conduct simulations using Fluent's large eddy simulation (LES) mode. By carefully building confidence in Fluent's LES mode through validation of well-known flows, the study for fixed Weber, Reynolds and Mach numbers can be extended to the turbulence regime, where the droplet wake region is characterized by a fully turbulent flow in a fashion more similar to existing experiments than this idealized computational case of laminar flow. This will shed light on the effect of compressibility on droplet breakup for higher Reynolds number, whether it will have the same effect as in this laminar study or not. Higher Reynolds

number brings the study closer to regimes where flow used in engineering more typically occur. However, this step is strongly dependent on available computing power, most likely to require advanced clustered hardware or extended period of time to resolve a case.

4. Simulation in with accelerating flow will bring condition closer to real life application in scramjets. As this type of study requires turbulence to be modeled correctly and calculation domain to be large, the computational cost will however be high.

Bibliography

[1] Y. Kim and J. Hermanson, "Breakup and Vaporization of Droplet Under Locally Supersonic Flow," *AIP Fluids,* 2012.

[2] O. G. Engel, "Fragmentation of Waterdrops in the Zone Behind an Air Shock," *Journal of Research of the Natioal Bereau of Standards,* 1958.

[3] A. R. Hanson, E. G. Domich and H. S. Adams, "Shock Tube Investigation of the Breakup of Drops by Air Blasts," *AIP Fluids,* 2010.

[4] D. D. Joseph, J. Belanger and G. S. Beavers, "Breakup of a liquid drop suddenly exposed to a high-speed airstream," *International Journal of Multiphase Flow 25,* pp. 1263-1303, 1999.

[5] T. G. Theofanous and G. J. Li, "On the physics of aerobreakup," *AIP Fluids,* 2008.

[6] T. G. Theofanous, G. J. Li, T. N. Dinh and C.-H. Chang, "Aerobreakup In Disturbed Subsonic and Supersonic Flow Fields," 2007.

[7] E. P. Lin and J. C. Hermanson, "Compression Wave Structure on Droplets under Supersonic Conditions," in *AAIA*, Denver, 2014.

[8] T. G. Theofanous, G. J. Li and T. N. Dinh, "Aerobreakup in Rarefied Supersonic Gas Flows," *ASME,* 2004.

[9] V. M. Boiko and S. V. Poplavski, "Experimental Study of Two Types of Stripping Breakup of the Drop in the Flow Behind the Shock Wave," *Combustion, Explosion, and Shock Wave,,* vol. 48, pp. 440-445, 2012.

[10] L. P. Hsiang and G. M. Faeth, "Near-Limit Deformation and Secondary Breakup," *International J. Multiphase Flow Volume 18,* pp. 635-652, 1992.

[11] M. Pilch and C. A. Erdman, "Use of Breakup Time Data and Velocity History Data to Predict The Maximum Size of Stable Fragments for Accelaration-Induced Breakup of a Liquid Drop," *Journal Multiphase Flow Volume 13,* pp. 741-757, 1987.

[12] I. M. Syahdan, A. Ferrante and J. C. Hermanson, "Dynamics and Deformation of Droplets Under Supersonic Conditions Poster," in *The Annual Poster Event of The William E. Boeing Department Of Aeronautics and Astronautics*, seattle, 2014.

[13] B. E. Gelfand, "Droplet Breakup Phenomena In Flows With Velocity Lag. Prog Energy Combustion Science," *Prog Energy Combustion Science Vol 22,* pp. 201-265, 1996.

[14] S. A. Krzeczkowski., "Measurement Of Liquid Droplet Disintegration Mechanism," *MInternational J. Multiphase Vol 6,* pp. 227-239, 1979.

[15] Z. Dai and G. M. Faeth, "Temporal Properties of Secondary Drop Breakup in the Multimode Breakup Regime," *International J. Multiphase Flow 27,* pp. 217-236, 2001.

[16] J. C. Meng and T. Colonius, "Numerical simulation of the early stages of high-speed droplet breakup," *Shock Waves,* pp. 399-414, 2015.

[17] H. Y. Li, Y. F. Yap, J. Lou and Z. Shang, "Numerical Modelling of Three-Fluid Flow using the Level-set Method," *Chemical Engineering Science,* pp. 224-236, 2015.

[18] C. W. Hirts and B. D. Nichols, "Volume of Fluid (VOF) Method for the Dynamics of Free Boundaries," *Journal of Computational Physics 39,* pp. 635-652, 1981.

[19] M. S. Dodd and A. Ferrante, "A Fast Pressure-Correction Method for Incompressible Two-Fluid Flows," *Journal of Computational Physics 273,* pp. 416-434, 2014.

[20] ANSYS.inc, ANSYS Fluent Theory Guide.

[21] H. W. Liepmann and A. Roshko, Elements of Gasdynamic, New York: Wiley, 1957.

[22] M. Boger, F. Jaegle, B. Weigand and C.-D. Munz, "A pressure-based treatment for the direct numerical simulation," *Computer and Fluids,* pp. 338-349, 2014.

[23] Y. Rimon and S. I. Cheng, "Numerical Solution of A Uniform Flow over a Sphere at Intermediate Reynolds Number," *The Physics Of Fluids,* vol. 12, 1969.

[24] G. Constantinescu and K. Squires, "Numerical Investigations of Flow over Sphere in the Subcritical and Supercritical Regimes," *Physics of Fluids,* vol. 16, 2004.

[25] S. S. W. Lam and N. Pollock, "An Experimental Study of Transonic Flow Past a Sphere," in *Tenth Australian Fluid Mechanics Conference*, Melbourne, 1989.

[26] P. Simpkins and E. Bales, "Water-drop Response to Sudden Accelerations," *J. Fluid Mech Volume 55,* pp. 629-639, 1972.

Appendix

Appendix A: Fluent Setup settings

This appendix lists setup changes from fluent default values.

Table 4. Fluent Detailed Setup

Main Tab	Sub Tabs
Setup > General	Solver > Type > Pressure Based
	Solver > Time > Transient
	Solver > 2D Space > Axisymmetric
Setup > Models	Multiphase> Model>Volume of Fluid
	Multiphase> Volume Fraction Parameters> Implicit
	Multiphase> Body Force Formulation> Implicit Body Force Checked
	Phase> Primary Phase> Phase Material> air (modified dynamic viscosity)
	Phase> Secondary Phase> Phase Material> isopropanol (modified)
	Phase> Phase interaction> Surface tension> Surface Tension Force Modelling On
	Phase> Phase interaction> Surface tension> Model> Continuum Surface Stress
	Phase> Phase interaction> Surface tension coefficients (N/M)> isopropanol-air> constant>0.0213
	Viscous> Model> Laminar
	Energy> On
Setup > Materials	Fluid> isopropanol> User defined database> Location of isopropanol.scm> ok
	Fluid> isopropanol> Change/Create
	Fluid> air> Density (kg/m3)> Ideal gas (supersonic cases), Incompressible ideal gas (subsonic cases)
	Fluid> air> Viscosity (kg/(m-s))> power law> Reference vicosity (kg/m3)> See input table
Setup > Boundary Condition	Fluid> air> Viscosity (kg/(m-s))> power law> Reference temperature (k)> 275.15
	Fluid> air> Viscosity (kg/(m-s))> power law> Temperature Exponent> 0.7
	inlet boundary name > velocity inlet> Momentum> Velocity Magnitude> See input table
	inlet boundary name > velocity inlet> Thermal> Temperature (k)> see input table
	outlet boundary name > pressure outlet
	axisymmetric axis name > axis
	top symmetry name > symmetry
	Operating Pressure> See input table
Setup > Mesh Interface	Mesh name> define interface name
	Connect all subdomain one-by-one interface through interface Zone 1 and Interface Zone 2 > Create
Setup> Reference Value	Reference value > Compute From> inlet boundary name

Setup> Solution Methods	Pressure-Velocity Coupling > Scheme> PISO
	Spatial Discretization > Pressure> Body force weighted
	Volume fraction> First order upwind
	Under-relaxation Factors> Pressure> 0.9
	Under-relaxation Factors> Density> 1
	Under-relaxation Factors> Body force> 1
	Under-relaxation Factors> Momentum > 0.9
	Under-relaxation Factors> Volume fraction > 0.9
	Under-relaxation Factors> Energy > 1
	Advanced> BCGSTAB
Setup> Calculation activities	Autosave Every (time step)> 50
	Autosave Every (time step)> edit> select all variables wanted to use in CFD-post
Setup> Run Calculation	Time stepping method> Fixed
	Time Step Size (s)> 1e-08 (initial steup, adjust as needed)

Appendix B. Divergence of Viscous Stress Equation

Divergence informs the flux on a variable of point, which can act as a source of a sink. The divergence can be interpreted as how strong a variable works on a place and it direction. So it can be used an indicator of what physic is working on a phenomenon.

The divergence of viscous stress tensor is presented by matrix equation (8)

$$\nabla.\tau = \begin{matrix} \frac{d\tau_{xx}}{dx} & \frac{d\tau_{xy}}{dy} & \frac{d\tau_{xz}}{dz} \\ \frac{d\tau_{yx}}{dx} & \frac{d\tau_{yy}}{dy} & \frac{d\tau_{yz}}{dz} \\ \frac{d\tau_{zx}}{dx} & \frac{d\tau_{yz}}{dy} & \frac{d\tau_{zz}}{dz} \end{matrix} \tag{8}$$

The components can be built using equation (9):

$$\tau_{ij} = \left(-\left(\frac{2}{3}\right)\mu\,\nabla.v\right)\delta_{ij} + \mu\left(\frac{\partial v_i}{\partial x_j} + \frac{\partial v_j}{\partial x_i}\right) \quad , \tag{9}$$

where μ is the dynamic viscosity and v is the velocity. If $i = j$, then $\delta_{ij} = 1$, other else $\delta_{ij} = 0$.

In the case of incompressible flow, $\nabla.v = 0$

The total effect of the stresses ($\nabla.\sigma$) which include the pressure term has a matrix similar to equation (9), but its components are built by equation (10)

$$\sigma_{ij} = -\left(P + \left(\frac{2}{3}\right)\mu\,\nabla.v\right)\delta_{ij} + \mu\left(\frac{\partial v_i}{\partial x_j} + \frac{\partial v_j}{\partial x_i}\right) \quad , \tag{10}$$

where p is absolute pressure.

Because $\nabla.\sigma$ has the component of pressure and viscous stress, the gradient of pressure and the divergence of viscous stress should have resultant that is equal to $\nabla \cdot \sigma$. This can be used as a check to ensure the build of divergence of viscous stress in the post-processor software is correct.

Appendix C. Pressure Distribution

List of pressure distribution, Offset time form top: 1 μs, 3 μs, 7 μs, 11 μs, and 15 μs of We = 200 and 50

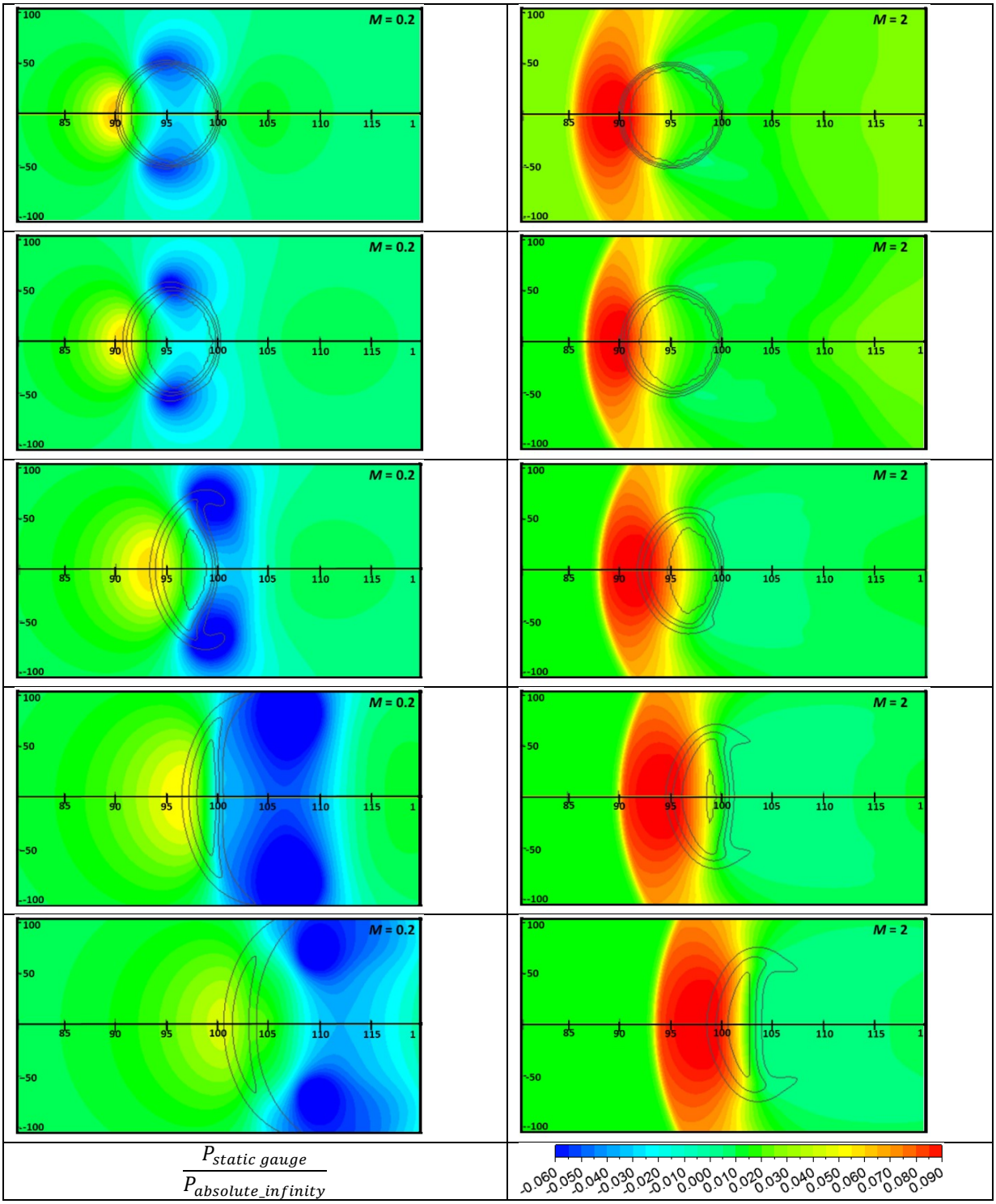

Figure 43. Normalized pressure comparison: Subsonic (left) flow and Supersonic (right) flow, displayed in the same color code. *Re* = 100, *We* = 200. Offset time form top: 1 µs, 3 µs, 7 µs, 11 µs, and 15 µs. Offset time form top: 1 µs, 3 µs, 7 µs, 11 µs, and 15 µs. The droplets are represented by black iso- lines of volume fraction values: 0.98 (innermost), 0.9, 0.5, and 0.1 (outermost).

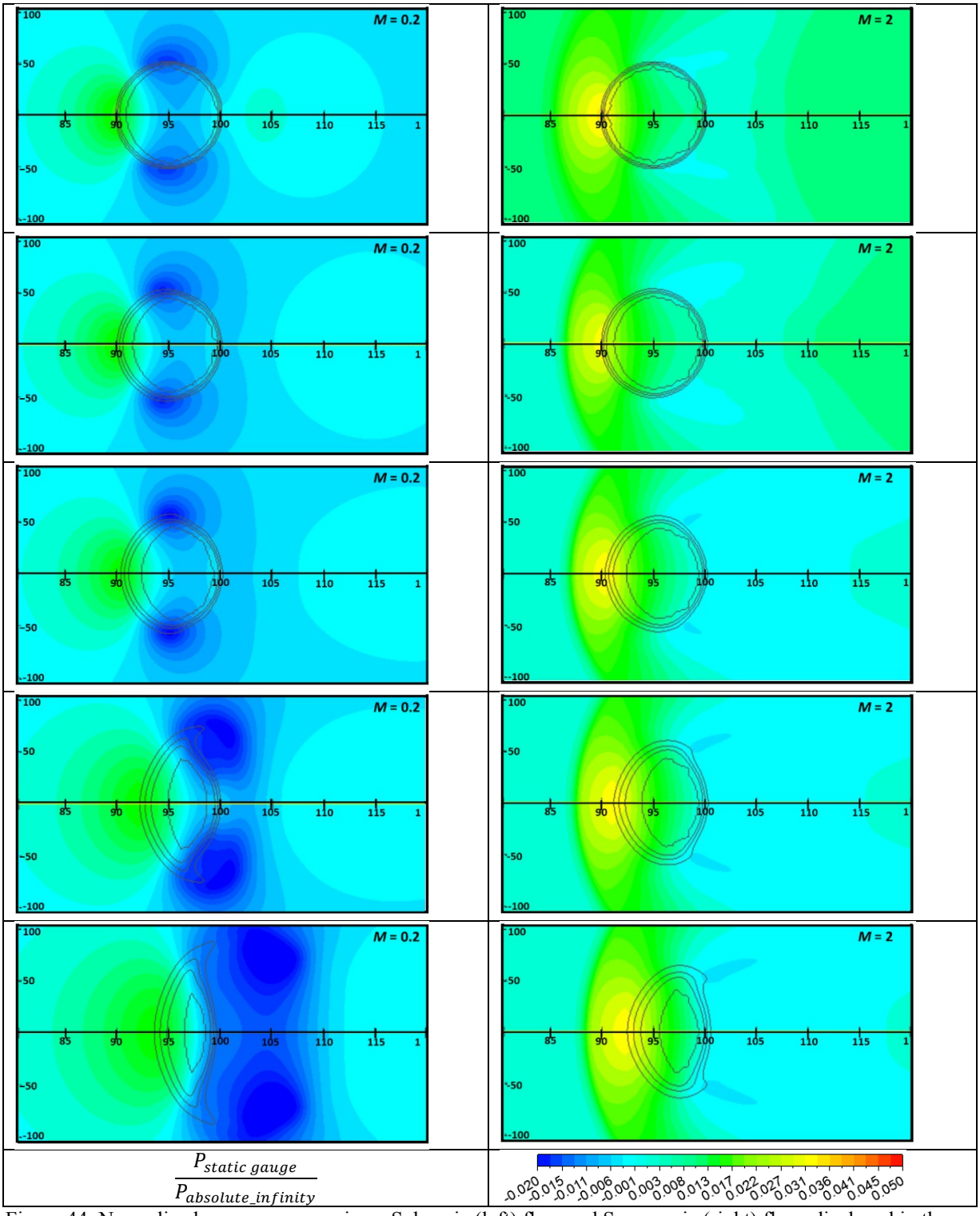

Figure 44. Normalized pressure comparison: Subsonic (left) flow and Supersonic (right) flow, displayed in the same color code. *Re* = 100, *We* = 50. Offset time form top: 1 μs, 3 μs, 7 μs, 11 μs. Offset time form top: 1 μs, 3 μs, 7 μs, 11 μs, and 15 μs. The droplets are represented by black iso- lines of volume fraction values: 0.98 (innermost), 0.9, 0.5, and 0.1 (outermost).

Appendix D: Recirculation

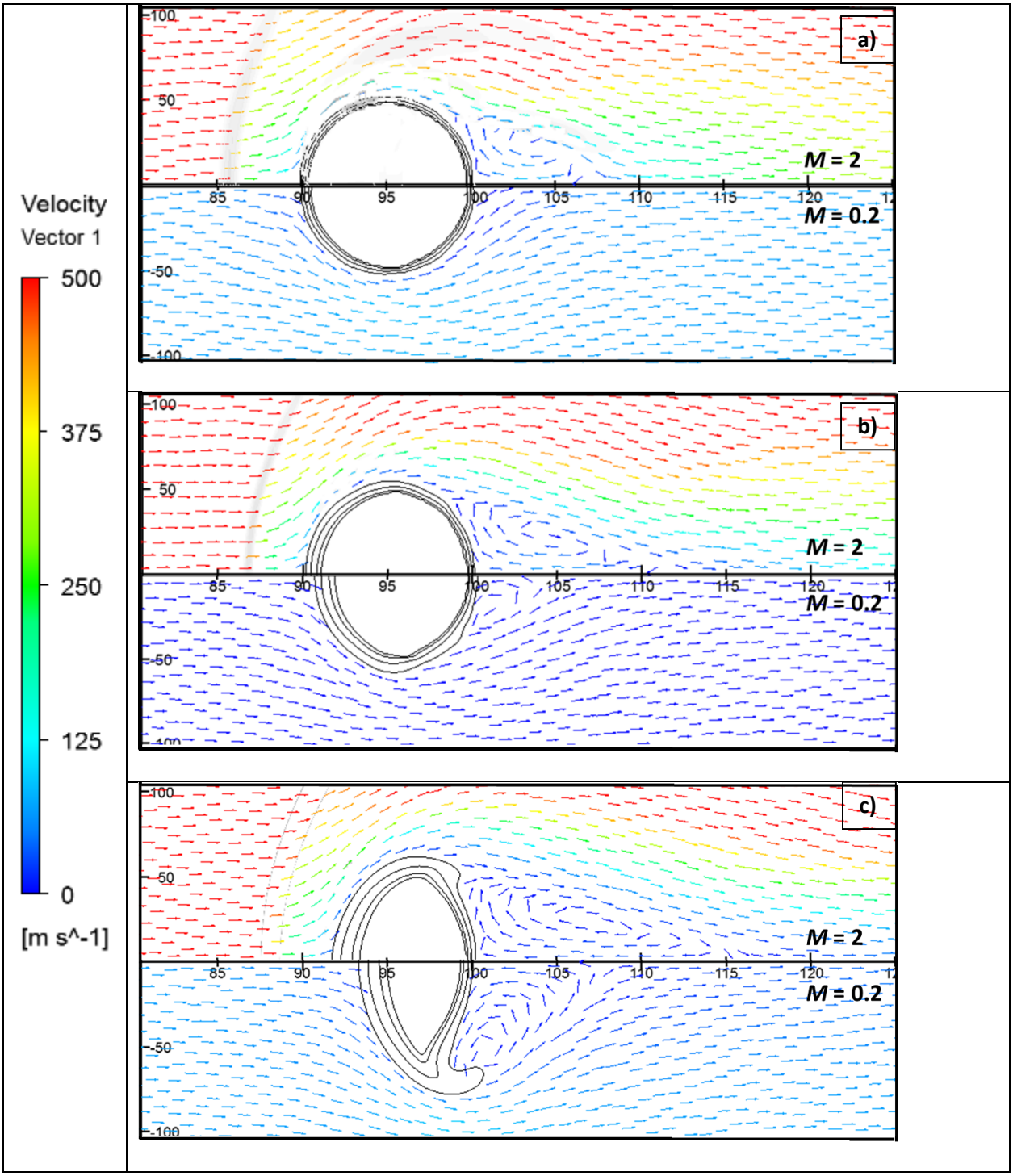

Figure 45. Supersonic (upper) case and Subsonic (lower) case velocity vectors evolution. *Re* = 100, *We* = 200. Offset time: a) 1 µs, b) 3 µs, c) 7 µs. The droplets are represented by black iso-lines of volume fraction values: 0.98 (innermost), 0.9, 0.5, and 0.1 (outermost)

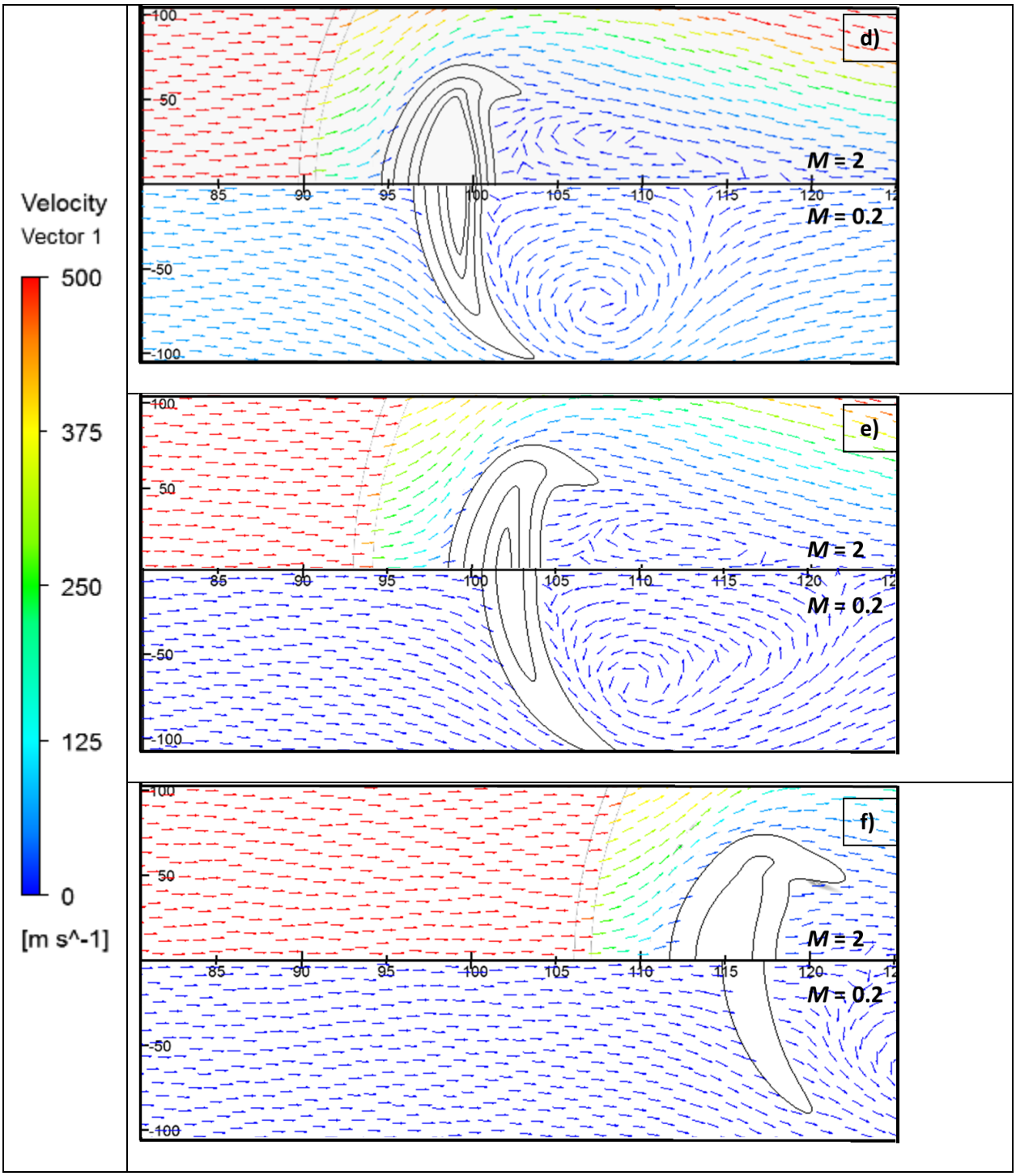

Figure 46.Supersonic (upper) flow and Subsonic (lower) flow velocity vectors evolution (continued). *Re* = 100, *We* = 200. Offset time: d) 11 µs, e) 15 µs, f) 23 µs. The droplets are represented by black iso-lines of volume fraction values: 0.98 (innermost), 0.9, 0.5, and 0.1 (outermost)

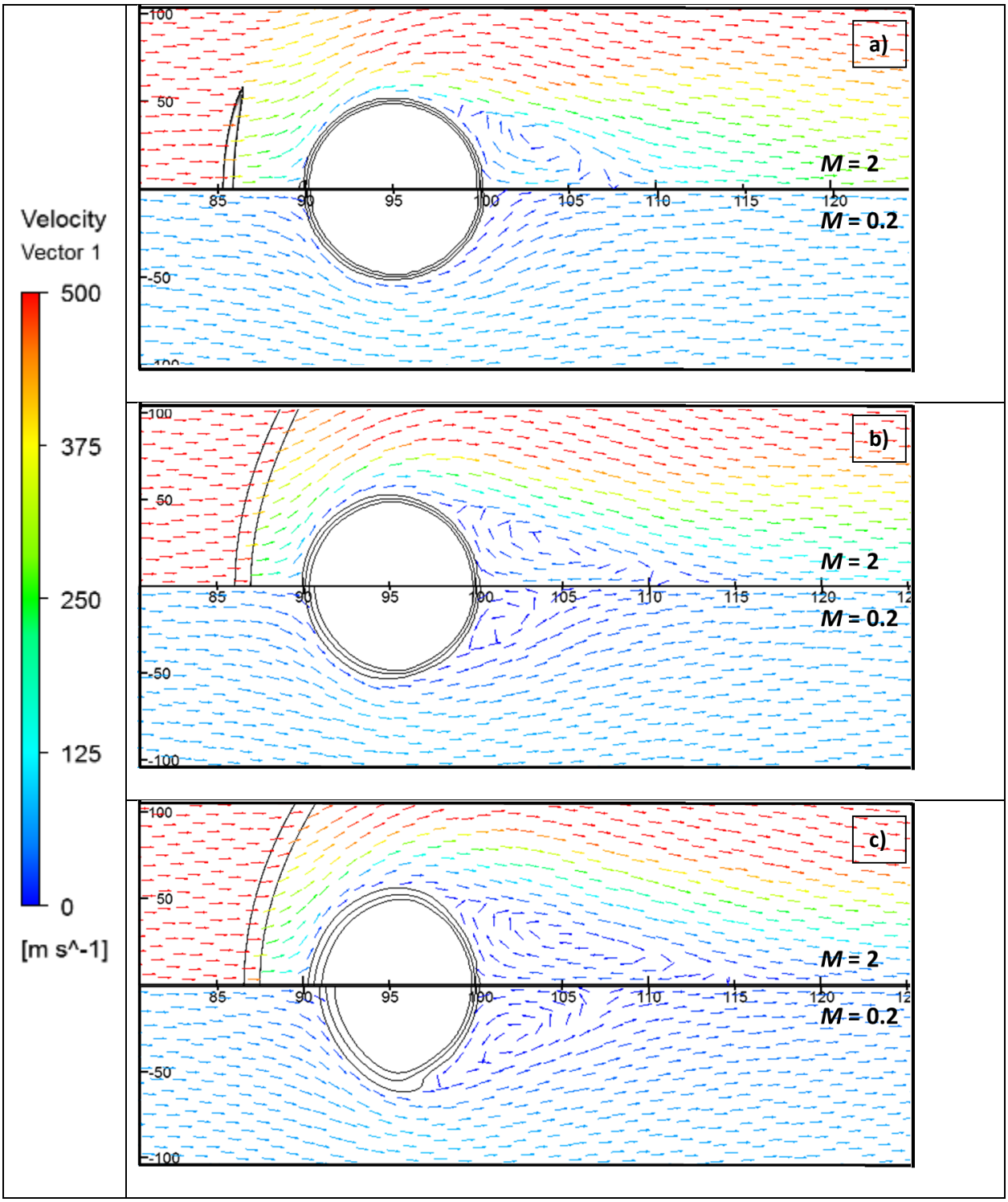

Figure 47. Supersonic (upper) flow and Subsonic (lower) flow velocity vectors evolution. *Re* = 100, *We* = 50. Offset time: a) 1 µs, b) 3 µs, c) 7 µs. The droplets are represented by black iso-lines of volume fraction values: 0.98 (innermost), 0.9, 0.5, and 0.1 (outermost)

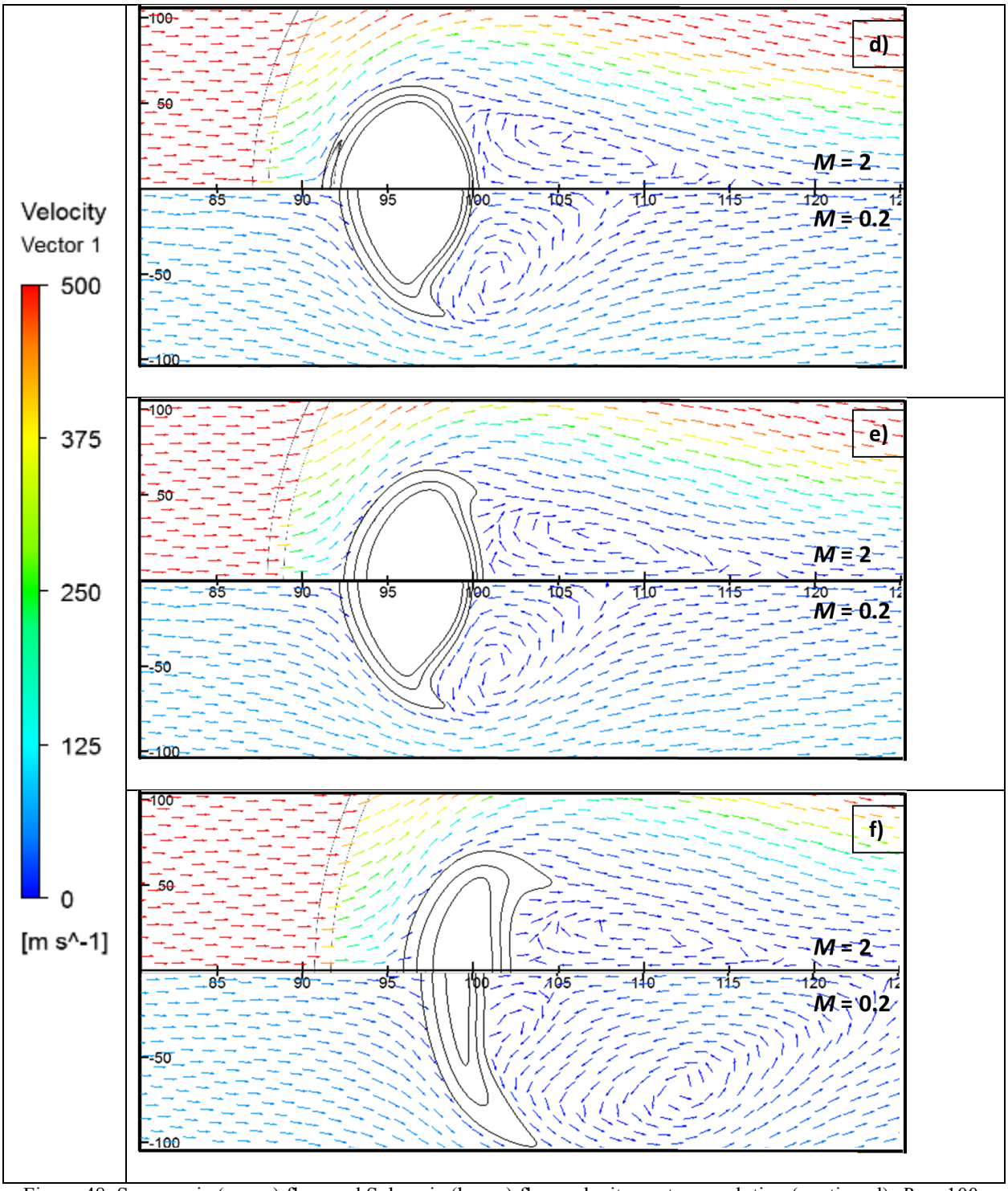

Figure 48. Supersonic (upper) flow and Subsonic (lower) flow velocity vectors evolution (continued). *Re* = 100, *We* = 50. Offset time: d) 11 µs, e) 15 µs, f) 23 µs. The droplets are represented by black iso-lines of volume fraction values: 0.98 (innermost), 0.9, 0.5, and 0.1 (outermost)

Appendix E: Recirculation (Normalized)

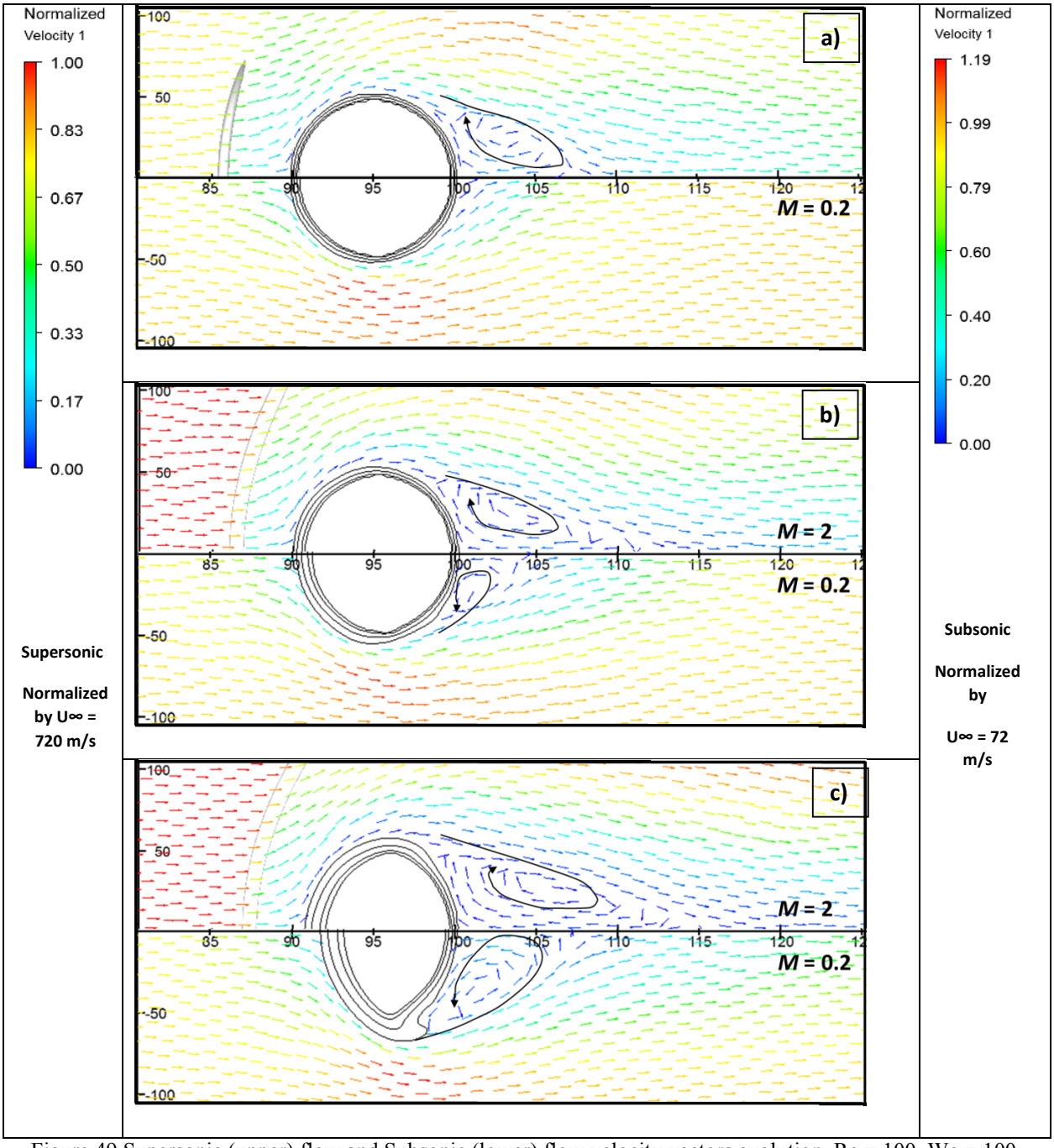

Figure 49.Supersonic (upper) flow and Subsonic (lower) flow velocity vectors evolution. Re = 100, We = 100. Offset time: a) 1 µs, b) 3 µs, c) 7 µs. The droplets are represented by black iso-lines of volume fraction values: 0.98 (inner most), 0.9, 0.5, and 0.1 (outer most). The general movement of swirl region shown to aid recirculation center visualization.

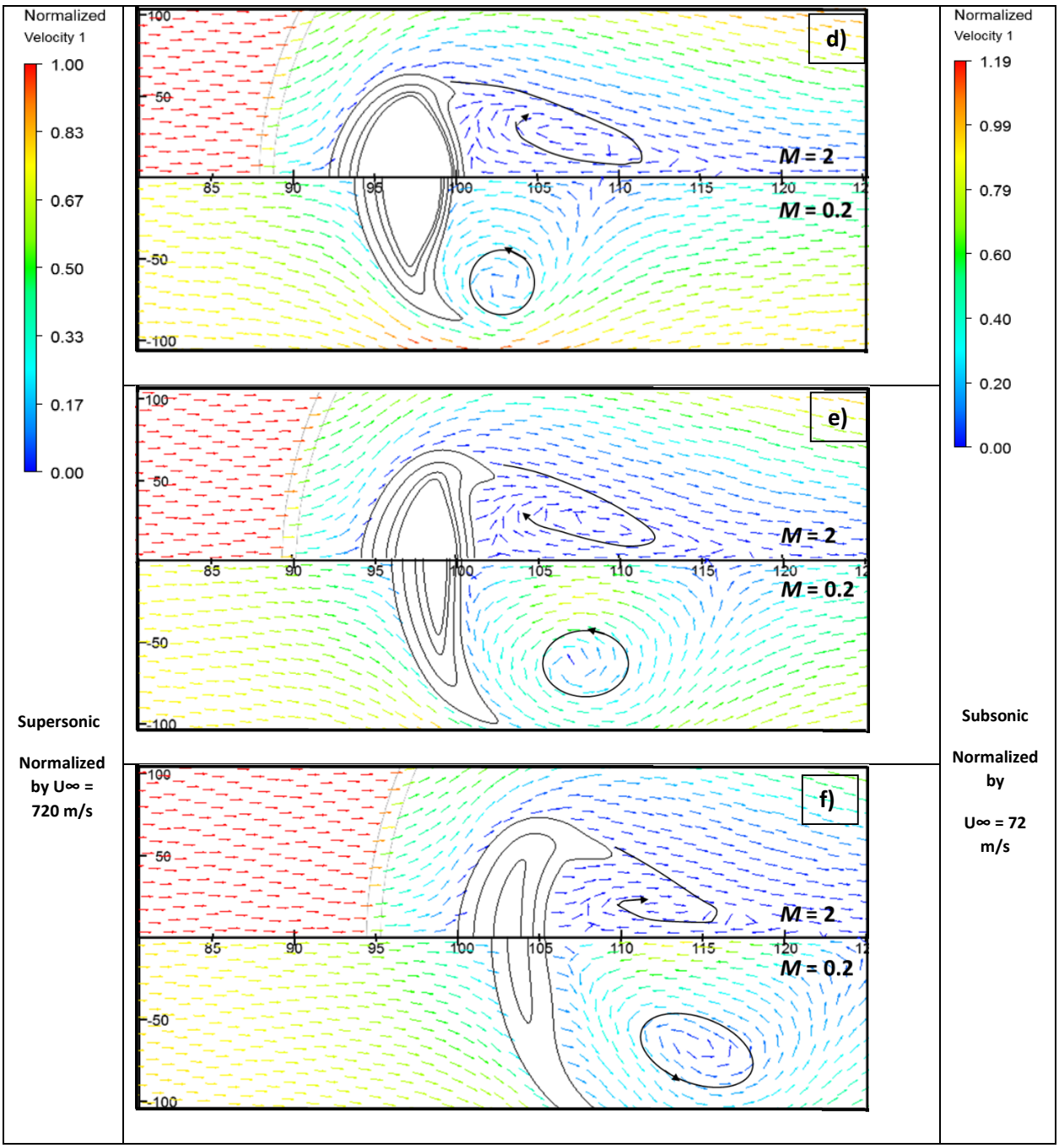

Figure 50. Normalized Supersonic (upper) flow and Subsonic (lower) flow case velocity vectors evolution. *Re* = 100, *We* =100. Offset time: d) 11 µs, e) 15 µs, f) 23 µs. The droplets are represented by black iso-lines of volume fraction values: 0.98 (innermost), 0.9, 0.5, and 0.1 (outermost). The general movement of recirculation region shown to aid recirculation center visualization.

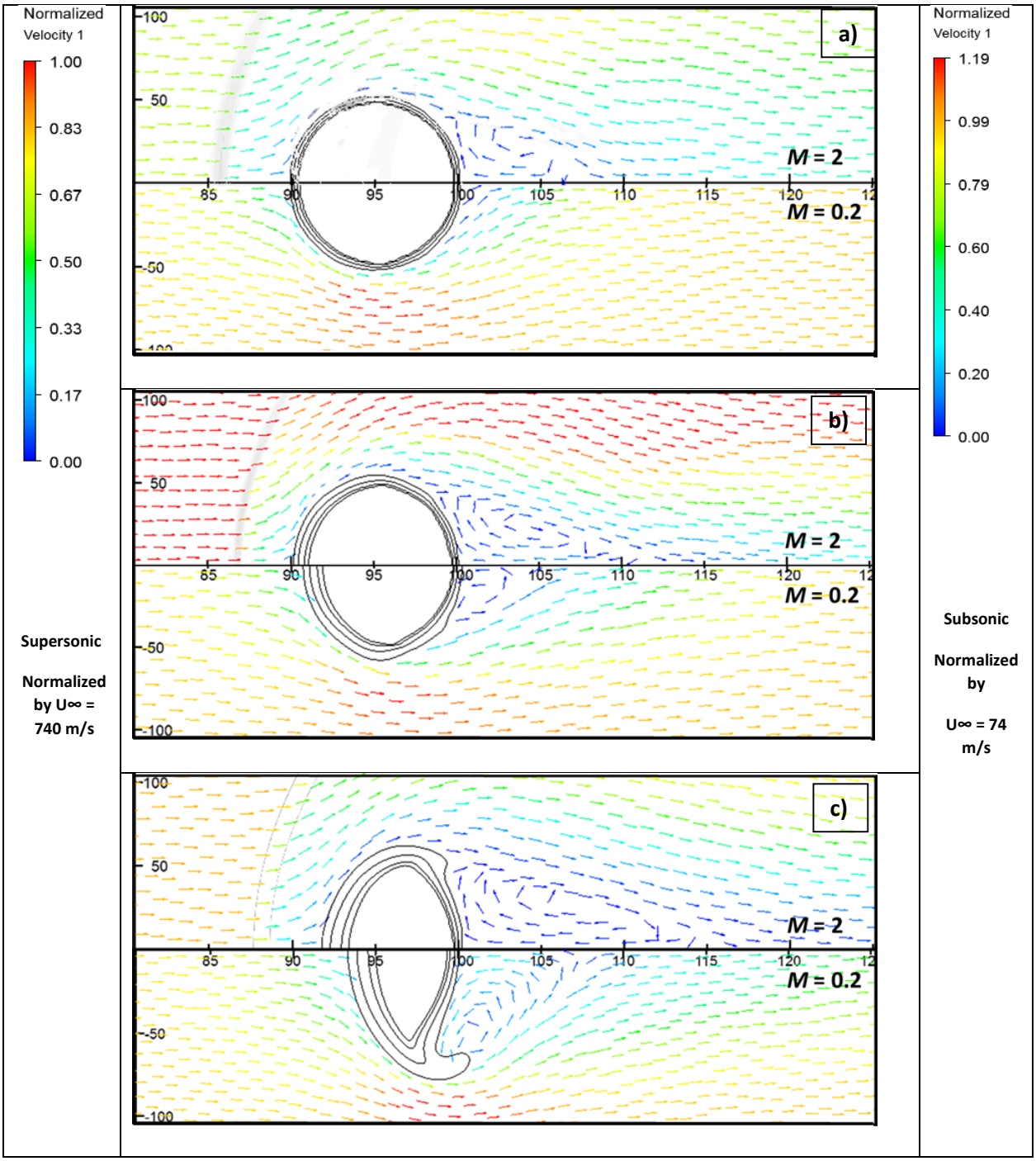

Figure 51. Normalized Supersonic (upper) flow and Subsonic (lower) flow velocity vectors evolution. *Re* = 100, *We* = 200. Offset time: a) 1 µs, b) 3 µs, c) 7 µs. The droplets are represented by black iso-lines of volume fraction values: 0.98 (innermost), 0.9, 0.5, and 0. 1 (outermost). The general movement of the swirl region shown to aid recirculation center visualization.

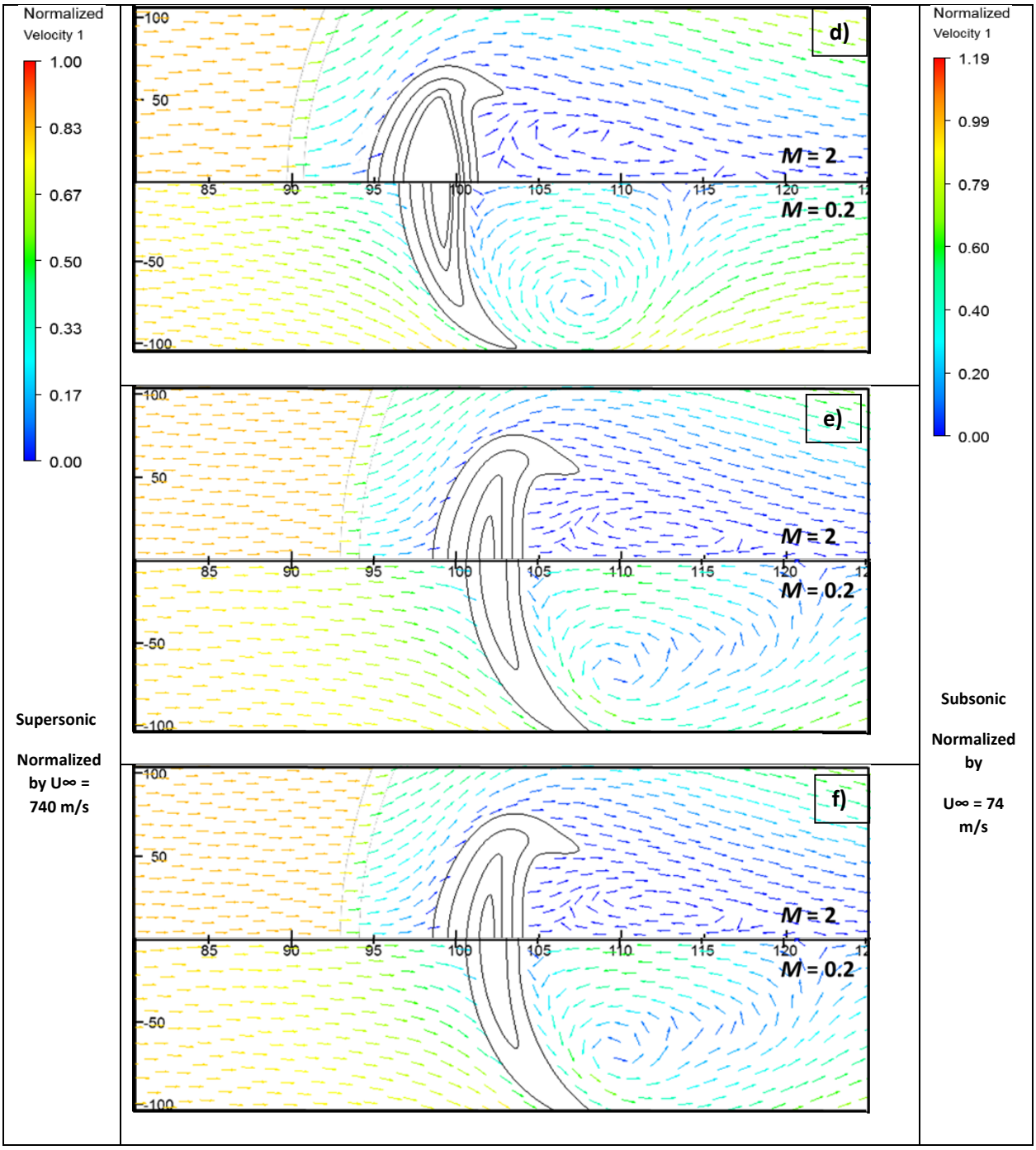

Figure 52. Normalized Supersonic (upper) flow and Subsonic (lower) flow velocity vectors evolution (continued). *Re* = 100, *We* = 200. Offset time: d) 11 µs, e) 15 µs, f) 23 µs. The droplets are represented by black iso-lines of volume fraction values: 0.98 (innermost), 0.9, 0.5, and 0.1 (outermost). The general movement of recirculation region shown to aid swirl center visualization.

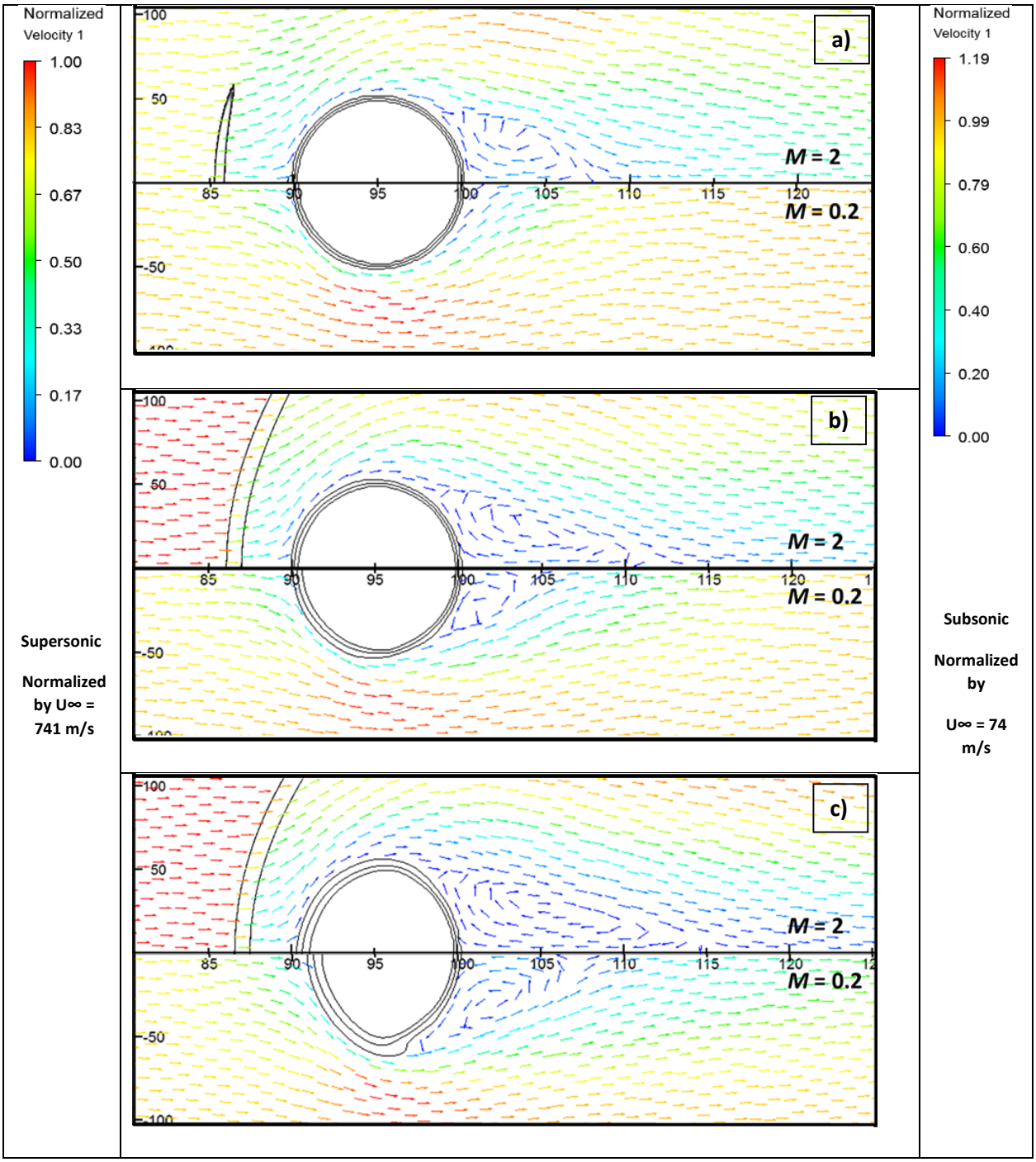

Figure 53. Normalized Supersonic (upper) flow and Subsonic (lower) flow velocity vectors evolution. *Re* = 100, *We* = 50. Offset time: a) 1 µs, b) 3 µs, c) 7 µs. The droplets are represented by black iso-lines of volume fraction values: 0.98 (inner most), 0.9, 0.5, and 0.1 (outer m most). The general movement of recirculation region shown to recirculation swirl center visualization.

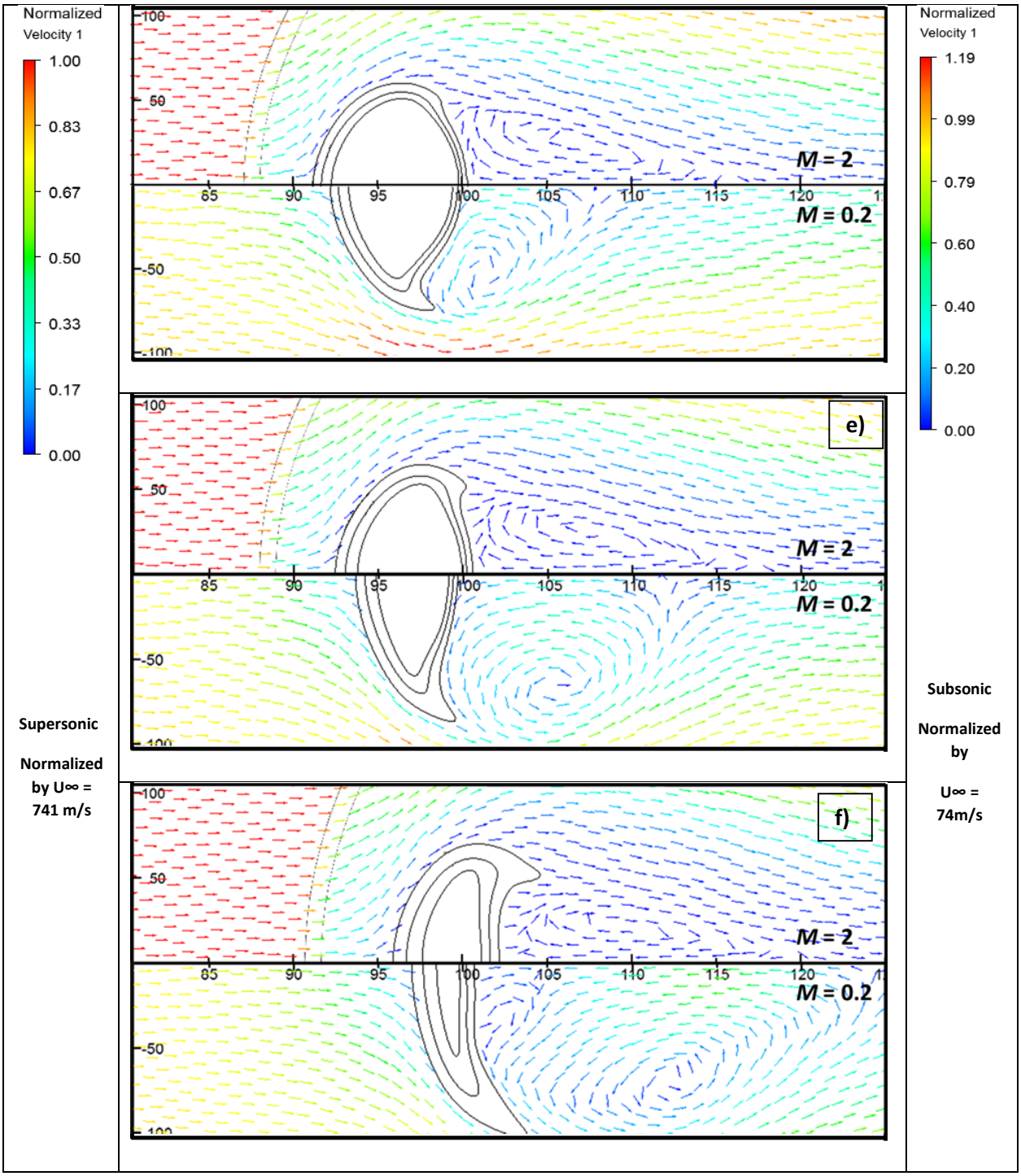

Figure 54. Normalized Supersonic (upper) flow and Subsonic (lower) flow velocity vectors evolution (continued). *Re* = 100, *We* = 50. Offset time: d) 11 µs, e) 15 µs, f) 23 µs. The droplets are represented by black iso-lines of volume fraction values: 0.98 (innermost), 0.9, 0.5, and 0.1 (outermost). The general movement of recirculation region shown to aid swirl center visualization.